

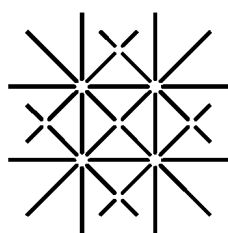
**Novel Principle for
2D Molecular Self-Assembly:
Self-Intermixed Monolayer Phases of
Sub-Phthalocyanine and C₆₀ on Ag(111)**

INAUGURALDISSERTATION

zur
Erlangung der Würde eines Doktors der Philosophie
vorgelegt der
Philosophisch-Naturwissenschaftlichen Fakultät
der Universität Basel
von

Michael de Wild
aus Basel (BS)

Basel, 2002



UNI
BASEL

Genehmigt von der Philosophisch-Naturwissenschaftlichen Fakultät auf Antrag von

Prof. Dr. H.-J.Güntherodt
Prof. Dr. E. Meyer
Dr. T.A. Jung

Basel, den 22. Oktober 2002

Prof. Dr. Marcel Tanner, Dekan

Abstract

In this thesis, a novel route to highly perfect bi-molecular self-assembly on a metallic surface is presented. Two kinds of organic molecules, the polar Chloro-[subphthalocyaninato]-boron(III) (SubPc) and the polarizable C₆₀-Buckminster fullerene, were co-deposited onto atomically clean Ag(111) under UHV conditions. Depending on the relative surface coverage of the two species, different well-ordered intermixed monolayers are formed: At a mixing ratio SubPc/C₆₀ = 2:3, an anisotropic *stripe* structure consisting of C₆₀-chains with an inter-chain periodicity of 3.3 nm is found. A mixing ratio SubPc/C₆₀ = 1:1 leads to a 2D hexagonal pattern with periodic vacancies. At room-temperature, the structures spontaneously emerge by self-organization and are stable at the same. The mixed structures show interesting and unusual features. One of the ordered bi-molecular overlayer, the 3:2-*stripe*-phase, exists in two chiral forms, although the individual molecules themselves are achiral. Different phases can co-exist simultaneously, and also a 2D molecular gas phase can be observed. The appearance of the molecular *stripe* domains in STM measurements strongly depends on the applied bias-voltage. The structural parameters and the schematic binary “phase-diagram” of this system are deduced from detailed room-temperature Scanning Tunneling Microscopy (STM) studies. The underlying interactions and the relevant properties of the molecules are discussed, based on STM, XPS and UPS measurements and on numerical simulations. The pattern formation is further treated under thermodynamic aspects of a two-component mixture. A counter-example to the intermixed system is further presented: silylated Perylen and C₆₀ molecules, co-adsorbed on clean Ag(100), do not intermix but lead to a 2D segregation.

These novel *Self-Intermixed Monolayer Phases* (SIMP) are different from previously known self-assembled molecular monolayers in that they form intermixed patterns at room temperature on uniform, unreconstructed atomically clean terraces. These self-organized patterns, as well as the additionally shown conformational changes of Porphyrin molecules, inspire to be incorporated in building blocks of possible molecular electronic devices.

Contents

Abbreviations	iv
1. Introduction: Motivation and Outline	1
2. Instrumental Methods and Set-up	4
2.1. UHV System	4
2.2. Substrates	4
2.3. Organic Molecular Beam Epitaxy (OMBE)	6
2.4. Scanning Tunneling Microscopy (STM)	7
2.5. Photoelectron Spectroscopy (PES)	9
2.6. Introduction to Molecular Modeling	12
3. Self-Assembly of Phthalocyanines and C₆₀ on Ag(111)	14
3.1. Molecular Self-Assembly and 2D Layering	14
3.2. Single Component Phases: Phthalocyanines and C ₆₀ on Ag(111)	16
3.3. Mixture of C ₆₀ and SubPc: 3:2- <i>Stripe</i> Phase	18
3.3.1. Adsorption Geometry of the <i>Stripe</i> Pattern	20
3.3.2. Chiral Supra-Molecular Structures of Achiral Molecules	23
3.4. Mixture of C ₆₀ and SubPc: Binary 1:1- <i>Star</i> Phase	23
3.4.1. Adsorption Geometry of the <i>Star</i> Pattern	26
3.4.2. 2D Molecular Gas-Phase	26
3.5. Schematic Room-Temperature Binary Phase Diagram	28
4. Intermixing Mechanism	31
4.1. A Delicate Balance of Electrostatic and Van der Waals Interactions	31
4.2. Discussion of Other Intermixing Models	34
4.2.1. Long-Range Interactions Mediated by Substrate Surface States	35
4.2.2. Intrinsic Dipole-Dipole Interaction	36
4.2.3. Intermolecular Charge Transfer: Apparent Height Analysis	36
4.2.4. Formation of a New Chemical Complex	38
4.3. Thermodynamics of Mixtures	46
4.4. Typically Segregating System: Perylen – C ₆₀ Codeposited on Ag(100)	53
4.4.1. C ₆₀ on Ag(100)	53
4.4.2. Siliated Perylenes on Ag(100)	56
4.4.3. Mixture C ₆₀ – Perylen	58
5. Conclusion and Outlook	60

A. Porphyrins: A Model Molecule to Study Conformational Flexure and Switching	65
A.1. Structure of a Free Cu-TBPP Molecule	65
A.2. Molecular Conformation	66
A.3. Cu-TBPP on Ag(100)	68
A.4. Conclusion	73
Bibliography	76
Acknowledgements	95
Conferences and Publications	96
Curriculum Vitae	98

Abbreviations

1D, 2D, 3D	One-, two, three-dimensional
AFM	Atomic force microscope
BE	Binding energy
C ₆₀	C ₆₀ Buckminster fullerene
Cu-TBPP	Cu-tetra-[3,5 <i>di-ter-butyl-phenyl</i>] porphyrin
DOS	Density of states
E_F	Fermi-energy
ESCA	Electron spectroscopy for chemical analysis
hcp	Hexagonal close-packed
HOMO	Highest occupied molecular orbital
KE	Kinetic energy
LB	Langmuir-Blodgett
LUMO	Lowest unoccupied molecular orbital
LEED	Low-energy electron diffraction
MBE	Molecular beam epitaxy
ML	Monolayer
OMBE	Organic molecular beam epitaxy
Perylen	<i>N, N', N'', N'''</i> -Tetra(trimethylsilyl)-4,9-diamino-perylenchinon-3,10-diimin
PES	Photoelectron spectroscopy
Pc	Phthalocyanine
SAM	Self-assembled monolayers
STM	Scanning tunneling microscope
STS	Scanning tunneling spectroscopy
RT	Room-temperature
SIMP	Self-intermixed monolayer phase
SubPc	Chloro[subphthalocyaninato]boron(III)
UHV	Ultra-high vacuum
UPS	Ultraviolet photoelectron spectroscopy
XPS	X-Ray photoelectron spectroscopy

1. Introduction: Motivation and Outline

In the natural world, molecules are used for many purposes. Using molecule-based materials for electronics, sensing, and optoelectronics is a new endeavor, called *molecular electronics*, and the subject of riveting new research [1–4] and substantial popular press interest. A convenient definition of molecular electronics by M.A. Ratner [5] is *the set of electronic behaviors in molecule-containing structures that are dependent upon the characteristic molecular organization of space*. Early work focused on some visionary [6] or speculative [7] ideas and mechanistic suggestions, showing in the early 70ies that it is theoretically possible to use a single molecule as a rectifier. Some truly pioneering measurements of charge transfer across molecular adlayers [8] were done in 1971 and S. Roth [9] demonstrated an experiment in 1995 with an donator-acceptor molecule within a Langmuir-Blodgett film that behaved like a diode.

There is currently great interest in the adsorption of large organic molecules on inorganic surfaces. Partly, this activity is due to the increasing use of organic semiconductors for technological purposes. Organic light emitting diodes [10–12] and thin films transistors [13, 14] may serve as examples in this context. A recent break-through was achieved by designing logic circuits with field-effect transistors on the basis of single carbon nanotubes [15]. At the same time, a fundamental interest arises to extend the notions formed by myriad investigations of small molecule adsorption to the physisorption of larger adsorbates, which involve a higher degree of functionalization and can be designed by concepts of Supramolecular Chemistry [16–18]. An important class of molecular device functionality is based upon reversible changes of molecular conformation. One can argue that conformational changes in molecules represent the ultimate limit of nanomechanics.

The advent of self-assembly methodologies [19, 20] for efficient arrangement of a large number of molecules and the development of scanning probe techniques [21–24], both to prepare molecular nanostructures and to characterize their physical and electrical properties, made prototype molecular electronic devices into a reality.

The field of molecular electronics seeks to use individual molecules to perform functions in electronic circuitry now performed by semiconductor devices [25]. Individual molecules are hundreds of times smaller than the smallest planar features conceivably attainable by semiconductor technology. Because it is the area taken up by each electronic element that matters, electronic devices constructed from molecules will be hundreds of times smaller than their semiconductor-based counterparts. Moreover, individual molecules are easily made exactly the same by the billions and trillions. The dramatic reduction in size, and the sheer enormity of numbers in manufacture are the principle benefits offered by the field of molecular electronics.

In order to produce ultra-small structures which provide some functionality to our decimeter world, two key problems need to be addressed: First these devices need to be manufac-

1. Introduction: Motivation and Outline

tured by efficient (parallel or self-assembled) techniques, and second, they need to be interconnected and “wired” at least to the micrometer level which is accessible by state-of-the-art technology.

The long-term goal is to provide moderate computational power and high-density memory in an extreme small, low-power format, which will not require multibillion-Euro fabrication facilities. The conventional CMOS technique may stall at 10 nm, depending on the fabrication economy, because the production has to be extremely accurate. This is meant by the often quoted “breakdown of Moore’s law”. In the mid 1960s, Gordon Moore, then working as a Director of R+D for Fairchild Semiconductor, came out with his famous quote to the press. He stated that he expected transistor density per Integrated Circuit to double every 18 - 24 months (“Moore’s Law”, see figure 1.1). It seems as if Gordon Moore’s vision, as the co-founder of Intel Corporation in 1968, was right up to now: The new Northwood core Pentium 4 processors have more than 55 million transistors. But not only the afore mentioned economic reasons, but also fundamental physical principles like leaking tunneling currents between two narrow structures could lead to a conversion of the production methods towards molecular electronics.

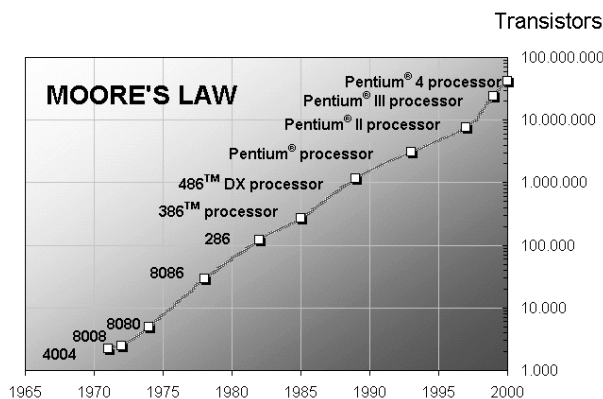


Figure 1.1.: The number of transistors integrated into Integrated Circuits is growing exponentially since the seventies following the prediction of Gordon Moore in 1968. For its continuity, however, new technologies might be needed. Data from [26].

As a highly interdisciplinary field, progress depends on successful interactions across the boundaries of traditional subject areas. Molecular electronics encompasses biology, chemistry, computing, electronics and physics, each subject with its own methodology and jargon. Most importantly, there is a huge potential for research and discovery, which has motivated National and International Research Programs to collaborate with Multi-National Corporations in one or the other field. The close collaboration of scientists and technologists from many different fields propels nanoscience and nanotechnology.

During this PhD thesis, a novel principle of self-assembly was investigated which leads to nanostructures that have the potential to serve as building blocks for molecular electronic devices. The bi-molecular system Subphthalocyanine (SubPc) and C_{60} , co-deposited

on the clean Ag(111) surface, self-organizes into specific nanometer-size structures. The relative surface coverage of the two species determines the geometry of the observed patterns, which could in principle serve as the basis for storage devices at room-temperature. The conformational switching of single Porphyrin molecules gives similar ideas towards storage applications.

The outline of this thesis is as follows: Chapter 2 describes the ultra-high vacuum system which has been used to investigate single molecules at atomically clean surfaces. The preparation of the samples is described, including the substrate fabrication and the molecular deposition. The main analyzing tools, the Scanning Tunneling Microscope (STM) and the Electron Spectroscopy for Chemical Analysis (ESCA), are briefly explained. A short overview over the computational methods closes this chapter. In Chapter 3, the binary Self-Intermixed Monolayer Phases (SIMP) are discussed. It starts with the description of both individual components, SubPc and C₆₀, and then shows the various phases with their specific compositions. The adsorption geometry of all phases with their properties like induced chirality are further discussed. The chapter ends with the schematic room-temperature “phase diagram”. A detailed discussion of the underlying intermixing mechanism is given in Chapter 4, followed by a general consideration of thermodynamics of mixtures. It is not clear a priori whether two components mix or segregate. The phase behavior here is studied under thermodynamic aspects. Also given is a counter-example by a segregating binary system which does not lead to exciting intermixed structures. Chapter 5 gives a few examples of potential applications of the created patterns, including ideas for a continuation of this work. Appendix A presents an example of the attractive field of molecular conformation and its relevance in a larger context.

2. Instrumental Methods and Set-up

In this chapter, the experimental methods and the *Nanolab* at the University of Basel are described. In section 2.1, the UHV system is presented. In section 2.2, details on the Ag(111) and Ag(100) substrate preparation are given. Section 2.3 describes the molecular deposition system. The main tool used during this thesis is the scanning tunneling microscope (STM), described in section 2.4. Chemical analysis of the sample surface and measurements of the valence band were done by photoelectron spectroscopy, discussed briefly in section 2.5. Finally, an introduction to computational methods to investigate quantum molecular problems is given in section 2.6.

2.1. UHV System

Ultra high vacuum (UHV) is indispensable to study atomic processes at surfaces because it extremely reduces the density of contaminants. Under UHV condition with 10^{-11} mbar pressure, the number of molecules in the vacuum is so low that the mean free path length is enlarged from the order of 10^{-8} m at atmospheric pressure to the order of km [27]. The number of collisions at the sample surface therefore is reduced to a minimum and enables to study processes on atomically clean surfaces during several hours or days.

The Nanolab, see figure 2.1 and 2.2, consists of several individually pumped chambers which are separated by gate-valves. The chambers contain the tools for the various steps of sample preparation, molecular and metal deposition, analysis and sample transfer to the outer world [28–33]. All steps were performed in-situ. The partition into different chambers assures that the individual processes do not interfere with each other. An ingenious transport system allows the samples to reach all chambers.

2.2. Substrates

Well-defined substrates serve as support for the molecular layers. For practical uses, either single crystals with a certain orientation, see figure 2.3, or perfect grown metal films can be used. For this study, Ag(111) and Ag(100) films (see figure 2.3) were produced in-situ. After analyzing the metallic films, they were used for many experiments with molecules.

Ag(111) Preparation

The Ag(111) films with a surface lattice constant of 0.289 nm were grown hetero-epitaxially on air-cleaved Muscovite *2M*-1 mica substrates with predeposited Au pads. After introduction to UHV, the mica substrate was first annealed at 840 K for 2 h in order to obtain sharp

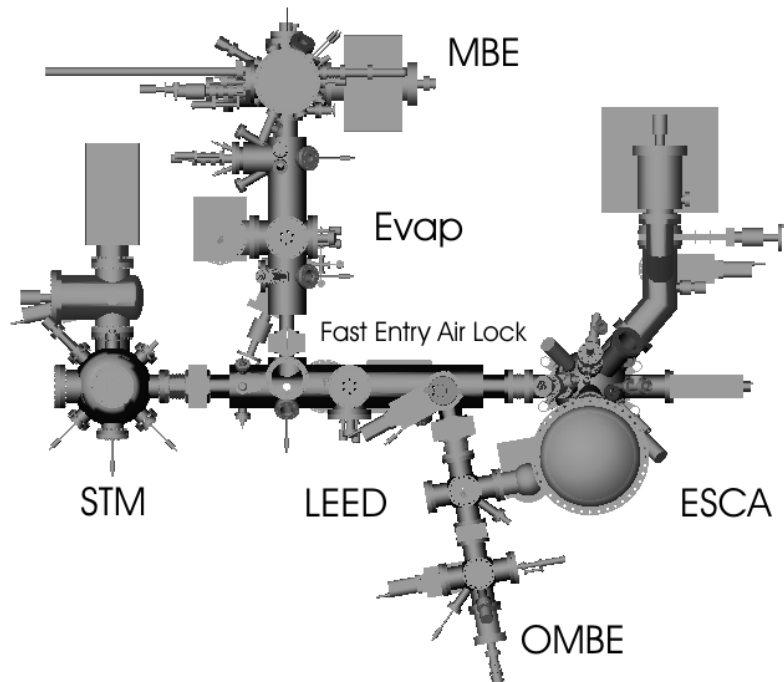


Figure 2.1.: The Nanolab: top view of the UHV system comprising the STM-, ESCA-, MBE-, LEED-, Evap- and OMBE-chamber. (Technical drawing by A. Heuri)

and clear hexagonal LEED spots. The silver layer was then deposited with an electron beam evaporator to a thickness of 120 nm, at a rate of 1 nm/sec and a pressure of $6 \cdot 10^{-8}$ mbar. The temperature of the mica during deposition was held at 570 K. Silver is reported to grow with atomically smooth surfaces [35] at this temperature, consisting of large step-free terraces. The Au from the contact pads is not visible in XPS measurements after the Ag deposition.

Before every new molecular experiment, the Ag(111) surface was cleaned by standard UHV techniques (repeated Ar^+ ion etching by 600 eV ions and post annealing to 573 K) which gave a well-ordered LEED pattern.¹

Ag(100) Preparation

Atomically clean Ag(100) surfaces were also used as substrates. In a first step, a GaAs(100) sample from a commercial wafer was introduced into UHV via the Fast Entry Air Lock. It then was heated to 850 K ($p < 1 \cdot 10^{-8}$ mbar) until sharp LEED spots were visible and indicated a clean, well-ordered crystallographic structure without contamination. Then a 1 nm thick Fe seed layer was deposited by MBE at 380 K with a rate of 0.01 nm/sec ($p \approx 3 \cdot 10^{-8}$ mbar). After that, a 150 nm thick Ag layer was epitaxially deposited at a constant rate of 0.1 nm/sec and 380 K sample temperature ($p \approx 1 \cdot 10^{-8}$ mbar). Finally, the Ag(100) sample was annealed at 620 K for 2 h and then analyzed in-situ by LEED, XPS and STM.

¹On the films, in contrast to single crystals, rings in the LEED pattern indicate different domains.

2. Instrumental Methods and Set-up

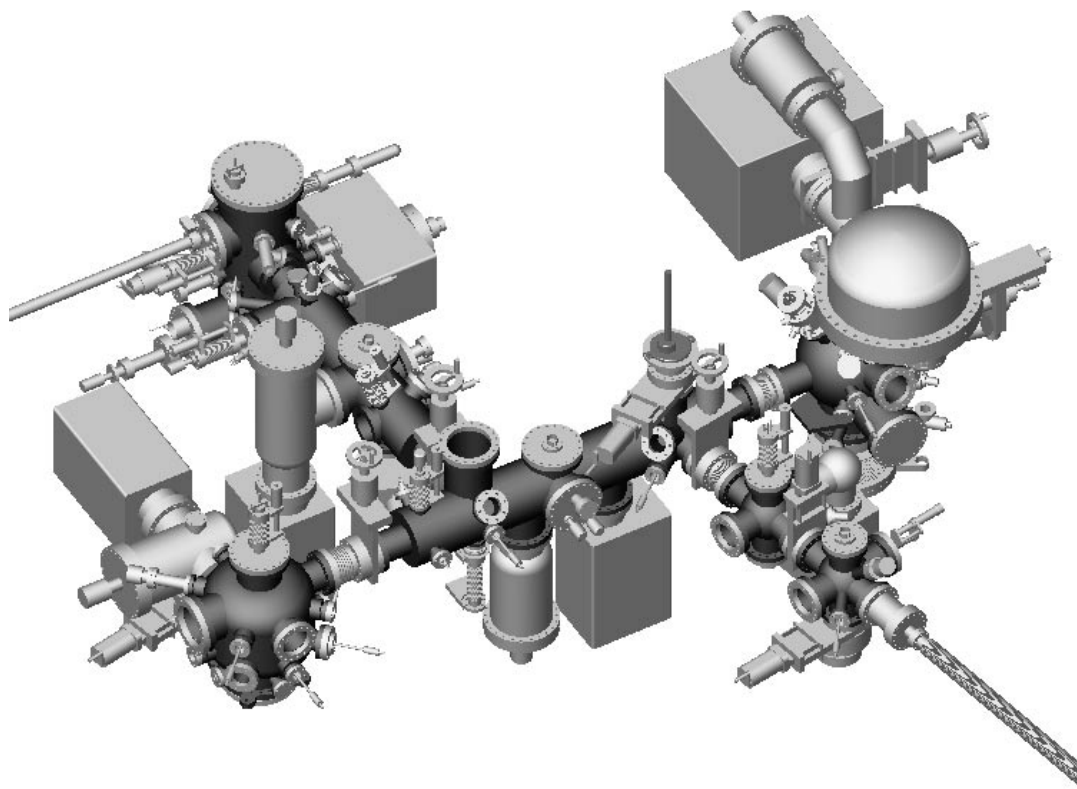


Figure 2.2.: 3D model of the Nanolab exposing the manifold features of the system. (Technical drawing by A. Heuri)

The films are characterized by atomically flat areas and large terraces (hundreds of nm), which grow in different domains.

Before every new molecular experiment, the Ag(100) surface was cleaned by standard UHV techniques (repeated Ar^+ ion etching by 600 eV ions and post annealing to 573 K) which gave a well-ordered LEED pattern.

2.3. Organic Molecular Beam Epitaxy (OMBE)

Ultrapure (99.99%) molecules are thermally deposited (by heating to 570–650 K) from tantalum crucibles at a rate of 0.5 to 1 ML min^{-1} onto atomically clean substrates that are kept at room-temperature. A chimney on the button heaters collimates the sublimating molecules into a narrow solid angle. The sublimators are outgassed for a long time in order to avoid impurities while depositing the films. The coverage, typically in sub-monolayer range, is measured with a water cooled microbalance at an accuracy of some percent of a

2.4. Scanning Tunneling Microscopy (STM)

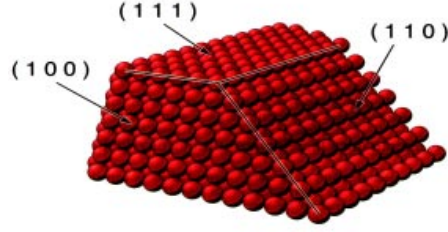


Figure 2.3.: Sphere model of a face-centered cubic single crystal with surfaces oriented (100), (110), and (111), each with specific symmetry and corrugation. From [34].

monolayer (ML). The film thickness can later be calibrated by core-level intensities in XPS measurements and coverage estimation in STM images. The pressure during the molecule-sublimation can rise up to $\approx 2 \cdot 10^{-8}$ mbar.

2.4. Scanning Tunneling Microscopy (STM)

The Scanning Tunneling Microscopy (STM), invented by Binnig and Rohrer in 1981 [22] (receiving Nobel Prize in 1986), delivers pictures of solid surfaces with atomic resolution. A direct real-space image of a surface is obtained by moving a tiny metal tip across a sample surface and recording the electron tunnel current between tip and sample as a function of the position [21, 36–39]. This finally makes it a powerful tool for us to study the orientational configurations of molecules grown on solid surfaces.

Tunneling is a genuine quantum mechanical effect in which electrons from one conductor penetrate through a classically impenetrable potential barrier – in the present case, the vacuum – into a second conductor [21, 36–40], see figure 2.4. The phenomenon arises from the “leaking out” of the respective wave functions into the vacuum and their overlap within classically forbidden regions. This overlap is significant only for atomic-scale distances and, in the first-order perturbation theory, the tunnel current, I_T , when a bias voltage V_{bias} is applied between the two electrodes, is expressed as

$$I_T = (4\pi^2 e/h) \sum_{s,t} |M_{st}|^2 [f(E_t) - f(E_s)] \delta(E_t + |e|V_{bias} - E_s) \quad (2.1)$$

where $f(E) = [1 + e^{\frac{E-E_F}{kT}}]^{-1}$ is the Fermi function, M_{st} is the tunneling matrix element between states ψ_s and ψ_t of the left and right electrodes respectively (tip and sample), calculated independently, E_s is the energy of ψ_s relative to the left-electrode Fermi level, and E_t is the energy of the ψ_t relative to the right-electrode Fermi level. The height of the potential barrier is the work function ϕ . For most purposes, the Fermi functions can be replaced by their zero-temperature values, i.e. unit step functions. In the limits of small voltages $V_{bias} \ll \phi$, this expression then further simplifies to

2. Instrumental Methods and Set-up

$$I_T = (4\pi^2 e^2 V_{bias}/h) \sum_{s,t} |M_{st}|^2 \delta(E_s - E_F) \delta(E_t - E_F). \quad (2.2)$$

Bardeen [41] showed that, under certain assumptions, the matrix element in equation (2.2) can be expressed as

$$M_{st} = (h/8\pi^2 m) \int d\mathbf{S} (\psi_s^* \nabla \psi_t - \psi_t \nabla \psi_s^*) \quad (2.3)$$

where m is the electron mass and the integral is over any surface lying entirely within the barrier region and separating the two half-spaces. Now the ideal STM tip would consist of a mathematical point source of current, whose position we denote \mathbf{r}_T . In that case, equation (2.2) for the current at a tip-sample separation distance d and small voltage V_{bias} would reduce to [42, 43]

$$I_T \propto \sum_s |\psi_s(\mathbf{r}_T)|^2 V_{bias} \delta(E_s - E_F) \equiv \rho_{x,y}(\mathbf{r}_T, E_F) V_{bias} e^{-2\kappa d}, \quad \kappa = \sqrt{8m\pi^2 \phi}/h \quad (2.4)$$

Thus the ideal STM would simply measure $\rho_{x,y}(\mathbf{r}_T, E_F)$, the local density of states (DOS) at E_F . The exponential decay of the signal leads to the unique resolution in tip-sample separation. Typically the current decays about one order of magnitude per Å. It is important to see how far this interpretation can be applied for more realistic models of the tip. Tersoff and Hamann [42, 43] showed that equation (2.4) remains valid, regardless of tip size, as long as the tunneling matrix elements can be adequately approximated with those for an s -wave tip wave function [38]. The tip position, \mathbf{r}_T , must then be interpreted as the effective center of curvature of the tip, i.e. the origin of the s -wave which best approximates the tip wave functions.

All images in this thesis were recorded using the constant current mode (“topographic” mode). In this mode, a feedback loop system is used to force the tip via a piezoelectric driver to be always at such a distance to the sample surface (≈ 1 nm) that the tunneling current flowing between these two electrodes remains constant. By recording the voltage, which has to be applied to the piezoelectric driver in order to keep the tunneling current constant, i.e. recording the height of the tip $z(x, y)$ as a function of the position, a “topographic” image can be obtained in this mode. This mode can be used for surfaces, which are not necessarily flat on the atomic scale, thus for stepped surfaces or adsorbate covered surfaces. The topographic height of the tip movement can be obtained directly, provided the sensitivity of the piezoelectric driver elements is known. A disadvantage of the constant current mode is the finite response time of the feedback loop, which limits the scan speed. A schematic illustration of the constant current mode is shown in figure 2.5. Another mode of operation, which was not used for this study, is the constant height mode. In this mode the tip is scanned at constant height over the sample surface while the feedback loop is slowed or turned off completely. The variations in the tunneling current, which are recorded as a function of location, then contain the height information. An advantage of this mode is the

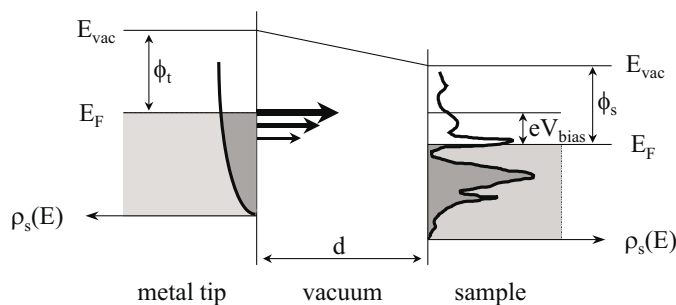


Figure 2.4.: Schematic energy diagram for the tunneling process from the tip to the unoccupied states of the sample. The two conductors are separated by the distance d , and the positive bias voltage V_{bias} is applied to the sample. The DOS of the tip and the sample are indicated as ρ_t , ρ_s , respectively. The size of the arrows in the tunneling gap represents the tunneling probability, described by the tunneling matrix element.

faster scan rate. This mode, however, is only applicable to atomically flat surfaces, thus not suited for molecular imaging.

For metals the local DOS $\rho_{x,y}(\mathbf{r}_T, E_F)$ is typically in good agreement with the topology. For adsorbates, however, the topology and the image obtained in constant current mode can differ completely due to a modified electronic situation. CO on Cu(211), for example, can appear as a protrusion or depression depending on the arrangement of the adsorbates and the presence of a CO molecule at the tip [44]. Similarly, the contrast of larger organic molecules is known to depend on its specific substituents [45]. The molecular corrugation also can be reversed upon tunneling within a specific range of the bias voltage [46]. A recent review [47] discusses the STM-contrast on adsorbates.

All measurements were done in-situ by a home-built room-temperature STM, using an electro-chemically etched tungsten tip which was cleaned in vacuum by electron bombardment heating. The voltage V_{bias} corresponds to the sample bias with respect to the tip, see figure 2.4. Here, tunneling from the tip into the unoccupied states of the sample was applied. For molecules this means tunneling into the LUMO. In the images, the slow scan direction is from bottom to top. The line scans were recorded in forward (left to right) and backward direction, with identical tunneling parameters. The architectural and electronic specifications of the STM used in the Nanolab are described in [28]. Details of the Eddy-current damping and the in-situ tip-change system can be found elsewhere [48].

2.5. Photoelectron Spectroscopy (PES)

Photoemission is nowadays one of the most widely used experimental methods in order to obtain important information of matter such as chemical composition, geometrical or electronic structure [49]. The phenomenon was discovered in 1887 by Hertz [50] and had become controversial for more than twenty years. In 1905, Einstein finally explained the

2. Instrumental Methods and Set-up

observation of Hertz by inclusion of the quantum nature of light [51], leading him to receive the Nobel Prize in 1922.

The principle of a photoemission process is sketched in figure 2.6. When matter is irradiated with photons, electrons may be excited to higher states, and if the excited electrons have an energy exceeding the work function, they can be emitted from the material. These electrons are called *photo-electrons* and their kinetic energy in vacuum, E_k , is given by the relation, (energy conservation)

$$E_k = h\nu - E_B - \phi \quad (2.5)$$

where $h\nu$ is the photon energy, ϕ is the work function of the solid and E_B is the binding energy of the initial electronic state. The binding energy is referenced by the Fermi level, E_F . Depending on the photon energy used, information on core levels (X-ray) or valence levels (ultraviolet, UV) of the sample electronic state is obtained. While the photoemission itself is described by Einstein, there have been many detailed theoretical studies on the process [49]. A semi-empirical approach [52], so-called three-step model, has been proven extremely useful in describing the photoemission from a solid. Unlike STM, this is a non-local method, but it allows quantitative analysis of the chemical composition and environment on a macroscopic scale.

Photoemission measurements were performed with an ESCALAB MK II from V.G. Scientific Ltd., GB, which is equipped with a hemispherical analyzer, aligned with a fixed angle to the incident photon beam. The angular acceptance can be controlled by an adjustable aperture. All photoelectrons come from within an area of about 4 mm by 4 mm. The energy

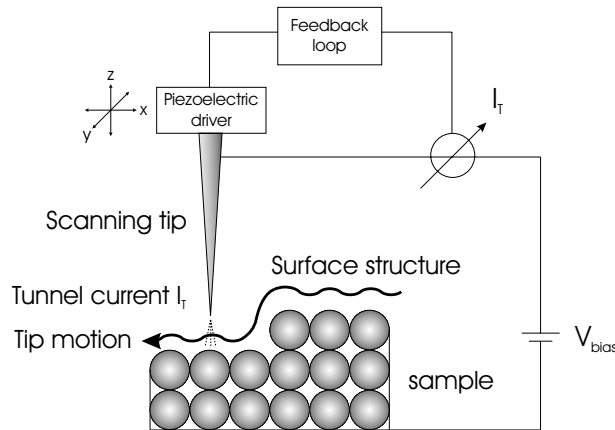


Figure 2.5.: Principle operation of the STM. (Schematic: distances and sizes are not to scale.) The tunneling current I_T which flows between the tip and the atomically flat and conducting sample when a constant bias voltage V_{bias} is applied, decays exponentially with the tip-sample separation. The tip motion in the scans with constant current mode, controlled by a feedback loop and piezoelectric elements, is indicated over a surface step.

2.5. Photoelectron Spectroscopy (PES)

scale is referenced towards the Fermi level E_F of a bulk Ag sample.

For X-Ray Photoemission Spectroscopy (XPS), photo-energies > 100 eV allow the measurement of the binding energy of core-levels states, chemical composition of surfaces and the study of chemical shifts which depends on the environment of the elements. XPS was done by using the Mg- K_α line with a photon energy of 1253.9 eV. The probing depth of XPS is in the order of 20-40 Å [53]. The molecular coverage of the sample was obtained by comparing the area of the C1s peak with the double peak of Ag3d [54].

For UV Photoemission Spectroscopy (UPS), photo-energies < 100 eV allow the study of valence bands and occupied molecular orbitals. Nonmonochromated He-I ($h\nu = 21.2$ eV) radiation was used for UPS measurements. Since UPS has a very low information depth (typically 5-10 Å, due to inelastic scattering [53]), we here focus on the contact region between the molecules and between the molecules and the substrate.

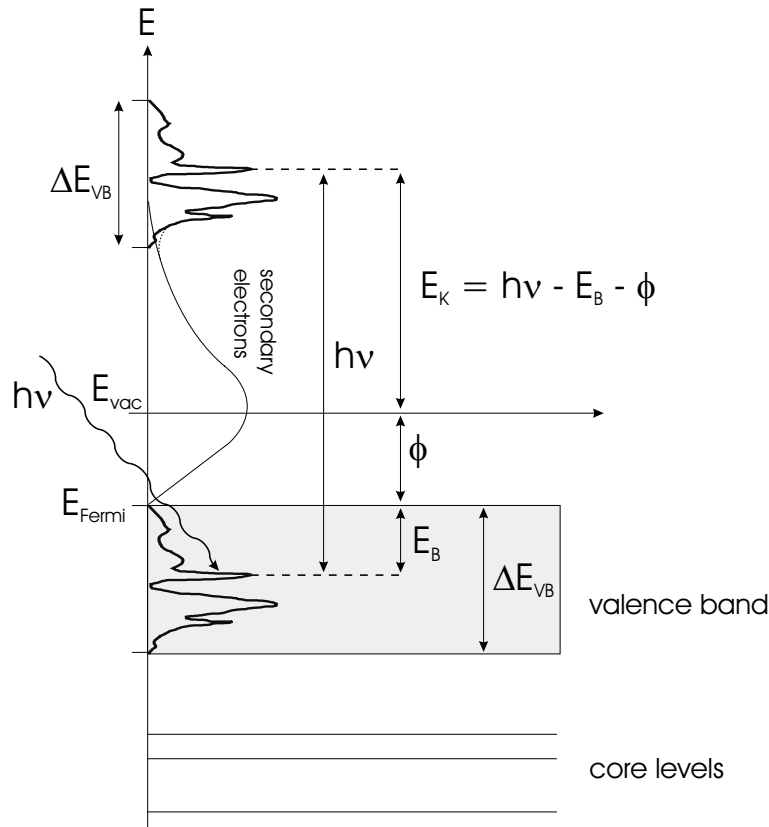


Figure 2.6.: Principle of Photoelectron Spectroscopy. The irradiated matter emits electrons with kinetic energy E_K if the photon energy $h\nu > E_B + \phi$ and is thereby mapping the occupied energy levels of the solid.

2.6. Introduction to Molecular Modeling

Molecular modeling is the science (and art) of representing molecular structures numerically and simulating their behavior with the equations of quantum and classical physics. Computational chemistry programs allow scientists to generate and present molecular data including geometries, energies, electronic properties, spectroscopic properties and bulk properties.

The starting point for many computer assisted molecular studies is generally a two dimensional drawing of a compound of interest. These diagrams can range from "back-of-the-envelope" sketches to electronically stored connection tables in which one defines the types of atoms in the molecule, their hybridization states and intramolecular bonds.

Connection tables are easily stored and searched electronically. However, they must be transformed into three dimensional representations of chemical structure to study chemical properties. Chemists use the mathematical descriptions of the rules of physical chemistry which are contained in quantum mechanics and molecular mechanics to accomplish this task.

In its purest form, quantum theory uses well known physical constants such as the velocity of light, values for the masses and charges of nuclear particles and differential equations to directly calculate molecular properties and geometries [55]. This formalism is referred to as *ab-initio* (from first principles) quantum mechanics.

The equation from which molecular properties can be derived is the Schrödinger equation, $H\psi = E\psi$, where E is energy of the system relative to the situation in which all atomic particles are separated to infinite distances, ψ is the wavefunction which defines the Cartesian and spin coordinates of the atomic particles and H is the Hamiltonian operator which includes terms for both, potential and kinetic energy. Unfortunately, the Schrödinger equation can be solved only for very small molecules such as hydrogen and helium. Approximations must be introduced in order to extend the utility of the method to polyatomic systems.

The first approximation attempts to differentiate nuclei and electrons. It assumes that nuclei are much heavier than electrons and move much more slowly so that molecular systems can be viewed as electrons moving in a field of fixed nuclei (the Born-Oppenheimer approximation). Solutions to the Schrödinger equation using this assumption lead to values of effective electronic energy which are dependent on relative nuclear coordinates.

The second approximation allows the wavefunction ψ to be represented as the product of one-electron (or spin) orbitals which are described by a set of basis functions. This formalism is called *Linear Combination of Atomic Orbitals* theory. Once the molecular orbitals have been derived, the orbital coefficients (which define the energy of the system) are calculated. Hartree-Fock theory is used to accomplish this goal. Hartree-Fock assumes that the energy of a set of molecular orbitals can be derived from the basis set functions describing the orbitals by a set of adjustable coefficients which are used to minimize the energy of the system.

Walter Kohn showed in 1964/65 that the energy of a quantum-mechanical system is uniquely determined by its electron density. This quantity is more easily handled than the complicated wave-function in the Schrödinger equation. Kohn also provided a method which made it possible to set up equations whose solution give the system's electron density and energy. This method, called *Density Functional Theory* has become widely used in chemistry

since, because of its simplicity, it can be applied to fairly large molecules [56]. It provides a good accuracy as long as the electron correlation is small.

In general, ab-initio methods are able to reproduce laboratory measurements for properties such as the heat of formation, ionization potential, UV/Visible spectra and molecular geometry. Ab-initio quantum methods compute a number of solutions to a large number of equations [57]. John A. Pople (Noble Prize Chemistry 1998) has developed this computational method. The methods were made available to researchers through e.g. the *Gaussian-98* ab-initio program. While recent publications have reported calculations on large molecules [58], the methods are generally limited to compounds containing between ten and twenty atoms due to the amount of computer time required for each calculation and the large amount of disk space needed to store intermediate data files. Physical/theoretical chemists have developed alternative approaches to computing structures and properties by simplifying portions of the calculation to circumvent these limitations. These methods are collectively named *semi-empirical* quantum methods.

Semi-empirical methods utilize approaches which are similar to ab-initio methods, but several approximations are introduced to simplify the calculations [59]. Rather than performing a full analysis on all electrons within the molecule, some electron interactions are ignored. These methods include the Hückel approach for aromatic compounds (in which the outer electrons in conjugated systems are treated, but the inner (or core) electrons are ignored, fixed geometry).

While semi-empirical methods require less computer resources than ab-initio methods, they are still compute intensive. In general, calculations are routinely performed on compounds which contain up to 100 atoms. The chief drawback of the method is that its application is limited to systems for which appropriate parameters have been developed. The computational requirements for quantum mechanical approaches on molecules consisting of several thousands of atoms (proteins, drug candidates) render these methods unusable for routine analysis. Thus, a further simplification in the way molecular geometries and their associated properties are computed is required. This approach is the *Molecular Mechanics* or *Force Field* method.

Rather than utilizing quantum physics, the method relies on the laws of classical Newtonian physics and experimentally derived parameters to calculate geometry as a function of steric energy. In contrast to ab-initio methods, molecular mechanics is used to compute molecular properties which do not depend on electronic effects (geometry, rotational barriers or vibrational spectra). Since the calculations are fast and efficient, molecular mechanics can be used to examine systems containing thousands of atoms. However, unlike ab-initio methods, molecular mechanics relies on experimentally derived parameters so that calculations on new molecular structures may be misleading.

On SubPc, AM1 semi-empirical calculations as well as ab-initio density functional calculations using the B3LYP exchange-correlation functional at the 6-31Gd level [60, 61] were performed, complementing earlier work [62–64]. The charge distribution, electrostatic potential, dipole moment and all molecular orbitals including the HOMO and LUMO are calculated. On Perylen, also ab-initio density functional calculations using the B3LYP exchange-correlation functional at the 6-31Gd level [60, 61] were done to calculate the same properties.

3. Self-Assembly of Phthalocyanines and C₆₀ on Ag(111)

In this chapter, a novel route to highly perfect molecular self-assembly through competing interactions of a bi-molecular system on a metallic surface is presented. After some introductory remarks on the topic of self-assembly in section 3.1, both molecules of the binary mixture are presented separately in section 3.2. Then the novel two-component phases are described: Depending on the relative surface coverage of the two species, Subphthalocyanine and C₆₀, well-ordered intermixed monolayers consisting of pseudo-linear C₆₀-chains (section 3.3) or 2D hexagonal patterns with periodic vacancies (section 3.4) are formed. The structural parameters and schematic binary “phase-diagram” of this system, which are deduced from detailed room-temperature STM studies, are discussed in section 3.5.

3.1. Molecular Self-Assembly and 2D Layering

The term *self-assembly* was coined by G. M. Whitesides [65] and covers a broad range of examples from different fields:

“Molecular self-assembly is the spontaneous association of molecules under equilibrium conditions into stable, structurally well-defined aggregates joined by non-covalent bonds. Molecular self-assembly is ubiquitous in biological systems and underlies the formation of a wide variety of complex biological structures.”

In a recent talk [66], he further characterized this phenomenon: In self-assembling processes, individual objects act quasi-individual and the results contain complex effects which cannot easily be understand (comparable to traffic, stock exchange, thunderstorm). Molecular self-assembly is a powerful method for assembling atomically precise material and devices. Biological organisms are composed of molecular building blocks, such as nucleic acids, proteins, and phospholipids, and are equipped to assemble these components into extremely well-organized structures – namely themselves. Self-organized systems are in the focus of nanotechnology research because of their potential use in the parallel “bottom-up” creation of functional supramolecular structures [67–69]. Self-assembling systems [65] will be required in order to efficiently produce nanoscale molecular electronic devices (“Let’s Nature do the job”) and to create patterned molecular layers for a broad range of applications such as molecular data storage.

Molecular self-assembly has been shown to depend on intermolecular and on molecule-substrate interactions [70–72]. When molecules are deposited onto clean metallic surfaces, they can show a rich variety of phenomena [73]. The present interaction determine the growth, ordering and diffusion of the molecules on the substrate. In the experiments presented here, the molecules are bound to the substrate [74] and do not desorb to the vacuum. But due to the small corrugation of the surface potential, they can to some extent

3.1. Molecular Self-Assembly and 2D Layering

diffuse within a 2D confinement, as was exemplified in [75, 76]. This diffusive mobility ensures that lateral intermolecular interactions can play a significant role in adsorbate ordering. Such noncovalent intermolecular interactions are critical to an understanding of a wide range of disciplines from molecular biology to materials science [77]. In crystal engineering, supramolecular synthesis utilizes hydrogen bonding and other interactions including halogen-halogen, electrostatic interactions, and weak electron donor-acceptor complexation to organize molecules within a crystal [78–80]. When the concepts of 3D supramolecular synthesis are applied to the 2D case of physisorbed molecules on metal surfaces, the adsorbate-substrate interaction plays a role of equal importance with that of the intermolecular interactions [81]. The weak lateral forces exerted by the surface upon physisorbed molecules, and the image charges that occur in metal substrates, allow the weak intermolecular forces to play a significant role in the formation of long-range order in the adsorbed phase. An example of weak intermolecular interactions combined with physisorption comes from the STM study of DNA base molecules on Cu(111) [82]. DNA bases form superstructures on Cu(111) surfaces through intermolecular hydrogen bonding and their planar orientation on the surface. The relative inertness of Cu(111) allows the molecules to diffuse over the surface to spontaneously self-assemble into small clusters and chains. Further, the Langmuir-Blodgett (LB) technique relies on the weak Van der Waals interaction of long hydrophobic molecules on top of a water surface [83–85], whereas the formation of Self-Assembled Monolayers (SAM) is driven by the strong selective bonding of a head group (mostly thiols) to a metal (mostly Au(111)) or a semiconductor surface [86]. The SAMs are a well established technique to produce 2D molecular crystals with variable properties by specially designing the molecular length and end-groups. Very recently, Yokoyama and co-workers [68] have observed similar small clusters and chains on Au(111) at 63 K. In this study, cyanophenyl-substituted porphyrins were found to form three-molecule clusters in the case of single substitution, four-molecule clusters for asymmetric double substitution, and branching chains for symmetrical double substitution. While these reports on DNA bases and substituted porphyrins are encouraging for 1D aggregation, they do not represent practical examples of 2D supramolecular structures. There are also reports [87] of highly ordered 2D structures at the solution-graphite interface where solvent and solute adopt well-defined bimolecular structures. Strongly ordering chemisorbed systems such as CO/NO + C₆H₆ (benzene) adsorbed on Pt, Rh, Ni and Pd [88–95] or CO and NH₃ (ammonia) on Ru(001) [96] or CO/NO and C₂H₃ (ethylidene) on Rh(111) [97] are not appropriate models for the non-covalent interactions envisaged here because both species undergo significant bonding with the used metal substrates.

Here, a novel route to self-assembly of highly perfect binary molecular monolayers on a metallic surface through competing non-covalent interactions is presented. These novel “Self-Intermixed Monolayer Phases” (SIMP) are different from previously known self-assembled molecular monolayers in that they form intermixed patterns at room temperature on uniform, unreconstructed atomically clean terraces. Unlike in SAM and LB films, the intermixed molecules do not segregate [98–100]. In contrast to former two-component experiments [81], the individual loosely-packed components are easily discriminable because of their specific symmetries. Therefore, experiments e.g. towards single molecular storage application are straightforward.

3.2. Single Component Phases: Phthalocyanines and C_{60} on Ag(111)

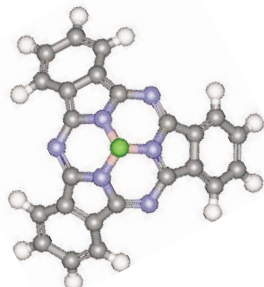


Figure 3.1.: Structure of Chloro[subphthalocyaninato]boron(III) (SubPc). Colors specify different elements: C, dark gray; Cl, green; H, white; N, blue; B, pink, hidden by the Cl. The height is approximately 0.5 nm, the diameter ca. 1.3 nm.

The growth and self-organization of pure monolayer islands of the individual components sublimed onto Ag(111) have been studied previously by STM [33, 75]. The first component, Chloro-[subphthalocyaninato]-boron(III) (SubPc) [101], is a polar molecule with a characteristic triangular symmetry (figure 3.1). It is the lowest phthalocyanine homologue with unusual electrical and optical properties [102]. These compounds are only known as boron derivatives. In contrast to planar four-fold symmetric phthalocyanines, here, the center metal atom is replaced by a boron-chlorine unit which binds three instead of four isoindol-residues. Therefore the SubPc molecule has a C_{3v} symmetry. Due to the sp^3 bonded boron it is non-planar but nevertheless has an aromatic 14- π -electron system. The synthesis of SubPc was made by Meller and Ossko in 1972 [101] and 2 years later its structure was determined by Kietaihl [103] using X-ray diffraction. In the next 15–20 years great progress for the structural characterization of the SubPc molecules was not achieved even though a notable group of SubPc derivatives was synthesized [104, 105]. One of the most striking features of the X-ray crystal structure is the presence of pairs of SubPc molecules in Van der Waals contact [102]. In a secondary organization, the SubPc pairs form a sheet in which the concave faces point inward and the axial groups point outward toward the next sheet.

In STM images the SubPc molecules appear as three-lobed objects. Individual phenyl-rings can be recognized in STM images with submolecular resolution, see figure 3.2. SubPc molecules adsorbed on Ag(111) self-organize into a honey-comb pattern [33], see figure 3.3. Furthermore, subphthalocyanines can be organized at the supramolecular level in liquid crystals and LB films [102]. They are considered as useful molecules that could act as recording media for DVD-R applications [106] and could be employed for rewriting at short wavelength (purple color: The calculated HOMO-LUMO gap is 2.7 eV and fluorescence measurements in a dimethylholamide solution give a value of 2.2 eV [62]).

The second component is the well-known C_{60} carbon fullerene¹ [107] (figure 3.4). Since

3.2. Single Component Phases: Phthalocyanines and C_{60} on Ag(111)

the discovery of a method for synthesis of C_{60} molecules in macroscopic quantities [108],

¹Also called Buckminsterfullerene, Buckyball, C_{60} Fullerene, Carbon cluster (C_{60}), Follene-60, Footballene, Footballene (C_{60}), Icosahedral C_{60} , Soccerballene or [5,6]Fullerene C_{60} .

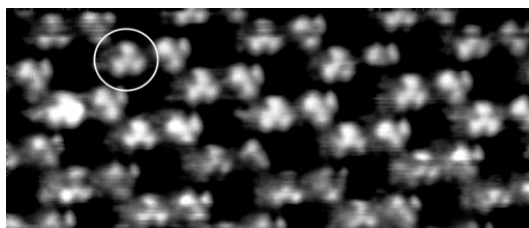


Figure 3.2.: SubPc adsorbed on Ag(111). A single molecule is marked by a circle. The three sub-units of a molecule represent the phenyl-rings [62]. Scan range 21 nm x 9 nm. $V_{bias} = 2$ V, $I_t = 200$ pA.

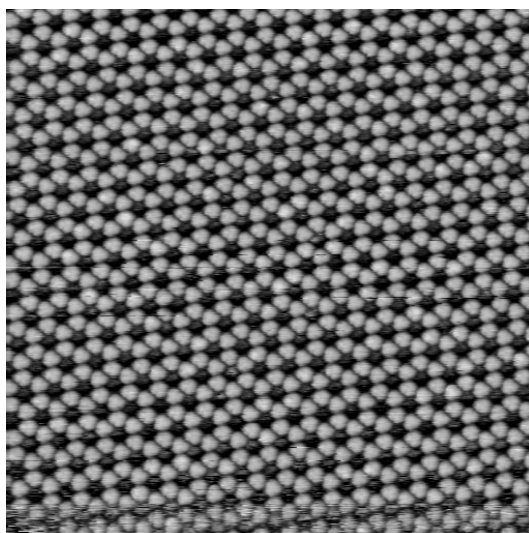


Figure 3.3.: A monolayer of SubPc on Ag(111): The molecules are arranged in a hexagonal honey-comb pattern [75]. Scan range 56 nm x 56 nm. $V_{bias} = 1.3$ V, $I_t = 200$ pA.



Figure 3.4.: Structure of C_{60} . The diameter of the carbon cage is approximately 7 Å.

3. Self-Assembly of Phthalocyanines and C_{60} on Ag(111)

great activity has been directed toward the understanding of the growth and structural properties of C_{60} layers. Much interest has been focused on the interfacial properties of these layers in contact with various surfaces [109]. In particular, because of charge transfer across C_{60} -metal interfaces, structures composed on these interfaces have attracted considerable attention [110].

The carbon atoms of each C_{60} molecule have a pentagon-hexagon arrangement. The hexagonal pattern is found in graphite which exhibits sp^2 bonding characteristics. However, to allow the molecule to curve around to form a sphere, pentagonal bonding is also present. This introduces some sp^3 hybridization. One feature of this molecule is that all the valence electrons are involved in C-C bonding with no unpaired electrons left over giving a closed-shell electronic structure. In its bulk form, fullerite, C_{60} molecules interact with each other via weak van der Waals forces. The energy gap between the lowest unoccupied molecular orbital (LUMO) and the highest occupied molecular orbital (HOMO) is 1.9 eV. C_{60} therefore is an intrinsic semiconductor. As for other semiconductors, the electrical characteristics may be altered by doping with atoms of different species. Due to the electrophilic (the LUMO is three fold degenerate) nature of C_{60} , much attention has been given to doping fullerene crystals to form n-type semiconductors, metals or superconductors [111].

The threefold degenerated LUMO is shown in figure 4.1 in section 4.1. In the room-temperature STM images, however, the fullerenes appear as spheres and no details from the intramolecular structure are visible. This is due to the vibrational modes of the molecules at room-temperature, which are fast compared to the scanning speed [112] (see also section 4.4.1).

The ultra-pure C_{60} with a density of 1.65 g/cm³ [113] were sublimed at approximately 650 K. The growth and self-organization of C_{60} on Ag(111) have been studied previously by STM [112, 114, 115]. C_{60} sublimed onto Ag(111) form close-packed islands with $p6mm$ symmetry which are found to be rotated $\pm 30^\circ$ against the Ag lattice [116], see left side of figure 3.6 and figure 3.7. It is a commensurate $(2\sqrt{3} \times 2\sqrt{3})R \pm 30^\circ$ structure and is the most stable phase of C_{60} adsorbed on Ag(111) [115]. The lattice mismatch of these C_{60} (111) islands is -0.2% at room-temperature and all molecules are adsorbed at hollow sites [116].

3.3. Mixture of C_{60} and SubPc: 3:2-Stripe Phase

C_{60} and SubPc co-deposited onto the atomically clean Ag(111) substrate are observed to self-organize into periodic 2D patterns at room-temperature. In typical STM images (figure 3.5), individual molecules within ordered patterns can be clearly identified by their characteristic triangular or round shapes, which match those determined in previous STM studies [62, 75, 112, 116]. The highly anisotropic arrangement of the molecules on the right hand side of figure 3.6 consists of zigzag rows of SubPc molecules (green) separated by quasi-linear chains of C_{60} molecules (yellow). Within these rows, the C_{60} molecules are grouped into aligned triplets, where the center molecule is sandwiched between two SubPc molecules. Remarkably, in this self-assembled pattern, a significant fraction of the surface between the molecules remains uncovered (appears dark in figure 3.5 and figure 3.6). In this phase, the molecules intermix at a fixed ratio of SubPc: C_{60} = 2:3. Alternating C_{60} chains and SubPc

3.3. Mixture of C_{60} and SubPc: 3:2-Stripe Phase

zigzag rows form a 2D periodic “*stripe pattern*” which belongs to the planar space group $p2$. The stripes are parallel to the close-packed C_{60} rows of an island of the hexagonal phase of C_{60} on Ag(111) [116], which appears on the left side of figure 3.6. These close-packed rows of the pure C_{60} layer are parallel to the $[\bar{1}\bar{1}2]$ direction of the substrate and can thus be used to identify the orientation of the *stripe* pattern. Such coexisting C_{60} islands are formed next to the mixed phase when the C_{60} content of the deposited film exceeds a critical ratio. The C_{60} within the hexagonal phase occupy highly-symmetric threefold-hollow sites [116] of the underlying Ag(111) substrate, and thus the molecules in the mixed layer have a definite registry with respect to the substrate lattice i.e. they adapt to the atomic corrugation of the surface potential. Nevertheless, the observed self-intermixing assembly requires a sufficient mobility of each component at 293 K. Previous authors have reported significant room-temperature diffusion of C_{60} on some metals. On Ag(111) this diffusion is manifested via the growth of islands from step edges [112]. For SubPc, the room-temperature coexistence of ordered islands with patches of mobile molecules in a 2D “lattice gas”-phase has been reported recently [75]; a similar 2D gas-phase is observed (see figure 3.10 in section 3.4.2). The mobility of the molecules is further supported by time lapsed-images in the vicinity of vacancy defects, as exemplified by the split appearance of the C_{60} molecule marked red (at the top of figure 3.6). The STM data confirm the perfection of the atomic and molecular arrangement of the substrate and of the grown binary layers: virtually no substitutional defects or additional adsorbates appear on the extended ordered terraces. This is a prerequisite to recognize details of the complex self-organization.

Clearly, the intermolecular interactions between SubPc and C_{60} are producing an entirely new 2D crystalline structure that is energetically favored over the patterns resulting from either parent component.



Figure 3.5.: Self-intermixed monolayer on Ag(111) and its molecular components. Artificially colored Scanning Tunneling Microscopy image of the basic unit of the molecular *stripe* pattern with superimposed schematic contours (SubPc green, C_{60} yellow). Individual components can be identified by size and shape. Scan range 4.3 nm x 3.2 nm. $V_{bias} = 1.3$ V, $I_t = 20$ pA.

3. Self-Assembly of Phthalocyanines and C_{60} on Ag(111)

3.3.1. Adsorption Geometry of the Stripe Pattern

A model of the registry is given in figure 3.7. The model is based on a thorough analysis of STM images with different phases. The known hexagonal close-packed phase of pure C_{60} molecules and the honeycomb pattern of pure SubPc molecules are used as references. Images with two different phases were surveyed for angles and distances. The stripes grow in

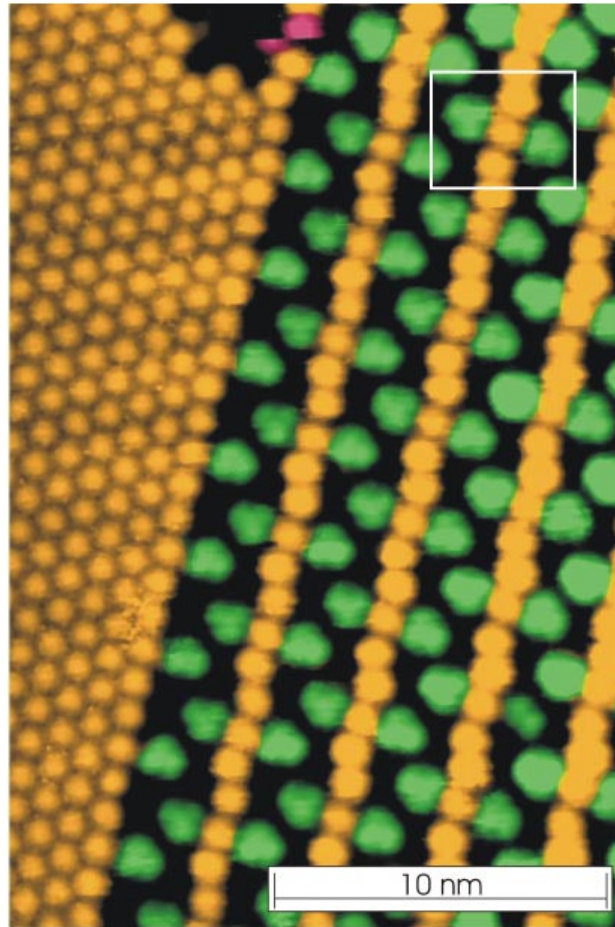


Figure 3.6.: Self-intermixed monolayer on Ag(111): Artificially colored STM image of a monolayer of co-adsorbed SubPc and C_{60} on Ag(111) (imaged area, 17 nm x 25 nm, $V_{bias} = 1.3$ V, $I_t = 20$ pA). The self-intermixed *stripe* phase is shown on the right with alternating C_{60} chains (yellow) and SubPc rows (green). The bare substrate areas appear dark. The distance between adjacent parallel C_{60} rows is 3.3 nm. Up to 38 parallel stripes with a length of 100 nm have been observed. The monoclinic unit cell of $p2$ symmetry contains three C_{60} and two SubPc molecules. One C_{60} molecule, colored in red near the top edge of the C_{60} island, jumped to an adjacent site between two horizontal scans. A pure C_{60} island coexists on the left hand side.

3.3. Mixture of C_{60} and SubPc: 3:2-Stripe Phase

Characteristics	Experiment	Model
molecular spacing in pure C_{60}^{hcp} -islands	1.0 ± 0.1 nm	1 nm
inter-row spacing \perp stripes	3.3 ± 0.3 nm	3.32 nm
SubPc–SubPc distance \parallel stripes	3.0 ± 0.3 nm	3.0 nm
centerhole–centerhole distance in <i>star</i> pattern	5.7 ± 0.5 nm	5.2 nm
\angle (C_{60} -triplet, stripe-axis)	$\pm 8 \pm 1^\circ$	$\pm 8.2^\circ$
\angle between holes in <i>star</i> pattern (section 3.4)	$60.5 \pm 1^\circ$	60°
\angle (holes in <i>star</i> pattern and stripes)	$90 \pm 1^\circ$	90°
\angle (honey-comb axis, stripe axis)	$84 \pm 1^\circ$	84.5°
\angle (C_{60}^{hcp} -axis, $C_{60}^{stripe-center}$ -axis)	$9 \pm 1^\circ$	10°
\angle (<i>stripe</i> domains)	$60 \pm 1^\circ$	60°
\angle (honey-comb holes, <i>star</i> holes)	$68 \pm 1^\circ$	65°
\angle (honey-comb holes, honey-comb holes)	$60 \pm 1^\circ$	60°
\angle (honey-comb chiral domains) [33]	$9 \pm 1^\circ$	9.42°

Table 3.1.: Comparison between the experimental data and the theoretical analysis of the registry model.

lots of domains that can differ in the angle and the phase, see figure 3.8. This gives further insight to the substrate-overlayer relationship. The comparison of the measurements with the model (figure 3.7 and 3.13) is given in the table 3.1. The results correlate perfectly, although it is not possible to image the substrate simultaneous with the adsorbates and an error has to be taken into account.² The model perfectly fits in geometry (distances and angles) within all phases (C_{60}^{hex} , SubPc^{*honey-comb*}, *stripe*-phase and *star*-phase (presented in section 3.4)). Here, all SubPc molecules are located at identical adsorption sites (center *on-top*) and have the same appearance in STM images.

Remarkably, in this model the three C_{60} molecules within a triplet have not the same adsorption site with respect to the underlying substrate: The corner fullerenes still are adsorbed in hollow positions like in the pure island, whereas the center fullerene of a triplet now is located on-top. This different adsorption-geometry may lead to different electronic bonding between adsorbate and substrate and therefore to a different appearance in STM. Quite often in STM studies of molecular films, it is possible to recognize different appearances of molecules, i.e. to recognize molecules with a variation in the apparent height [114]. Since STM maps the local density of states (see equation (2.4)), it is controversial whether the brightness difference is related either to a real difference in height (i.e. molecules are pushed out) or to an electronic effect (i.e. a spatially non-homogeneous charge transfer). Here³ on Ag(111), bright molecules can also have different bonds in equivalent adsorption sites [112, 117]. In the case of Ag(100), see section 4.4.1, the different structures are not due to geometric effects, but to non-homogeneous charge distribution and different chemical bonding with the Ag substrate [117]. On Al(111), the observed non-equivalent adsorption

²The STM was calibrated with a Si(111)7x7 sample, but at least 5% error in the lateral accuracy have to be allowed.

³and also in the case of Au(111)

3. Self-Assembly of Phthalocyanines and C_{60} on $Ag(111)$

sites are due to the surface reconstruction [118], whereas on $Au(110)$, the C_{60} adsorption induces a cooperative self-assembly of Au atoms and C_{60} [109].

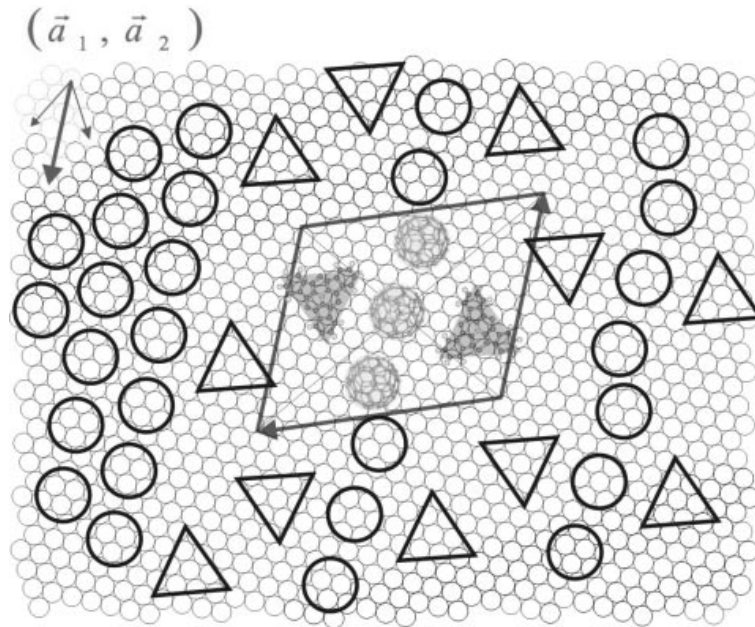


Figure 3.7.: Proposed model for the registry of the *stripe* phase on $Ag(111)$. The positions and the orientations of the C_{60} and SubPc molecules are depicted on the atomic silver lattice.

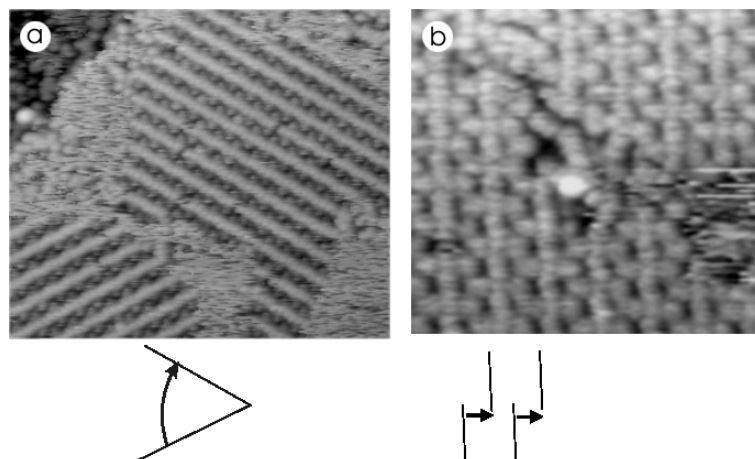


Figure 3.8.: **a)** Rotational and **b)** translational domain shifts of the *stripe* phase in accordance with the hexagonal (111) substrate (60° in a), resp. 1.7 nm in b) which means a shift by 6 Ag sites). Scan range a) 56 nm x 48 nm, b) 23 nm x 21 nm.

3.3.2. Chiral Supra-Molecular Structures of Achiral Molecules

Chiral is the Greek expression for *hands* and was used the first time by Louis Pasteur 1847 to describe macroscopic crystals that are its mirror images.⁴ Chirality is a geometrical property that plays an important role in physics, biology and chemistry. Two chiral forms of the same molecule can have extremely different properties: The taste of an orange and a lemon arise from the same molecule but with different chirality. Likewise the taste of caraway and spearmint. Two different enantiomers (chiral forms) have identical physical properties (such as boiling and melting point, density, spectroscopic and chromatographic features) and are spectroscopically not distinguishable, but sometimes well with STM. Recent results give more insight into the mechanism of chiral recognition [119–121].

Two mirror-symmetric species of the *stripe* pattern exist: The C_{60} -triplets are turned out of the overall row axis by 8° either clockwise or counterclockwise. Therefore I can clearly distinguish between λ (left) and ρ (right) domains which differ by a mirror operation. Interestingly, within one domain I can only find one chiral form, that means the chirality is strictly correlated. The reason might be found in the growth-process of an island: The first grown stripe probably defines the chiral form, then the following accretion has to suit it, see also section 3.5. Here, homochiral chains are formed by achiral molecules. These superstructures show adsorption-induced chiral motifs, a phenomenon that is called “organizational chirality” [122].

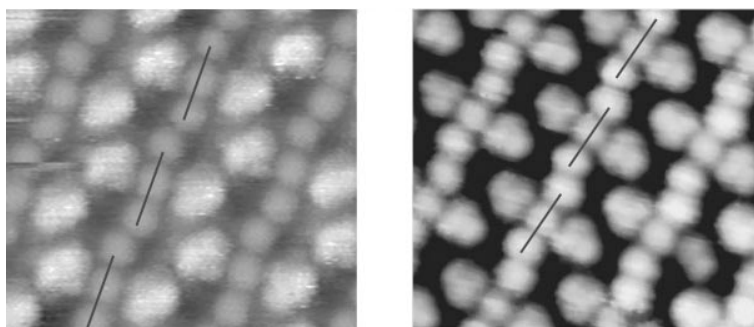


Figure 3.9.: Mesoscopic chirality segregation into λ and ρ domains of the *stripe* pattern: Enantiomorph supramolecular structures are formed by a chiral packing of achiral molecules. The scan ranges are approximately 10 nm x 10 nm. In both scans $V_{bias} \approx 1.3$ V, $I_t \approx 20$ pA.

3.4. Mixture of C_{60} and SubPc: Binary 1:1-Star Phase

A higher fraction of SubPc in the co-deposition process leads to a distinctly different pattern. Figure 3.10 shows the previous *stripe* phase (I) co-existing with a new hexagonal “*star phase*”

⁴As a graduate student, he was studying two acid-crystals in the dregs of wine with identical chemical composition but different optical properties.

3. Self-Assembly of Phthalocyanines and C_{60} on $Ag(111)$

(II). The triangular sub-unit (figures 3.11 and 3.12) of the hexagonal pattern consists of a C_{60} trimer which is surrounded by three SubPc molecules pointing towards center holes. The mixing ratio of SubPc: C_{60} in this pattern is 1:1. Between these two patterns (figure 3.10, I and II), irregular streaks of comparable height are clearly visible (figure 3.10, III). These streaks can be identified as mobile molecules in a 2D gas phase which diffuse faster than the imaging process, for more details see section 3.4.2, using the analysis recently applied to pure SubPc monolayers [75].

The self-assembled mixed monolayers observed here (*star* and *stripe* patterns) are distinctly different from previously known 2D molecular self-assembled or otherwise ordered binary layers. The ratio and relative positions of the components and the periodicity in the monolayer are maintained within large domains that are stable at room-temperature. Moreover, the spacing and orientation of the SubPc molecules suggests a special ordering mechanism. Therefore, I introduce the term “Self-Intermixed Monolayer Phases” (SIMP) for the novel co-adsorbed structures observed here.

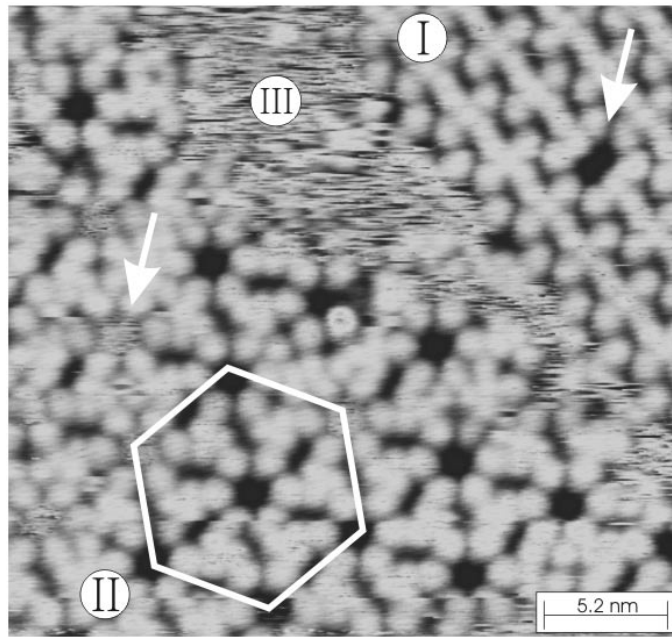


Figure 3.10.: Self-Intermixed Monolayer Phases (SIMPs): coexisting *star* and *stripe* patterns. This STM image shows two different SIMPs of SubPc and C_{60} on $Ag(111)$ (imaged area, 34 nm x 34 nm, $V_{bias} = 1.9$ V, $I_t = 20$ pA). On the right hand side, the 3:2-*stripe* SIMP (I) and on the left hand side, the hexagonal 1:1-*star* SIMP (II) is observed. Point defects are marked by arrows (top right: a vacancy defect is interrupting a C_{60} row; left: a center hole is filled with a molecule). Apparently random tip excursions of single molecular height (III) are visible between the two ordered regions and are identified as mobile molecules in a 2D gas phase [75].

3.4. Mixture of C_{60} and SubPc: Binary 1:1-Star Phase

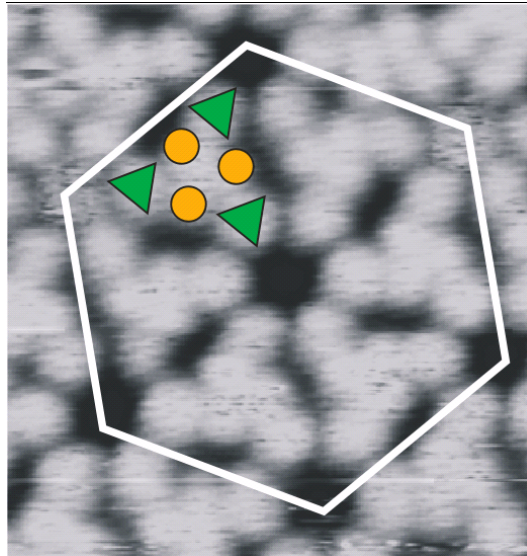


Figure 3.11.: STM image of a hexagonal cell in the *star* SIMP, with superimposed schematic shapes. A C_{60} triplet is surrounded by three SubPc molecules. Through a vacancy in the center, the level of the Ag substrate is imaged. Scan range 11.5 nm x 11.5 nm, $V_{bias} = 1.9$ V, $I_t = 20$ pA.

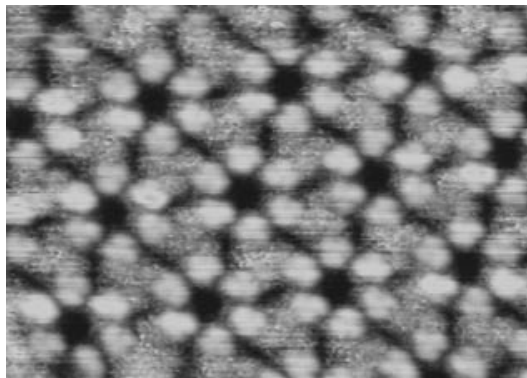


Figure 3.12.: With a good STM tip, the intramolecular structure of the SubPc molecules can be resolved and their orientation within the pattern is unravelled. Scan range 17 nm x 12 nm, $V_{bias} = 1.9$ V, $I_t = 20$ pA.

3. Self-Assembly of Phthalocyanines and C_{60} on $Ag(111)$

3.4.1. Adsorption Geometry of the Star Pattern

Based on the analysis presented in section 3.3.1 and table 3.1, the following registry model for the 1:1-*star* phase is proposed, see figure 3.13. It is a commensurable $(18 \times 18)R0^\circ - 2(3\text{SubPc} + 3C_{60})$ structure. Note that the allocation to the exact adsorption sites and the molecular orientations remain rather speculative.

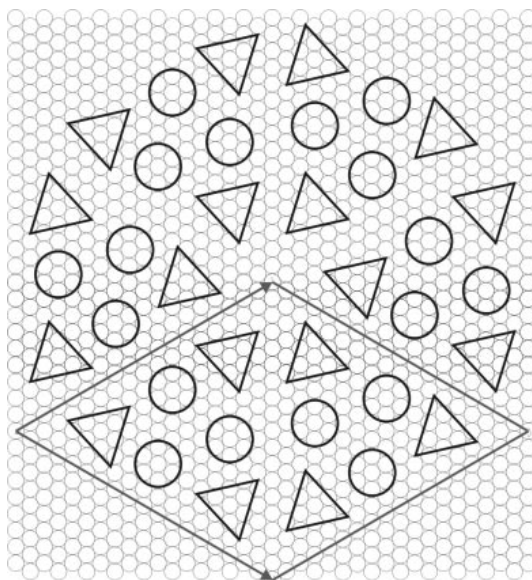


Figure 3.13.: Proposed model for the registry of the *star* phase on $Ag(111)$. The center hole is large enough to offer space for an additional molecule (see left arrow in figure 3.10).

3.4.2. 2D Molecular Gas-Phase

Between two SIMPs, often a 2D molecular gas-phase is found. In STM images, this can be recognized as streaks in the fast horizontal scan-direction, see top of figure 3.14. The line-scan, see bottom of figure 3.14, makes clear that the same single-molecular events can be found in the condensed phases and in the gas phase: the objects consistently have an apparent height of 0.5-0.6 nm and a width of 1-2 nm and can be identified as molecules. For a more detailed analysis of this so-called *lattice-gas* see [75]. The composition of the gas is not clear a priori, but could be explored by a variable temperature STM (e.g. freezing the movement or growing of a certain domain) or by a careful series of deposition experiments with one dominating component.

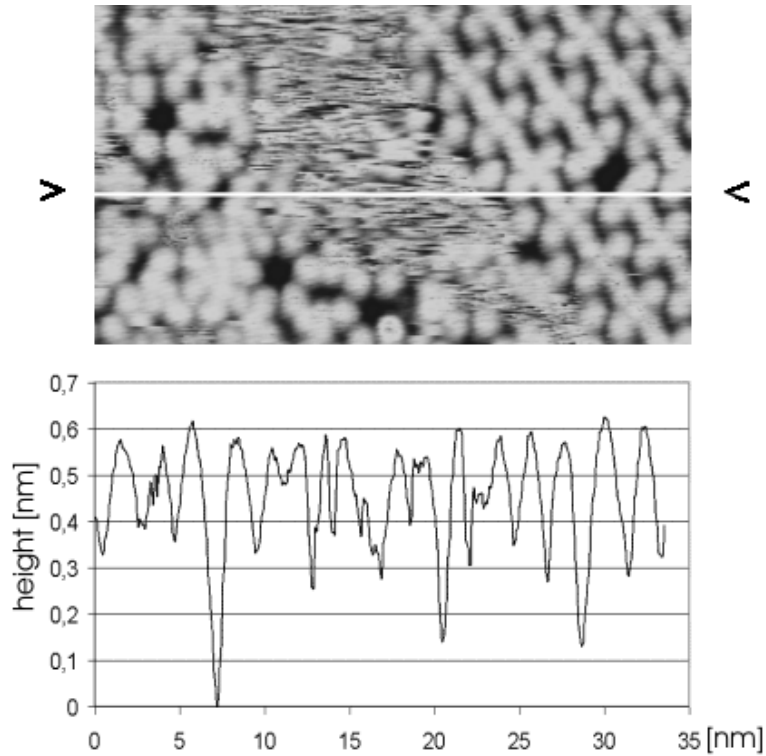


Figure 3.14.: Molecular gas-phase: between the two well-ordered SIMPs, random tip excursions can be seen due to mobile molecules (top part). Scan range 27 nm x 15 nm, $V_{bias} = 1.9$ V, $I_t = 20$ pA (section from fig. 3.10). The line-scan (“height-profile”, lower part) makes clear that the same objects can be found in the condensed phases and in the gas phase. The motion of the molecules in the gas-phase during the scanning-process, however, inhibits any correlation of the successive scan-lines.

3. Self-Assembly of Phthalocyanines and C_{60} on Ag(111)

Phase	Super-structure	Matrix	Unit-cell [\AA^2]	Ref.
Ag(111)	$1 \times 1 - (1\text{Ag})$	$\begin{pmatrix} 1 & 0 \\ 0 & 1 \end{pmatrix}$	7.233	Fig. 3.7
C_{60}	$(2\sqrt{3} \times 2\sqrt{3})R\pm 30^\circ - (1C_{60})$	$\begin{pmatrix} 2 & 2 \\ -2 & 4 \end{pmatrix}$	86.8	Fig. 3.7
SubPc	$(\sqrt{111} \times \sqrt{111})R\pm 4.71^\circ - (2\text{SubPc})$	$\begin{pmatrix} 10 & 1 \\ -1 & 11 \end{pmatrix}$	810.0	[33]
<i>star</i>	$(18 \times 18)R0^\circ - 2(3\text{SubPc} + 3C_{60})$	$\begin{pmatrix} 18 & 0 \\ 0 & 18 \end{pmatrix}$	2343.5	Fig. 3.13
<i>stripe</i>	$(\sqrt{108} \times \sqrt{151})R30^\circ - (2\text{SubPc} + 3C_{60})$	$\begin{pmatrix} 6 & 6 \\ -9 & 14 \end{pmatrix}$	998.1	Fig. 3.7

Table 3.2.: Crystallographic properties of various phases.

3.5. Schematic Room-Temperature Binary Phase Diagram

The multi-phase behavior of this binary system on Ag(111) has been studied as a function of composition in a series of deposition experiments. The results are summarized in the schematic “phase-diagram” (figure 3.15). From the top to the bottom, self-intermixed monolayers are shown with an decreasing SubPc: C_{60} mixing ratio from 1:0 to 0:1. In the first column, pure mono-molecular phases of SubPc and C_{60} are depicted at the top and the bottom. Homogeneous *star* and *stripe* SIMPs correspond to a mixing ratio of SubPc: C_{60} = 1:1 and 2:3, respectively, and are shown in the middle of the left column. Between these mixing ratios, coexistence of two adjacent phases is observed, as shown in the second column. Using this schematic 2D “phase-diagram”, a mixing ratio for deposition of the molecular components can be chosen to control the formation of selected 2D patterns [123].

Coadsorbate-induced ordering is a cooperative interaction between two different adsorbates which yields different ordered structures than either adsorbate forms by itself. The crystallographic properties of all superstructures from figure 3.15 are listed in table 3.2.

Intermixing Activity

The exact transition from one pattern to another upon additional deposition of molecules remains unsearchable, mainly because of technical reasons. The molecules are deposited in the OMBE chamber, whereas the observations are made in the STM-chamber, see figure 2.1. It is impossible to find the same surface location within nanometer precision and to control the mutation of the pattern after a sample-transfer of several meters. But there is a solution to get some aspects of the transition from one pattern to another sometimes. By preparing a sample with pure SubPc honey-comb pattern and then depositing a small amount of C_{60} , I can get some “snapshots” of the transition process.⁵ The C_{60} molecules inter-diffuse

⁵Because of slightly inhomogeneous deposition, there exist areas with a tiny amount of C_{60} . Other areas with higher density do not contribute to the process, presumably because the step-potential prevents inter-step diffusion and the molecules cannot cross steps of the substrate [75, 124].

3.5. Schematic Room-Temperature Binary Phase Diagram

and form “channels”, where two C_{60} molecules replace one SubPc molecule. Note that the SubPc domain of both sides of the “channel” are phase-shifted and the C_{60} molecules start to form a stripe similar to the known geometry (here, however, two C_{60} molecules are sandwiched between two staggered SubPc molecules). The chirality of this new single stripe

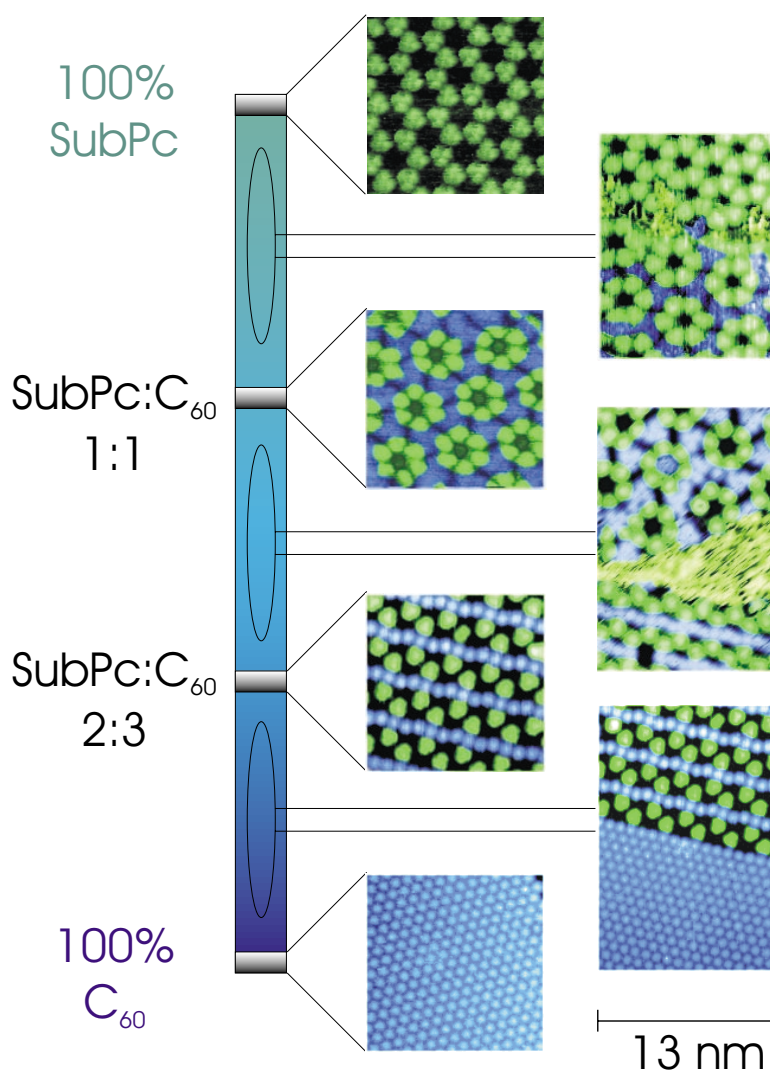


Figure 3.15.: Schematic room-temperature “phase-diagram” of SubPc and C_{60} with corresponding STM images of self-intermixed monolayers (imaged area, 13 nm x 13 nm, $1.0 \text{ V} < V_{bias} < 1.9 \text{ V}$, $20 \text{ pA} < I_t < 100 \text{ pA}$, C_{60} blue, SubPc green). Left column: pure SIMPs displayed against the ratio SubPc: C_{60} : 1:0, honeycomb phase of pure SubPc; 1:1, self-intermixed monolayer *star* phase; 2:3, self-intermixed monolayer *stripe* phase; 0:1, hexagonal phase of pure C_{60} . Right column: Coexisting phases in equilibrium with molecular 2D gas for ratios SubPc: C_{60} which are between the above-mentioned values.

3. Self-Assembly of Phthalocyanines and C_{60} on $Ag(111)$

(see section 3.3.2) is most probably given by the chirality of the preexisting honeycomb pattern.⁶

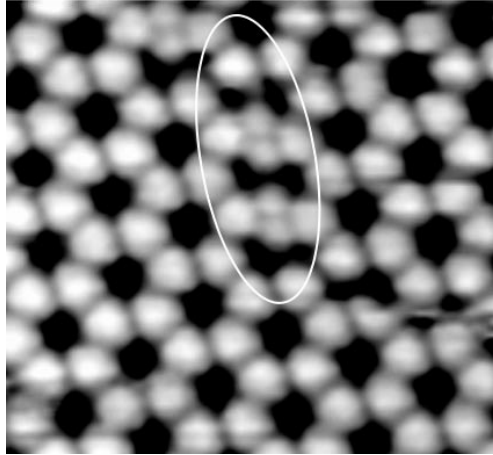


Figure 3.16.: “Snapshot” of the transition from pure SubPc honey-comb pattern to an intermixed phase. The C_{60} molecules inter-diffuse and form “channels”, where two C_{60} molecules replace one SubPc. Scan range 19 nm x 17 nm. $V_{bias} = 2$ V, $I_t = 15$ pA. This STM image is slightly filtered with a median filter.

⁶The honeycomb pattern can exist in two chiral domains [33].

4. Intermixing Mechanism

In order to understand this remarkable self-assembly behavior, possible molecule-molecule and molecule-substrate interactions have to be considered. These interactions and the molecular mobility determine nucleation, growth and ordering of molecular adsorbates. Upon deposition, these processes drive the system towards a minimum of the overall free energy. I think that the mechanism is based on a delicate balance of electrostatic and Van der Waals interactions. The most important underlying interactions and the relevant properties of the molecules [125] are discussed qualitatively in section 4.1. Further observations that explain the molecular interactions are given in section 4.2. A general consideration of thermodynamics of mixtures is treated in section 4.3. This chapter then is closed with a counter-example of the SIMPs: A bi-molecular system that does not intermix but that segregates into separate single-component phases is introduced in section 4.4.

4.1. A Delicate Balance of Electrostatic and Van der Waals Interactions

Neither SubPc nor C₆₀ form strong covalent bonds with the Ag(111) substrate, whereas it has for instance been observed for either molecule on Si(111) [62, 116]. Nevertheless, both molecules bind rather strongly to Ag(111): the C₆₀ monolayer desorbs only above 670 K [126, 127], whereas I have indications that the SubPc molecules decompose above 470 K. At room temperature, however, isolated molecules of both types diffuse and cannot be imaged by STM. This indicates that the corrugation of the molecule-substrate interactions is weak. In the following two paragraphs, the electronic properties and bonding of each component, C₆₀ and SubPc, are discussed first, and then the interactions governing the observed ordering in the SIMPs.

The first component, C₆₀, has a high polarizability, because its frontier π -orbitals extend around the carbon cage, see e.g. figure 4.1. Significant attractive Van der Waals interactions originate from mutually induced polarization fluctuation on the molecules [126, 128] and on the metal surface. An additional weak chemical bond to the Ag(111) substrate with ionic character arises from the charge transfer of approximately Δq of 0.8 electron from the metallic substrate to each C₆₀ in the monolayer, estimated from photoemission spectra, see figure 4.13, and vibrational energy shifts [129]. This charge transfer implies an induced dipole moment pointing towards the substrate which in principle leads to a long-ranged, lateral repulsion between these parallel dipoles. The packing and aggregation of the C₆₀ ad-layer is determined by the balance between the Van der Waals attraction, the dipolar repulsion and the “steric” (Pauli) repulsion between contacting molecules and the substrate.¹ The close

4. Intermixing Mechanism

match between intermolecular distances in the monolayer and in the fcc crystal of bulk C_{60} (with space group $Fm\bar{3}m$) [126] suggests that the long-range electrostatic repulsion between the adsorption-induced dipoles is of minor influence.

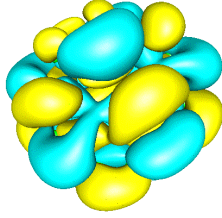


Figure 4.1.: LUMO of C_{60} [132].

For the second component, SubPc, AM1 semi-empirical calculations as well as ab-initio density functional calculations were performed using the B3LYP exchange-correlation functional at the 6-31Gd level [61] complementing earlier work [62, 63]. Both approaches indicate an excess of electronic charge on the electronegative atoms which surround the electron-deficient boron. This charge is compensated by an electron deficit which is mainly localized on the six central carbon atoms (figure 4.2).

This results in a calculated permanent axial dipole moment of $0.95 \text{ e}\text{\AA}$ pointing away from the Cl, the magnitude of which compares well to a measured value of $1.1 \text{ e}\text{\AA}$ and to the value of $1.2 \text{ e}\text{\AA}$ predicted by AM1 calculations [63], see figure 4.3. Each SubPc molecule is bound to the substrate by a Cl–Ag interaction and by electrostatic attraction of its polar charge distribution with the induced counter-polarization of the metallic substrate. On the basis of XPS and UPS data [33, 124] it is concluded that the SubPc is adsorbed intact with the Cl pointing towards the substrate. This is further confirmed by the observed destabilization of ordered 2D islands in STM images at reverse bias voltage V_{bias} where the dipole moment is opposing the electric field in the tunneling junction. The permanent dipole moment of SubPc together with its parallel image in the metallic substrate gives rise to a noticeable repulsive lateral interaction between the SubPc molecules [75]. On the other hand, SubPc is less polarizable than C_{60} , owing to its less extended frontier π -orbital, which are mainly localized around the central C–N–C-ring [62]. Therefore, the Van der Waals attraction between adsorbed SubPc molecules is weaker. This picture is supported by the tendency of SubPc to form ordered structures with voids and with intermolecular separations [75] of 1.79 nm which exceed the lateral extent of the molecule. The relative angular orientation of neighboring adsorbed SubPc molecules is determined by the details of the charge distribution: the dominant isotropic part of the electrostatic repulsion is reduced if the overall positive corner of one molecule points towards the face of its neighbor which exposes a negative charge around an N atom (see figure 4.2). Thus, for SubPc layers, unlike for C_{60} , a balance

¹Because of a small charge deficiency between the single bonds and a charge excess on the double bonds, the intermolecular potential in addition contains a small bond-to-bond Coulomb energy dependent on the molecule orientation [130]. This results in a variation of the domain energy by about 0.1 eV per molecule [131].

4.1. A Delicate Balance of Electrostatic and Van der Waals Interactions

between stronger electrostatic repulsion and weaker intermolecular attractions determines layer packing and ordering.

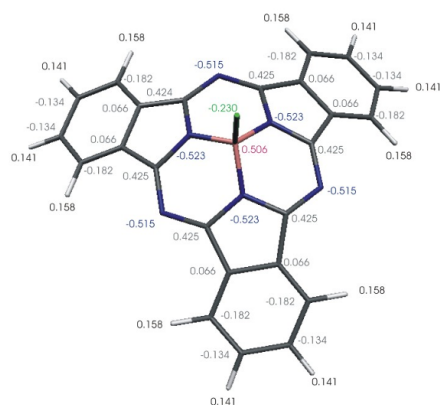


Figure 4.2.: Relaxed geometry and effective atomic charges (Mulliken population analysis) from a density functional computation on a single free SubPc molecule [125]. For the identification of atomic species, the color-code of figure 3.1 is used. The distribution of delocalized electronic states and partial charges determines the intermolecular and molecule-substrate interactions which presumably leads to the observed ordering as discussed in the text.

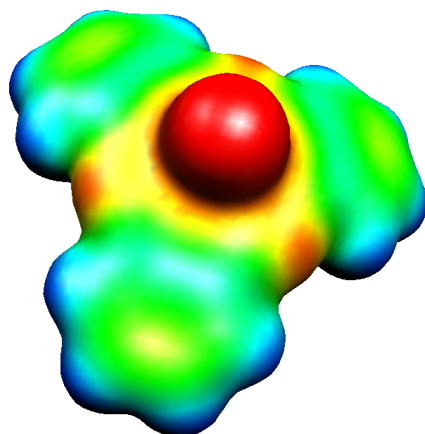


Figure 4.3.: Electrostatic potential of the free SubPc molecule mapped onto the electron density surface [60]. Excess of electrons at the Cl in the center are colored *red* (negative electrostatic potential), more positively charged portion at the peripheral phenyl-rings *blue* (positive potential). This electron distribution is responsible for the axial dipole moment [60] and for the molecular interactions.

4. Intermixing Mechanism

For the mixed phases, I note that the packing density of SubPc molecules in the *stripe* and *star* phases is about 7% and 20% higher than in the honeycomb phase of pure SubPc even if the same area is assigned to each C_{60} as in the pure hexagonal phase.² In analogy with ordered structures of small co-adsorbed molecules [89–91], this suggests a higher binding energy. In the case of benzene co-adsorbed with CO or NO, where also different phases were observed [89–92], this has been attributed to increased attraction between *antiparallel* induced dipole moments which originate from the adsorption chemistry of the two species. In our case, stronger binding also partly arises from the interactions of the SubPc permanent dipole moment with the *antiparallel* induced dipole moment of the neighboring C_{60} molecules. In addition, Van der Waals and anisotropic Coulomb interactions contribute. A summary of all the contribution is given in figure 4.4. But at the moment, it is not possible to deconvolute the individual contributions unambiguously. The proposed explanations are not final and a more detailed theoretical analysis is certainly desirable (e.g. numerical calculations including the substrate and/or several adsorbates). In particular the adsorption characteristics of the SubPc molecules, their mobility and appearance in STM images, as well as the detailed geometries, registries and relative energies of the observed ordered phases must still be quantitatively understood.

4.2. Discussion of Other Intermixing Models

There are many factors to consider when discussing this complex system. Unfortunately, even in works on simpler atomic systems [133], no conclusive rules could be derived about long-range electrostatic or local direct-interactions. The net effect in the redistribution of charge upon adsorption (and the modification of bonds) is very complicated and has to be recalculated in every single case. Further models can be proposed to explain the intermixing phenomenon as explained in section 4.1:

- Long-range interactions mediated by substrate surface states: On Ag(111), the corresponding wavelength of Friedel oscillations outranges the characteristic intermolecular spacing and strong surface-state – adsorbate coupling is ruled out, see section 4.2.1.
- Intrinsic dipole-dipole interaction: They are too weak, see section 4.2.2.
- Charge transfer *between* the molecules: Possible effect, could explain the intermolecular attraction, discussion in section 4.2.3.
- New chemical bonds between the components: UPS and XPS measurements (see section 4.2.4) show no chemical interaction between the components, but solely an inter-diffusion. The interface between the two components proves to be stable at room-temperature (STM).

²This results easily from following consideration (for numbers see table 3.2): One C_{60} molecule in the single component phase needs 87 \AA^2 , one SubPc molecule in the pure honeycomb pattern needs 405 \AA^2 . In separate phases, these two molecules thus need 492 \AA^2 . In the *star* phase, however, 1 SubPc + 1 C_{60} only need 391 \AA^2 . In the *stripe* phase, 2 SubPc + 3 C_{60} need 998 \AA^2 , whereas the same molecules in single-component phases need 1071 \AA^2 . This defines the higher packing density of 7% and 20%.

4.2.1. Long-Range Interactions Mediated by Substrate Surface States

Theoretical calculations on adsorbed atoms and molecules have shown that the interactions between adsorbates are primarily indirect (i.e., via the substrate wavefunctions) when the species are separated so that the overlap of adsorbate orbitals are negligible [95]. The substrate wavefunctions oscillate in sign as a function of the separation distance, and decrease (with r^{-2}) in magnitude with increasing separation distance [134]. When these interactions are found to be attractive at certain separation distances, ordered domains can form [135]. The possibility of such long-range interactions mediated by substrate surface states [136], however, can in my opinion be excluded because on Ag(111) the corresponding energy band edge is only 0.05 eV below the Fermi level [137], and the corresponding wavelength of Friedel

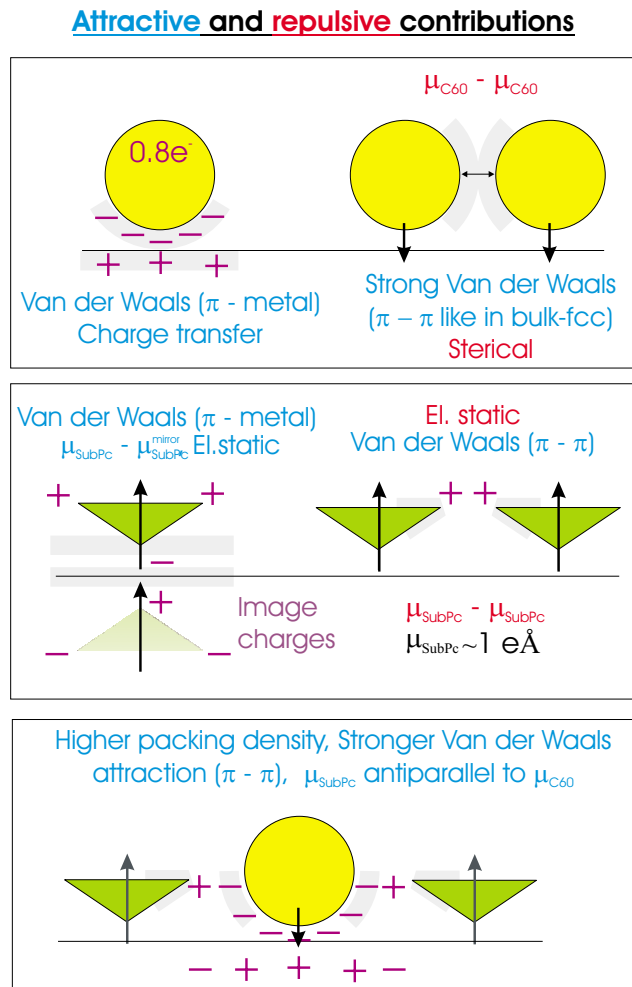


Figure 4.4.: Summary of the forces in SIMPs: molecule-substrate and molecule-molecule interactions for both components separately and the mixed phase are shown. Attractive contributions are in *blue*, repulsive contributions in *red*.

4. Intermixing Mechanism

oscillations ($\lambda = 3.8$ nm) considerably exceeds any of the observed nearest-neighbor spacing, see figure 3.7. Other anisotropic adsorbate systems show such a coupling [137, 138].

4.2.2. Intrinsic Dipole-Dipole Interaction

A calculation of the (permanent) dipole – (substrate induced) dipole interaction between SubPc and C₆₀ gives an attractive value of +8.3 meV for the antiparallel dipole moments [139].³ At room-temperature, this is not enough to explain the SubPc–C₆₀ attraction. From the change in work-function, the dipolar interaction energy for example of the pairing CO+benzene on Rh(111) was estimated to be +90 meV [89]. In their study, this was enough to stabilize these chemisorbed molecules in an intermixed phase.

4.2.3. Intermolecular Charge Transfer: Apparent Height Analysis

Previous observed intermixed systems [81, 88–95, 97] are based on a typical electrophilic and electrophobic molecular pairing with a charge transfer between the molecules. The leading forces for stabilization in these donator–acceptor systems are then believed to be dipole–dipole interactions (induced antiparallel dipole moments, see previous section).

The analysis of the apparent height of the C₆₀ and SubPc molecules gives some indications of a charge transfer from the 14- π -electron system of the SubPc to the π^* -orbital of the C₆₀, which is well known as a strong electron acceptor. This supports the observed moderation and stability of the mixed monolayers at the presence of two adsorbates. However, other observations (section 4.2.4) do not support this charge transfer mechanism.

Since STM images represent a convolution of the electronic (LDOS) and topographic structure, a change in the apparent height can thus be due to a change in the physical height of the molecule, a change in the conductance of the molecule or both, see equation (2.4). If the geometry of the system is known, information of the electronic situation can be deduced and a charge transfer might become detectable.

To investigate this proposed intermixing mechanism, height-profiles of STM images have been accurately analyzed. Images with coexisting phases and identical scanning parameters have been chosen to compare the apparent molecular heights. By investigating all phases, the apparent height of the C₆₀ in all configurations was found, see figure 4.5.

An electron transfer from the SubPc to the C₆₀ should lead to a reduction of the C₆₀ height in STM images of mixed phases since electrons would be transferred from the SubPc HOMO to the threefold degenerated C₆₀ LUMO orbitals. The additional filling of the LUMO would then reduce the tunneling probability (compared to the already 0.8 substrate-electron filled C₆₀ LUMO in the pure fullerene layer). In STM images (with negative bias, tunneling into the LUMO, see figure 2.4), the C₆₀ molecules would then be observed with a smaller signal. Moreover, additional SubPc neighbors should enhance the effect.

³Interaction energy $w(r) = \frac{u_1 u_2}{4\pi\epsilon_0 r^3}$. Supposed a permanent dipole moment for SubPc of 0.95 eÅ and a C₆₀ charge transfer of 0.75 e from the Ag(111)-substrate over a distance of 0.2 nm and an inter-molecular separation-distance of 4 lattice constants (see figure 3.7). This calculation does *not* include a charge transfer *between* the molecules which would intensify the dipolar interactions.

4.2. Discussion of Other Intermixing Models

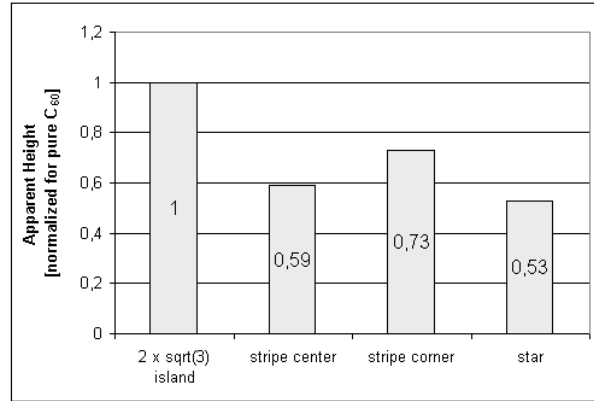


Figure 4.5.: Apparent height of C₆₀ molecules in different phases, imaged at 1.9 V bias voltage V_{bias} . The variations are assumed to arise from different local environments modified by the SubPc molecules.

Indeed, the measurements show such a decrease of the C₆₀-height as a function of the number of “donating” SubPc neighbors. The pure C₆₀ layer without any SubPc contact and no potential charge transfer shows the highest apparent height. Also the behavior of the C₆₀^{stripe-center}, C₆₀^{stripe-corner} and the C₆₀^{star} molecules support the charge transfer theory from the SubPc to the C₆₀. The C₆₀^{stripe-corner} molecule is the largest of these three cases, which in this model is explained by the absence of any SubPc contact. The higher coordinated C₆₀^{stripe-center} and C₆₀^{star} molecules are smaller than the low coordinated C₆₀^{stripe-corner} molecule which can be explained by the direct contact to SubPc neighbors. The small height-difference between the C₆₀^{stripe-center} and C₆₀^{star} molecules can be interpreted in the same arguments of charge transfer: Since the C₆₀:SubPc mixing ratio is 3:2 in the *stripe* pattern and 1:1 in the *star* pattern, the C₆₀ in the latter pattern appears smaller because it is supplied with the charge from one SubPc, in the *stripe* pattern only from $\frac{2}{3}$ of a SubPc. In conclusion, this analysis supports the SubPc→C₆₀ charge transfer theory.

There could be additional effects to explain the differences of the apparent heights, like the adsorption on different sites on the Ag(111) substrate [114] (see figure 3.13 and 3.7), random blinking⁴ [112] and substrate- or coadsorbate-induced conformational changes⁵ [140]. Up to this point, I discussed the apparent height of the fullerenes at a certain bias voltage and I showed that this effect could be linked to a possible charge transfer between the molecules. The situation gets more complex when looking at different bias voltages.

Bias-dependent Images During imaging with the STM, the bias voltage V_{bias} can be varied. Only one polarity was applied (sample positive), because the SubPc islands are known to be stable only in this field orientation due to the molecules’ dipole moment [33], see also section 4.1. Depending on the applied bias voltage, the SubPc or the C₆₀ molecules

⁴For an example see also section 4.4.

⁵For an example see also appendix A.

4. Intermixing Mechanism

appear more pronounced. At low voltage (e.g. 0.5 V), only the fullerenes can be imaged, see figure 4.6. This is consistent with observations on pure SubPc films [33]. That the C₆₀ molecules can be observed also at lower voltage is a hint for a metallic coupling induced by charge transfer from the Ag substrate, as already discussed in section 4.1 and further treated in different contexts in section 4.2.3. A detailed analysis of various STM images, recorded with the same tunneling current of 20 pA, shows that the apparent heights of both molecules becomes similar only at elevated bias voltage, see figure 4.7. The functional relation looks reasonable, but is not straightforward, since the appearance in STM is governed by the electronic structure of the adsorbed components. We are tunneling from the tip into the LUMOs. The electronic structure of free SubPc is known from computations [60], that of C₆₀ also from inverse PES experiments [141]. The two DOS show more details like the three peaks of C₆₀ (at 0.4, 1.5 and 2.8 eV [60]) or two peaks in the case of SubPc (at 0.6 and 2.26 eV [141]) and therefore should lead to a more complex behavior than the measurements and the fitted curve of figure 4.7. More data is required to fully understand the observed bias dependence and to correlate it to theoretical explanations. At this step I just state that the appearance of the *stripe* pattern strongly depends on the applied bias voltage.

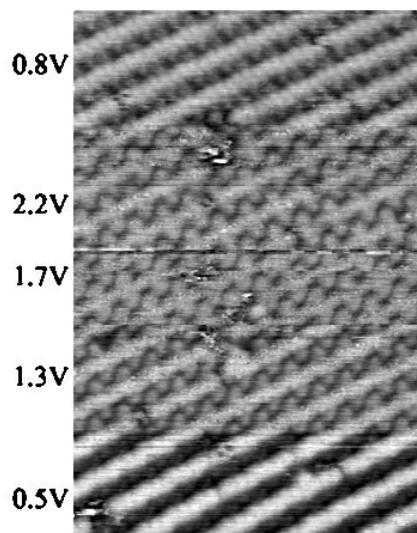


Figure 4.6.: STM image of a *stripe* island recorded at the different bias voltage V_{bias} , indicated on the left side. The tunneling current I_t was kept constant at 20 pA. At low V_{bias} , only the C₆₀ molecules remain visible. Due to the specific electronic structure of the molecules, the appearance of the pattern strongly depend on V_{bias} . Scan range 34 nm x 51 nm.

4.2.4. Formation of a New Chemical Complex

In the next few sections, I will show that the SubPc and C₆₀ molecules in the intermixed phases do *not* form a new chemical compound. The hypothesis was that the SubPc and

4.2. Discussion of Other Intermixing Models

the C_{60} molecules form building blocks of a new quantum state, e.g. a SubPc- C_{60} -SubPc complex in the *stripe* pattern. But potential associated molecule-molecule interactions and their changes in the electronic states are not seen in PES experiments or are too weak to be detected with our system. The photoelectron spectroscopy method is used to characterize the valence band and the C1s core level of the molecules in different combinations, as well as to determine the coverage of the molecular films.

Coverage determination: The coverage of the molecules was determined by comparing the C1s peak with the $Ag3d_{3/2}3d_{5/2}$ double peak area [54], taking the adsorption geometry into account. Thereby, 1 ML of C_{60} means that the substrate is covered with 1 layer of fullerenes in the $2\sqrt{3} \times 2\sqrt{3}$ arrangement. 1 ML of SubPc stands for a complete layer of SubPc molecules in the honey-comb pattern. The obtained coverage for C_{60} or for SubPc is proportional to the thickness obtained with the microbalance, as can be seen in figure 4.8. This is in no way surprising, but demonstrates that the molecules are confined to the 2D substrate surface and that they do not desorb after the deposition.

Furthermore, the value of the C1s-area on a SIMP sample is simply the sum of the C_{60} and SubPc signals, as they correlate perfectly with the sum of the microbalance values. Either molecule does not affect the other component and the first component (SubPc) remains at the surface even after the co-deposition of the second component (which finally is a weak form of “sputtering”). The deposition process therefore is *additive*, relating to section 4.3. In addition, these linear relations in figure 4.8 show that all measurements were done in the submonolayer range where no 2^{nd} layer effects yet take place. Weaker bonded molecules of a second layer would influence the XPS signal [142] and lead to a kink in figure 4.8.

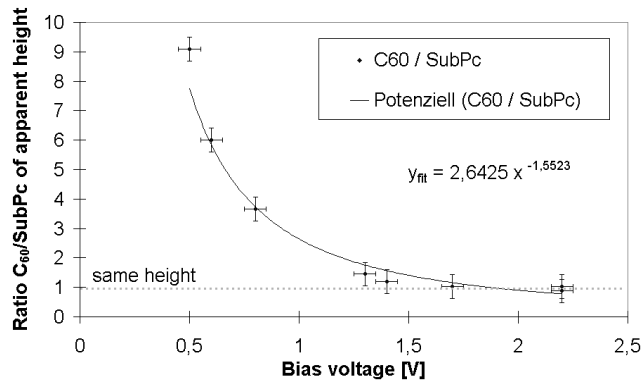


Figure 4.7.: The ratio of the apparent heights of C_{60} and SubPc is shown as a function of the applied bias voltage V_{bias} . The tunneling current I_t was kept constant at 20 pA. At elevated V_{bias} , the apparent heights of both molecules becomes the same, whereas at lower bias voltage, the C_{60} dominate because their LUMO is partly occupied owing to a charge transfer from the substrate. The SubPc molecules are hardly visible at low V_{bias} , which is consistent with observations on pure SubPc films [33].

4. Intermixing Mechanism

The absolute thickness calculation in units of monolayers is tricky because it uses some geometric factors describing the expected patterns. This can lead to large errors. However, a comparison to other UPS spectra [143] shows an excellent agreement.

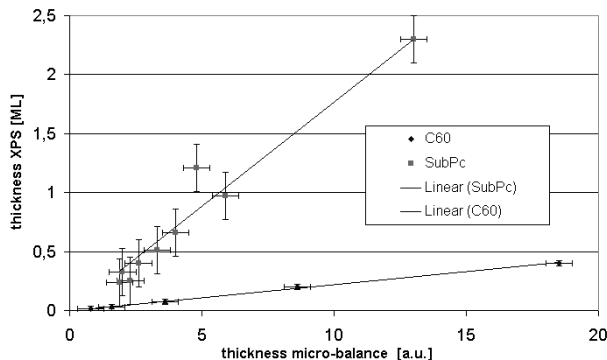


Figure 4.8.: Comparison of the coverage measurement by the microbalance and by XPS. Both methods correlate well.

C1s peak shows no new chemical component: XPS measurements were first performed on pure C_{60} thin films ($\theta < 1$ ML). In the measured XPS spectrum (at the top of figure 4.10), only one single $C1s$ peak at 284.9 eV relative to the Fermi level, could be resolved, corresponding to the interpretation that all carbon atoms of C_{60} are equivalent. However, the overall line shape is slightly asymmetric, with a well-pronounced tail extending to the high-binding-energy side, as also was seen on other metals [144]. This indicates that fullerene adsorption leads to a metallic interlayer and breaks the molecular symmetry, thus promoting a variety of inequivalent C sites [144].⁶ Studies done on thick films, in contrast, show a symmetric $C1s$ peak [145]. A characteristic shift of the $C1s$ peak as a function of the coverage is seen in figure 4.9. At a coverage of 0.4 ML, the shift is $\Delta = 0.35$ eV. This shift can be explained by a reduced image screening for molecules in the the thickest films [142, 146]. A controversial study [128] assigns this core level shift to a charge transfer because Scanning Tunneling Spectroscopy (STS) experiments⁷ show the same shift as Photoelectron Spectroscopy experiments.

All these results are in good agreement with other fullerene studies. When comparing C_{60} spectra to intermixed spectra, it is important that the coverage is considered because of its influence to the $C1s$ peak position.

In addition, XPS measurements were done on pure SubPc and two-component films (spectra see figure 4.10). The $C1s$ signal of the different films was analyzed. The chemical environment of the carbon atoms in C_{60} and SubPc is different: the 60 carbon atoms of the

⁶Bulk fullerenes show a symmetric $C1s$ peak because all C atoms are sitting in perfectly equivalent sites with each C atom being coordinated to two partner atoms through a double bond (hexagon side) and to the remaining C atom through a single bond (pentagon side), see section 3.2.

⁷without the ability of photoelectron screening

fullerene are all bound to three carbon neighbors via two single bonds and one double bond (see figure 3.1). The 24 carbon atoms in the SubPc molecules are bonded in the following three configurations (see figure 3.1): 6 of them are connected to three carbon atoms, 12 of them to two carbon neighbors and a hydrogen atom and 6 of them to two nitrogen and one carbon atom.

The SubPc C1s spectra therefore show two peaks (see figure 4.10): at 285.1 ± 0.1 eV (C–C compound type) and at 286.75 ± 0.1 eV (C–N compound type), in accordance to [148]. The spectra of the C₆₀ phase and the mixed layer (same figure) shown only one maximum at 284.9 ± 0.1 eV, respectively at 284.75 ± 0.1 eV (C–C compound type). In both C₆₀ and mixed layer spectra, the peaks are slightly asymmetric with a tail extending to the high-binding-energy side. In the case of the pure fullerene this is attributed to the metallic interlayer (see above). In the mixed films, the asymmetric tail also covers the smaller C–N peak. Here, both types of molecules, each with different carbon environments, contribute to the measurement. It can be seen that all C–C peaks are at the same position within 0.15 eV.⁸ Thus, the carbon compound C1s peak in the mixed phase shows no drastic shift upon co-deposition. From these observations it can be deduced that the carbon atoms of the SubPc and the C₆₀ molecules in the mixed phases still are in their original environment and the molecules are chemically not modified.

Valence band measurements show no new chemical component: Also in the UPS measurements, one can see that both molecules remain intact, just laying side-by-side, as is guessed from the STM images and XPS measurements. No new chemical compounds are believed to be formed.

Both SubPc and C₆₀ films show up with their characteristic UPS spectra [33] (see figure 4.11). The UPS profile of the clean Ag(111) surface is dominated by the Ag4*d* states spanning the 13-16 eV K.E. range (not shown here), while the featureless plateau located

⁸This residual shift probably arises from the coverage dependence of the individual peaks.

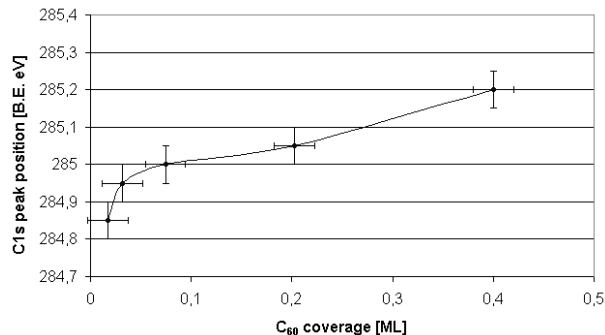


Figure 4.9.: The C1s peak of the C₆₀ film shifts as a function of the coverage. The chemical shift, compared to bulk fullerenes, where the C1s peak shows up at 285.3 eV, points toward an ionic character of the adlayer–substrate interaction [113, 147].

4. Intermixing Mechanism

at higher K.E's up to the Fermi edge are primarily due to the delocalized Ag5*sp* states (see lowest curve). The small peak at 17 eV K.E. is attributed to a satellite of the *d*-bands by the He-I β radiation with $h\nu = 23.08 \text{ eV}$. The C₆₀ (HOMOs at ≈ 18 and $\approx 17.5 \text{ eV}$ K.E.) have a weak interaction with the low density Ag5*sp* states of the substrate [143], so that the C₆₀ molecular orbitals will retain their character [127]. The high density of states of the Ag *d*-band only start at higher binding energies. This advantage of Ag over other noble metals ensures a large energy window for the C₆₀ derived states close to the Fermi level free from interference by the *d*-band. In addition, the Ag(111) surface is known to be stable with regard to reconstruction upon adsorption.

The C₆₀ UPS spectrum is characterized by the manifold HOMO- and HOMO-*n* orbital related structures, in agreement with published results [147]. Figure 4.11 shows the region around the Fermi energy at different C₆₀ coverage. The features at lower K.E. (not shown here) are mixtures of π and σ orbitals [149]. The two peaks at ≈ 18 and $\approx 17.5 \text{ eV}$ K.E. stand for the HOMO and HOMO-1 and they are derived from π -states with an angular momentum *l* equaling 5 and 4, respectively [150]. The HOMOs of the C₆₀ are known to shift towards lower K.E. as a function of the coverage [147, 151]. When comparing to the mixed phase later, this shift has to be taken into account. The parallel shift of the HOMO and HOMO-1 as a function of the coverage is clearly visible, as summarized in figure 4.12. The simultaneous shifting is a clear sign for the ionic dominance of the Ag-C₆₀ interaction, a so-called “rigid-band shifting” without covalent character. This shifting of the spectra can be explained by *charge transfer* [128]. Theoretical calculation of C₆₀⁺ and C₆₀⁻ support the rigid shift [145]. Another study [142] explains this shifting of the spectra by *screening* due to

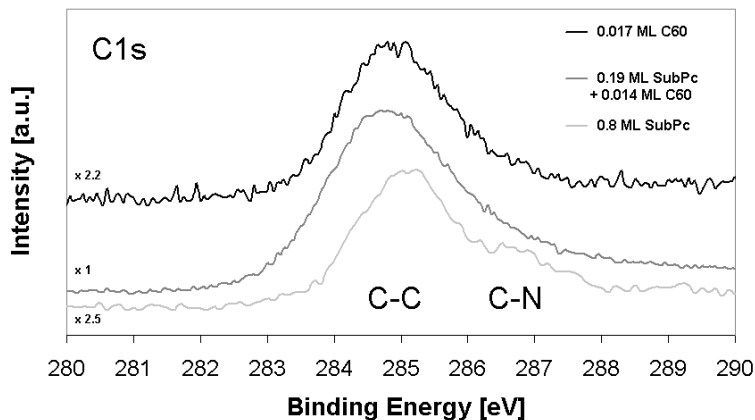


Figure 4.10.: XPS spectra of the C1*s* peak of pure C₆₀, pure SubPc and a two-component film on Ag(111) measured with Mg-K α excitation. A chemical shift can be observed for the C-C and C-N carbon compound peaks of the SubPc film. The two different chemical environments of the carbon atoms in SubPc also lead to the asymmetry in the main peak of the mixed film. In all phases, however, the C-C peak-position is unchanged.

the metallic first monolayer and the substrate. The valence band peaks at 13-16 eV kinetic energy related to the Ag(111) states are progressively reduced as C₆₀ is deposited on the surface (not shown here). The progressive formation of C₆₀ induced electronic levels can be observed. Spectra at sub-monolayer coverage are not affected by annealing to 500 K [143].

In pure Ag(111) samples, the Ag5*sp* background signal in the vicinity of the Fermi level is nearly zero. With small C₆₀ coverage, the film gets a metallic character as can be seen in the extra-emission at the Fermi level in figure 4.13, top curve [144, 147, 151]. This is consistent with the C1*s* results which also confirm the ionic character of the adlayer–substrate bond (see figure 4.9) and the analysis of the apparent heights (see section 4.2.3). The new states at E_F reflect the tail of the π^* -derived LUMO orbital which is completely unoccupied in solid C₆₀ and is sizeably shifted towards the Fermi level when the fullerene interacts with the Ag(111) substrate. This is clearly a strong confirmation of the ionic character of the C₆₀-substrate bond [112], the LUMO-derived extra-emission being the direct fingerprint of the charge transfer from the metal crystal towards the C₆₀ molecule. Integration of this peak yields a charge transfer of about 0.75 electrons per C₆₀ [127]⁹, consistent with vibrational energy shifts [129]. The term *metallic* here reflects the finite DOS at E_F as measured by STS or PES methods, but does not imperatively stand for a conductivity over large distances. For this purpose a lateral mobility of the charges is further required. The same formation of metallic-like interfacial states is also known from Perylenes (see 4.4.2) on Ag(111) [152].

The states at E_F effectively are new molecular states and not an artefact of the experimental method. It can be ruled out that the signal is a satellite (projection) of the C₆₀ HOMO by the He-I _{β} line (23.08 eV), although the positions offer this interpretation. From measurements on the pure Ag film I know that the He-I _{β} signal is only 3% of the He-I _{α} signal. The new states at E_F , however, form 45% of the LUMO. This is too intense to derive from the satellite line.

The SubPc spectra (see figure 4.13 and figure 4.14) shows characteristic features [33]: The HOMO is around 18.25 eV K.E., the same region where also the C₆₀-HOMO is located. Also the HOMO of the SubPc shifts to higher B.E. with increasing coverage, namely 0.4 eV from 0.4–8.4 ML, mainly attributed to charging effects of the molecular layer (more details can be found in [33]).

UPS measurements on two-component layers: We found that the valence spectra of SIMP films are identical to a simple linear combination of the C₆₀ and SubPc spectra, see figure 4.14. Thus neither a peak broadening nor a shift due to the intermixing process can be found.

In figure 4.14, three measured spectra (pure C₆₀, pure SubPc and two-component film) and one calculated linear-combination of two spectra are shown in the range close to E_F . The linear-combination of both single component films was fitted to reproduce the spectra of the mixed layer. This simulated spectra (weighted sum of the single-component spectra)¹⁰ and the measured spectra of the mixed film match perfectly. The intermixed spectra can be

⁹The threefold degenerated LUMO can maximally be filled with 6 electrons.

¹⁰The associated factors are not useful because the experimental settings are not absolute identical.

4. Intermixing Mechanism

interpreted as a simple superposition of features from both materials. No additional peaks and no broadening of the features close to E_F ¹¹ point towards a possible chemical reaction of both components. The system is *additive* in its electronic properties in regard to section 4.3. Therefore it is concluded that no strong hybridization of the electronic states takes place and no new chemical compound is created. A ground-state electron transfer between SubPc and C₆₀ is not observed or too weak to be detected and therefore is not believed to be the main intermixing reason. Note that in this linear-combination, the C₆₀ fraction has to match that in the intermixed phase because of the strong coverage dependence of the HOMO peaks

¹¹The π -derived features are most sensitive for a chemical bonding.

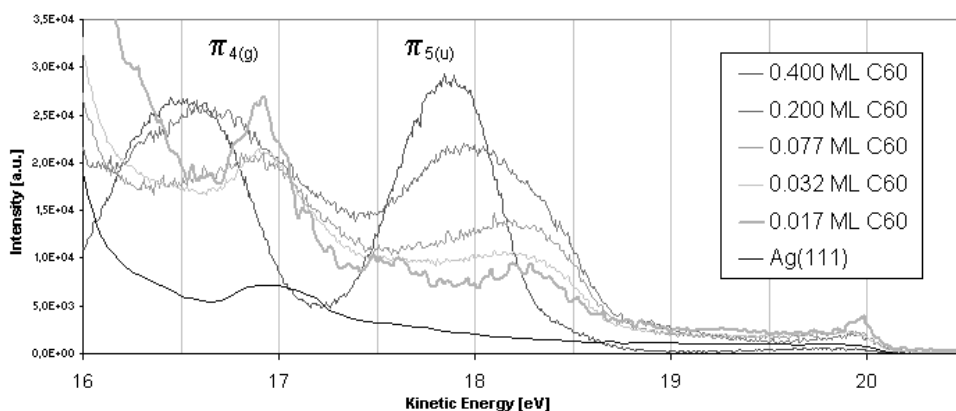


Figure 4.11.: He-I ($h\nu = 21.2\text{ eV}$) valence band spectra of various thickness' of C₆₀ layer on Ag(111). The characteristic HOMO and HOMO-1 peaks simultaneously shift towards smaller kinetic energies. The individual spectra are scaled by an arbitrary factor to stress the shifts.

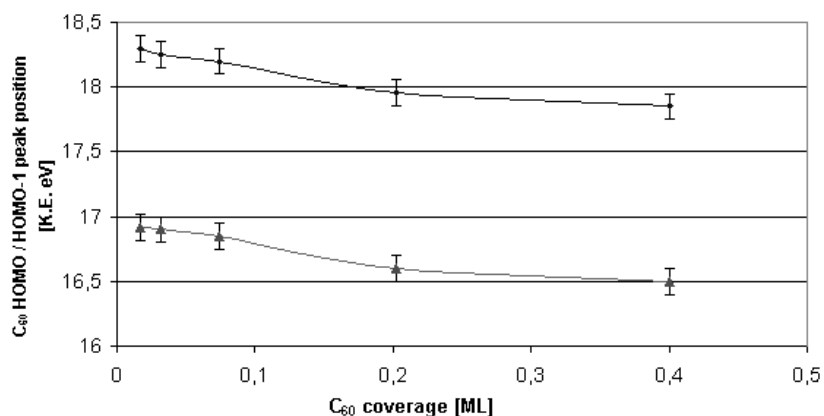


Figure 4.12.: Rigid band shift of the C₆₀ HOMOs with increasing film thickness indicate a charge transfer and screening.

4.2. Discussion of Other Intermixing Models

(figure 4.12). Secondary, the whole valence spectrum of the SIMP film can be described as a linear-combination of its components (not shown here), but below 16 eV K.E. the Ag features strongly dominate due to the low sub-monolayer coverage of molecules.

This additive behaviour is in contrast to other intermixed systems [89, 113] where the ground state electronic wave functions of two components actually do mix. For example Metal-Phthalocyanines (M-Pcs), combined with C_{60} in a study of novel photoreceptor material [113]. For $M=Ni, Cu, TiO$ or the metal-free H_2 -Phthalocyanine (Pc), all Pc derived features in the UPS spectrum shift on the binding energy scale (0.2-0.7 eV) towards the

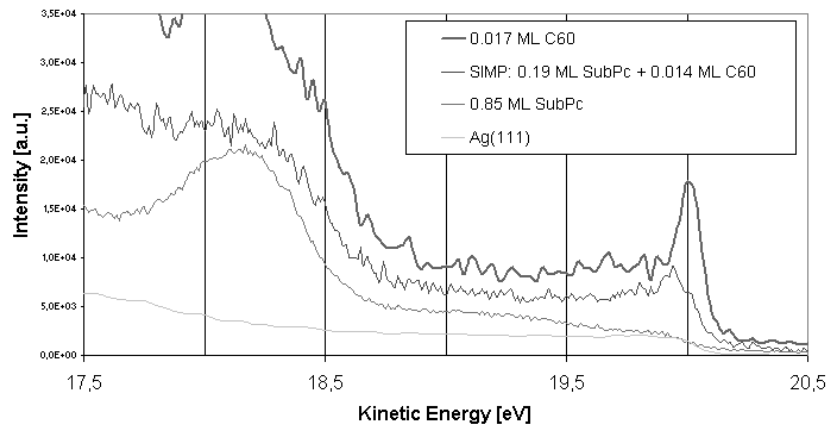


Figure 4.13.: UPS spectra close to E_F of different films. In contrast to the SubPc layer, the C_{60} and the two-component films show filled states at the Fermi edge.

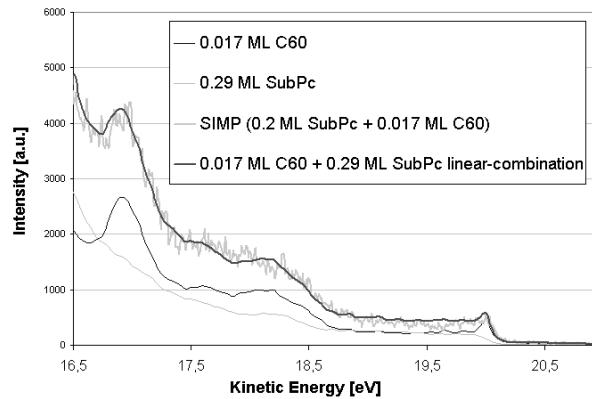


Figure 4.14.: Valence band spectra close to E_F of pure C_{60} , pure SubPc and a two-component film on Ag(111) with approximately the same amount of the components, together with a calculated linear-combination of the pure films. All features of the SIMP spectra simply can be explained by the pure films, thus no strong interactions between the two components are believed to take place.

4. Intermixing Mechanism

Fermi energy upon contact with C_{60} . This observation of a change of the surface-band bending demonstrates that it is not sufficient to measure the spectral feature of the single components separately. Only a measurement of the two components in contact with each other gives the true values for the energy differences between the valence-band onset of C_{60} and the different M-Pcs. That system is strongly *non-additive* in its electronic properties, referring to section 4.3.

The SIMP spectra (see figure 4.14 and 4.11) show a *metallic* characteristics like the pure C_{60} film at low coverage $\theta_{C_{60}}$. This is not mandatory linked to a SIMP property like “conducting nanowires” but could also derive from pure C_{60} phases, which form residual metallic $2\sqrt{3} \times 2\sqrt{3}$ islands.

Limitations: However, if there were new signals due to a chemical interaction, they are expected to be weak because of the relative small ordered SIMP domains within a large disordered gas-phase (ordered domains roughly estimated to 10%). The non-locality of the PES method leads to a fundamental restriction. In contrast to STM studies, large numbers of domains are statistically averaged. The handicap of small signals at thin films cannot be circumvented by using thick films, because the SIMP structures need close substrate contact and therefore are limited to 2D.¹² A second problem as a matter of principle is the similar HOMO peak positions in the valence bands of both components. And also a satellite from the He- I_β line unfortunately falls into this range. Measurable effects upon catalytic promotion are hardly detectable even in atomic systems with strong interactions and, moreover, are known to be even weaker in molecular systems [89].

4.3. Thermodynamics of Mixtures

The two kinds of molecules in the mixture are called *components*. If one component strongly predominates, then one speaks about a *solution*, otherwise of a *mixture*. In these kind of mixtures, new phenomena can emerge that don't exist in pure substances. Such two-component systems can contain aggregates of macromolecules, polymer-solutions, gels, soaps, liquid crystals, lipids, micelles, colloids and suspensions and are of major biological and technical importance [153]. The here observed phenomenon is known in 3D when two strongly unequal interactions between molecules leads to a demixing of a liquid phase [154]. Thereby, two or more liquid phases of different relative composition c and density ρ are formed and are in equilibrium with each other. This is known as *partial miscibility* of two liquids and as *mixing gap*, where the mixture is separated into two coexisting stable phases with different relative concentrations c (so-called demixing into conjugated solutions).

The properties of a multi-component system result from those of the components and of the effects which occur during the mixing process. The macroscopic behaviour of a multi-component system cannot be derived directly from the properties of the isolated components, but is determined also by the inter-molecular interactions. Generally, the physical interac-

¹²And up to now, it was not possible to image a SubPc double layer at room-temperature, not even at very low tunneling currents.

tion that appear between the particles of a system stem from the charge of free ions, from free or missing electron pairs or from permanent or induced displacement of charge which leads to a dipole effect and is found in many molecules. These physical interactions which affect the free mobility by the attraction or repulsion between the molecules and by the own volume of the particles, lead to changes of the properties of the mixed particles compared to the isolated ones. As a consequence, the external observed macroscopic properties are always a *sum* of the molecular properties of the isolated particles and the part which comes from the interactions. The properties of a multi-component system consist of contributions from the single components proportionally to their quantity. Only if the pure materials are assembled as macroscopic sub-systems, the properties of the pure components are *additive* [153]. Otherwise, a spontaneous mixing process takes place and change the properties of the system. These changes are only due to the mixing process; the temperature and the pressure can remain constant. These changes in *non-additive* systems are caused by a *dispersion of the molecules* and by *changes of the inter-molecular interactions*. The former reason is independent of the material and the system and is called *ideal part* of the modification. This is the case if we theoretical keep the inter-molecular interactions constant during the mixing process. The result then is an *ideal mixture*. The changes in the intermolecular interplay, however, leads to the *real effect* or *excess part*. It contains the material or system specific properties. As every real system develops additional interactions that depend on the temperature, pressure, composition and the kind of partners, it always shows more or less variations from the ideal behavior. The total required space for example results from the particle volume and the interspaces, that depend on the interaction of the specific mixture. These effects of dispersion of the particles and the changes of interaction after mixing can be as tremendous as a changing in the state of aggregation. As is well known, a change of the melting point of a certain material often is applied by mixing with a suitable component, e.g. the defrosting of ice by NaCl. In the case of the SIMPs, real effects concern e.g. the arrangement, the symmetry, the apparent height of the fullerenes in STM images and the surface density, as previously discussed.

If the molecules are distributed homogeneous over the whole system and the same interaction are dominating everywhere, a system is called *homogeneous*. On the other hand, several states of aggregation simultaneously can co-exist within a system. Such a system with a discontinuity in the molecular distribution and in its interactions are called *heterogeneous*. Individual homogeneous areas describe the *phases*, here in mixed systems *mixing – phases*, see figure 3.15. Different phases are separated by *phase boundary lines*, where the system properties change discretely. Thus *phases* are those parts of a heterogeneous system that have properties and composition different from other parts and are separated by interfaces. Furthermore, a phase is homogeneous, i.e. has identical physical and chemical properties in all locations. Under equilibrium condition, all phases in a phase-system are in equilibrium, also two that eventually are separated by a third phase. The equilibrium therefore is independent of the spatial arrangement of the phases [155]. A spatial separation of phases, however, may reduce the diffusion into the equilibrium. The phases in the schematic phase diagram (figure 3.15) agree with this thermodynamic definition, albeit they can be limited

4. Intermixing Mechanism

kinetically.

The miscibility generally is temperature-dependent. In certain temperature ranges, the components are not miscible in all concentrations. If two two-component phases co-exist, this state is the mixing gap. The mixing gap in liquid systems can have the forms shown in figure 4.15 (white areas). No states exist in the white areas, but two phases with the relative concentrations given by the boundary line (coexistence curve) coexist in equilibrium. In the dashed areas, a homogeneous phase of both components exists. The phase diagram of our SIMP system, so far only investigated at room-temperature, is believed to resemble case a) and c). 2D crystal structures are believed to exist only at certain temperatures: case c) for T being the temperature during deposition, case a) for T being the temperature of an already grown layer. Above the upper critical temperature, only a gas-phase containing both components (see section 3.4.2) is expected to exist. Cooling probably freezes the pattern and conserves it unchanged. A deposition below the lower critical temperature hinders the molecular diffusion and prevents a pattern formation.

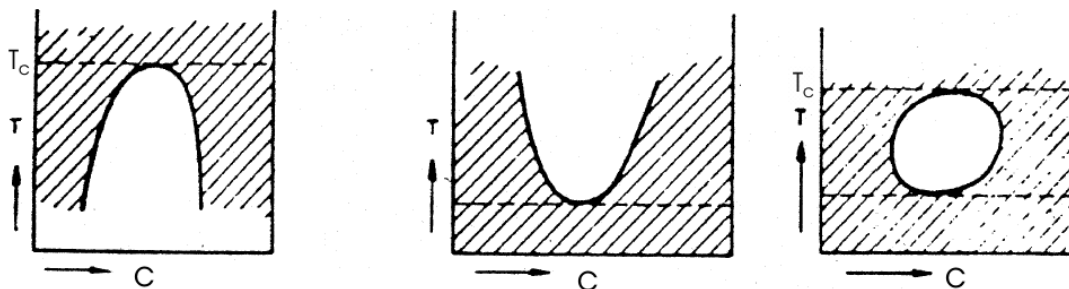


Figure 4.15.: Isobar T, c -diagrams for the phase behavior of 3D binary systems with limited miscibility in the liquid phase. In the dashed areas, a homogeneous phase of both components exists. **a)** For instance the Phenol-Water-system: a Water-rich and a Phenol-rich phase can coexist up to an upper critical solubility-temperature T_c . Above the phase boundary line, a homogeneous mixture is found at any composition, at a certain higher temperature, a liquid-gas-transition takes place; **b)** System with lower critical solubility-temperature, e.g. Triethylamin-Water; **c)** System with lower and upper critical solubility-temperature, e.g. Nicotine-Water; The assignment of the SIMP system needs further investigations, most notably variable temperature STM experiments. Graphics from [153].

With help of the thermodynamic functions, it can be tried to predict if a system is homogeneous or heterogeneous. It is deciding if the decay of an original homogeneous system into various phases is associated with an increase in entropy or not. In the first case, a freshly built phase of microscopic range will gain size at the expense of the existing ones. The system will get heterogeneous or the original phase will even disappear completely. If the entropy decreases, the microscopic new phase disappears and the system remains homogeneous.

Yet in simpler systems like real gases in 3D, e.g. Ne-Kr, there exist some cases with a

limited miscibility that results from the Coulomb-interaction between the molecules [156]. If the potential energy U_{AB} between various molecules A and B is larger than between similar components U_{AA} , resp. U_{BB} , then a mixing gap can appear, accompanied by a separation into two phases with different concentrations. But not only the orders of the potential energies are controlling the process. Furthermore, it is important how the entropy and the volume of the mixture depend on the concentration. Considering all this, the proper thermodynamic term of a mixture is its free enthalpy $G_m(P, T) = U_m - S_m T + V_m P$, m being the index for mixing. The potential part of the internal energy U_m from a mixture of two kind of molecules A and B with the concentration $c = \frac{N_B}{N_A + N_B}$ and the coordination number z (number of nearest neighbors of a molecule) (if $N_A + N_B = N$) is [157]:

$$U_m(c) = \frac{N \cdot z}{2} [(1 - c)^2 U_{AA} + 2c(1 - c)U_{AB} + c^2 U_{BB}] \quad (4.1)$$

This relation can be verified by counting the bonds of both kinds of molecules. If we assume a regular distribution of the molecules, the mean energy of a A -molecule in terms of its nearest neighbor is $\bar{U}_A = (1 - c)U_{AA} + cU_{AB}$, the one of a B -molecule is $\bar{U}_B = (1 - c)U_{AB} + cU_{BB}$. The total energy then is the sum of these average values over all molecules, i.e. $U_m = \frac{N \cdot z}{2} [(1 - c)\bar{U}_A + c\bar{U}_B]$ which is equal to (4.1). $U_m(c)$ as a function of the relative concentration c is drafted in figure 4.16 and supports the mixing.

In the case of the SIMP, $U_{AA} \approx 0.5 \text{ eV}$, the hybridization strength of the C_{60} with neighboring molecules [127], $U_{AB} \approx 0.42 \text{ eV}$ is the estimated¹³ strong C_{60} -SubPc intermixing term of Coulomb and Van der Waals interaction and $U_{BB} = 0.19 \text{ eV}$ the SubPc-SubPc interaction [75], which probably depends on the relative orientation and may alternate in sign with distance.

The entropy of a mixture is known from the thermodynamics. It is the part of the total entropy which depends only on the concentration c :

$$S_m(c) = -k \cdot N [(1 - c) \ln(1 - c) + c \cdot \ln(c)]. \quad (4.2)$$

This relation is obtained by counting the possibilities to distribute $N_B = cN$ molecules B and $N_A = (1 - c)N$ molecules A to $N = N_A + N_B$ places, namely $g(N, c) = \frac{N!}{[(1 - c)N]! \cdot [cN]!}$.

The mixing-entropy then is $S_m = k \cdot \ln g$. An approximation of the logarithm for $N \gg 1$ with help of the Stirling equation leads to equation (4.2). $S_m(c)$ as a function of the relative concentration c is drafted in figure 4.16. The presence of two components in the mixed phase is preferred.

The volume of a mixture is not easily calculated as a function of the concentration. Therefore, in place of using the free enthalpy G_m , we look at the free energy (Helmholtz-Potential, the energy available for doing work or the energy that gives the forces [139])

$$F_m = U_m - S_m T, \quad (4.3)$$

¹³Empirically varied to enable to two well-pronounced minima of the free energy F_m .

4. Intermixing Mechanism

the convenient thermodynamic potential for constant T and constant V . $F_m(c)$ as a function of the concentration c is drafted in figure 4.16 for positive mixing energy. The competition between entropy and energy finally determines the situation of the phases. Only if U_m is convex against the c -axis (positive mixing energy $U_{AB} > \frac{U_{AA}+U_{BB}}{2}$), $F_m = U_m - S_m T$ as a function of c can have two minima, see figure 4.17 (when the temperature is low enough). This is equivalent to two stable phases, in which the system is demixing to (at two distinct concentrations). Only at the two minima, the free energy is minimized and therefore the mixture splits up into two phases. This can happen only below the critical mixing temperature T_m , which can easily be derived from the above given relation. Below this critical temperature T_m , we find $\frac{\partial^2 F_m}{\partial c^2} < 0$. Another necessary condition to observe the intermixing effect is the value of the averaged fluctuations of the molecular kinetic energy $\langle E_{A,B}^{kin} \rangle < (U_{AB} - \frac{U_{AA}+U_{BB}}{2})$. In two-component gas systems, often high pressures are needed (Ne-Kr: $p > 1240$ bar [156]). However, with complicated molecules, in particular such with a permanent electric dipole moment as used here, phase-separations in gas domains are common even at low pressures. But because of the complex potential, calculations are impracticable. This short calculation here proves the presence of a mixing gap in the system when U_{AB} is chosen to 0.42 eV. However, the values for the potential energies still have to be determined more accurate.

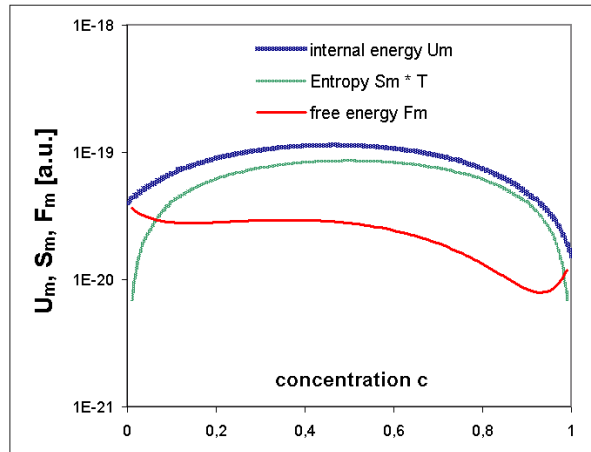


Figure 4.16.: Relation between entropy and energy for $U_{AA}=0.5$ eV [127], $U_{BB}=0.19$ eV [75], $U_{AB}=0.42$ eV. At the relative concentration $c=0$, only A -molecules exist, $c=1$ stands for the pure B phase. The competition between energy and entropy determines the emerging phases.

With regard to figures 4.18 and 4.19 we recognize that the compact $(2\sqrt{3} \times 2\sqrt{3})R \pm 30^\circ$ structure of pure C_{60} is closed by straight borderlines with 120° angles. This can be interpreted as a minimization of the interface (phase boundary lines) and the phase boundary energy¹⁴. In other words, the fullerenes tend to aggregate and maximize their number of

¹⁴This is the change in energy that appears when a molecule is brought from the inside of the system to its surface.

neighbors. The result is the best approximation to a circle on a (111) lattice which is a hexagon itself.

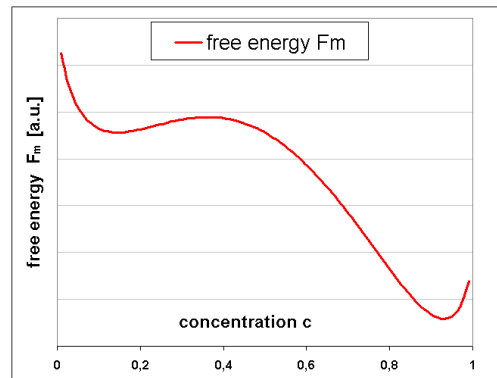


Figure 4.17.: In a mixed system, the free energy can have two minima, leading to a demixing at distinct concentrations of the components.

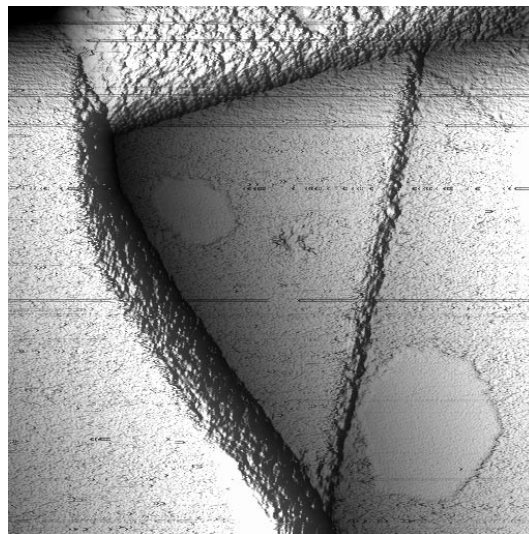


Figure 4.18.: Rough Ag(111) surface with C_{60} islands of hexagonal shape. The derivative of the piezo-movement is displayed to simultaneously show the details within the terrace and the huge step bunches. The C_{60} molecules are individually resolved when scanned on a reduced area (not shown here). The fullerenes tend to aggregate and maximize their number of neighbors. This results in a hexagon with the preferred border/inside ratio. Scan range 170 nm x 170 nm. $V_{bias} = 2$ V, $I_t = 15$ pA.

4. Intermixing Mechanism

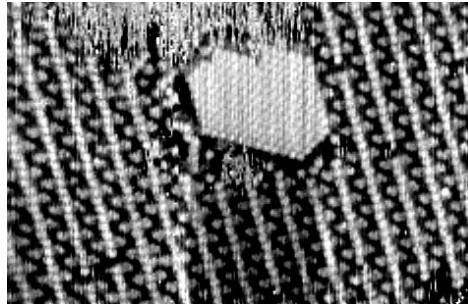


Figure 4.19.: *Stripe* domain containing a pure C_{60} island. The interior angles of the island always are 120° . This conglomeration of the exceeding fullerenes shows the minimization of the phase boundary lines and the phase boundary energy. Scan Range 50 nm x 30 nm. $V_{bias} = 1.3$ V, $I_t = 20$ pA.

4.4. Typically Segregating System: Perylen – C₆₀ Codeposited on Ag(100)

As another system of coadsorbed molecules, C₆₀ and Perylenes on Ag(100) was studied. Here, the molecules do not intermix, but segregate into single component phases. The (100) substrate orientation was selected because its symmetry agrees with the rectangular-shaped Perylenes, see figure 4.23. Details about the Ag(100) substrate and its preparation can be found in section 2.2.

4.4.1. C₆₀ on Ag(100)

The single component C₆₀-phase on Ag(100) (see figure 4.20) shows that the C₆₀ molecules are randomly ordered after the deposition process at room-temperature. There is no evidence of any preferential growth direction, and large holes are present inside the islands [117]. The (100) surface of this fcc crystal is rougher than the (111) surface [158] (see figure 2.3), and the molecules cannot cross the diffusion barrier to aggregate in compact islands. The lateral forces play a minor role. Only after an annealing cycle at 570 K for 10 minutes, they aggregate into dense islands, see figure 4.21. Remarkably, in these islands they can have two distinct heights, see figure 4.22. The islands are formed by bright and dark molecules which are organized along preferential directions. Looking in more detail, it is possible to distinguish two predominant arrangements of the bright C₆₀ molecules (zigzag and square structure). The bright fullerenes align along preferential directions after annealing and form a rectangular c(6x4) superstructure. A third structure (linear) was seen by [117]. The number of bright C₆₀ molecules is around 18% of the total molecules, and they do not change brightness in time, in contrast to other metal substrates. This can be attributed to a different chemical bonding to the substrate [112, 114]. On Ag(100) with a lattice unit of 0.409 nm, the intermolecular distance is 1.042 nm which is slightly larger than in bulk fcc C₆₀ crystals (1.002 nm). The corrugation of the second layer (<0.1 nm) is smaller than the first layer (<0.2 nm) and without any difference in brightness, as is also seen on Ag(111) [142]. The reason could be a wobbling of the molecules during the scan, because it is known that the second layer is weaker bonded to the substrate than the first one and is not modified by direct substrate interaction [142]. This would enhance the mobility of the molecules in the 2nd layer and lead to a more smeared out appearance in STM images. Since there is no difference in brightness in the second layer, the adsorption site on the substrate is responsible for the observed film morphology [117].

The changeover from identical molecules in as-grown film to bright and dim molecules in annealed film is explained by the following model [117]: When a C₆₀ molecule is deposited onto the Ag(100) surface at room-temperature, it is free to rotate at the bulk rate of 10⁹ s⁻¹ [112] like in the C₆₀ crystal [159]. In these conditions, the molecule is not chemically bonded, and the charge transfer is inhibited or less effective. After annealing, the charge transfer sets in,¹⁵ promoting the bonding of C₆₀ molecules and stopping the free rotational

¹⁵1.7 ± 0.08 electrons from the Ag(100) to the C₆₀ molecule [160].

4. Intermixing Mechanism

motion or at least damping it down substantially [128]. At the end of this process, the molecules have assumed the equilibrium configuration, where the bright and dark ones differ in their orientation with respect to the metal surface and, consequently, with respect to the vacuum [112].

Thin crystalline films grow near equilibrium by one of the following three mechanism: the Frank-van-der-Merwe (FM), the Stranski-Krastanov (SK), and the Volmer-Weber (VW) modes [161]. These growth modes are determined based on relative magnitudes of the surface energies of the substrate, the film and their interfacial energy [115]. Figure 4.20 and other studies [112, 114] show that surface energies at the C_{60} -Ag(100) (and also at the C_{60} -Ag(111)) interface satisfy the conditions for FM growth. Because of charge transfer across the C_{60} -Ag interface, the forces binding the C_{60} molecules to their substrate are stronger than van der Waals forces among these molecules, ensuring the first layer growth in the FM mode [115]. According to these STM studies the first-layer molecules form a full monolayer coverage, completing their growth before the nucleation in the second layer [112, 114]. These studies have also shown that the second-layer molecules form close-packed structures without altering orientations of the first-layer domains.

It is also possible that the surface structure of the substrate may undergo reconstruction, given the strength of interactions due to charge transfer at the interface. If these interactions displace the surface atoms from their bulk termination positions, the substrate surface may restructure to minimize its energy. However, this and other STM studies [112, 114] have found no evidence suggesting that C_{60} molecules induce reconstruction on the Ag surface.

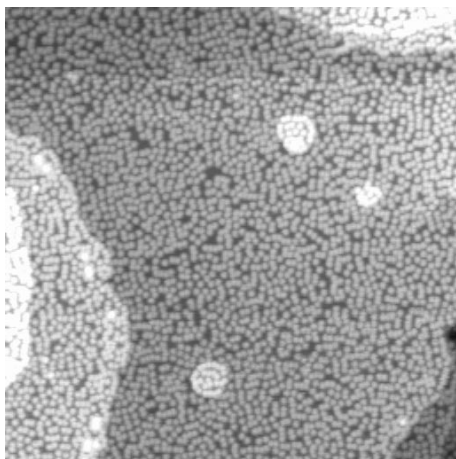


Figure 4.20.: C_{60} on Ag(100): After room-temperature deposition, the molecules are randomly distributed over several terraces. Only when the 1st layer is full, a 2nd layer can grow. Scan range 95 nm x 95 nm. $V_{bias} = 2.5$ V, $I_t = 30$ pA.

4.4. Typically Segregating System: Perylen – C₆₀ Codeposited on Ag(100)

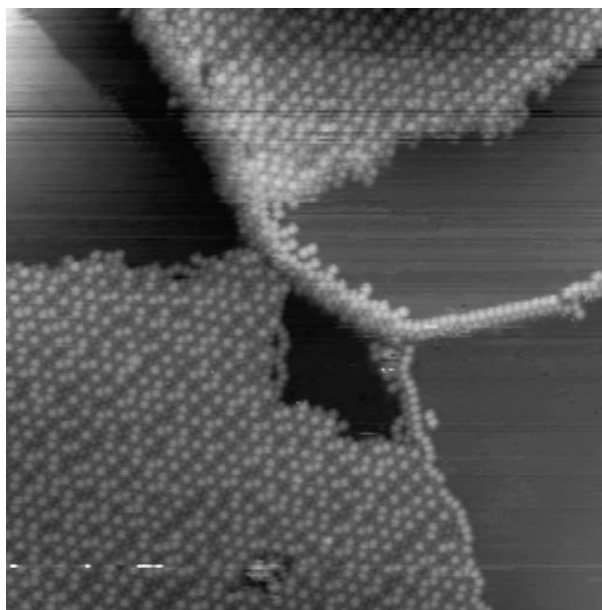


Figure 4.21.: C₆₀ on Ag(100) after annealing to 570 K for 10 minutes. Densely-packed islands are formed. Due to different chemical bonding to the substrate, bright and dark C₆₀ molecules appear. The bright molecules form pseudo-periodic structures. Scan range 65 nm x 65 nm. $V_{bias} = 1.8$ V, $I_t = 30$ pA.

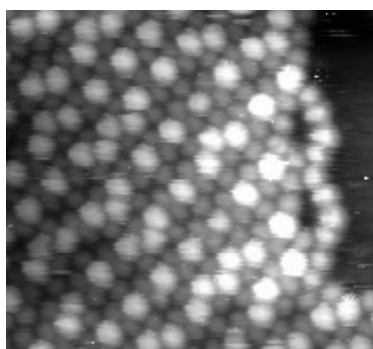


Figure 4.22.: C₆₀ on Ag(100) after annealing to 570 K for 10 minutes. The bright molecules are distributed in zigzag or square structures along a preferential orientation. Scan range 17 nm x 17 nm. $V_{bias} = 1.8$ V, $I_t = 30$ pA.

4. Intermixing Mechanism

4.4.2. Silated Perylenes on Ag(100)

In recent years, Perylen has become a model molecule for the investigation of the interaction of functionalized polycyclic aromatic molecules with solid surfaces [152, 162, 163]. Figures 4.23 and 4.27 show the N, N', N'', N''' -Tetra(trimethylsilyl)-4,9-diamino-perylenchinon-3,10-diimin molecule (from now on called *Perylen*) in a space-filling model. In condensed 3D crystals, these molecules form a monoclin structure (see figure 4.24) with space group $p2_1/c$, $a=13.73(2)$ Å, $b=10.587(10)$ Å, $c=12.885(10)$ Å, $\beta=111.32(7)^\circ$, $V=1744(3)$ Å³, $Z=2$, $\rho_{calc.}=1.141$ mg/m³. The melting point of $C_{32}H_{46}N_4Si_4$ is 485 K [164]. In 3D the molecules are connected to each other via the trimethyl-silyl ligands.

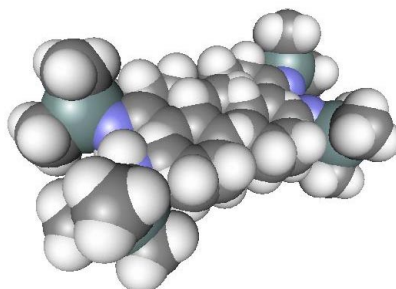


Figure 4.23.: Space-filling model of the N, N', N'', N''' -Tetra(trimethylsilyl)- 4,9 -diamino-perylenchinon-3,10-diimin molecule. Colors specify different elements: white: H, black C, blue N, green Si. For the chemical structure see figure 4.27.

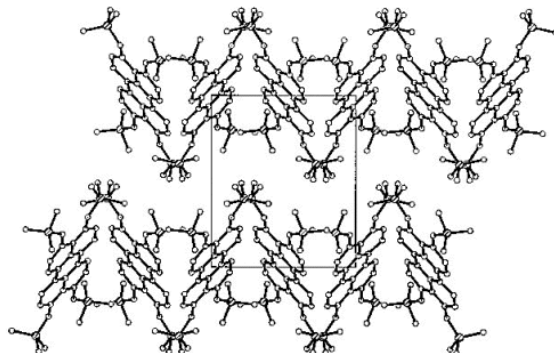


Figure 4.24.: 3D Crystal packing of N, N', N'', N''' -Tetra(trimethylsilyl)-4,9-diamino-perylenchinon-3,10-diimin [164].

The monolayer structure is very different from the 3D crystal structure, see figure 4.24. When adsorbed onto Ag(100) (see section 2.2) and confined to 2D, they lay flat on the substrate because of π -metal interaction of the aromatic Perylen-core. The binding probably is not as strong as in the case of unsubstituted perylenes which bind with a quite strong

4.4. Typically Segregating System: Perylen – C₆₀ Codeposited on Ag(100)

covalent character [165]. The trimethylsilyl ligands presumably elevate the perylen core and lead to a weaker physisorption of the molecules. In spite of the averaging over the lateral corrugation of the surface potential, each Perylen molecule adsorbs at a specific adsorption site: the molecules arrange in a so-called *herringbone* structure where each molecule is oriented perpendicular to its neighbor, see molecular-resolved islands in figures 4.25 and 4.26. The self-organization occurs at room-temperature without any additional annealing. The length of the overlayer unit-cell is 2.8 nm. The electron distribution in the molecules favors this orthogonal arrangement (see the electrostatic potential surfaces in figure 4.27). In this system, again the domain boundary energy plays an important role. The islands prefer to be closed by straight lines and angles of 90°, as can be seen in figure 4.26. Neighbored domains can differ in angle, preferred 54°, as can be seen in figure 4.28. Amusingly, this pattern is popular in macroscopic objects like floor panels, as can be seen in the photo, figure 4.29.

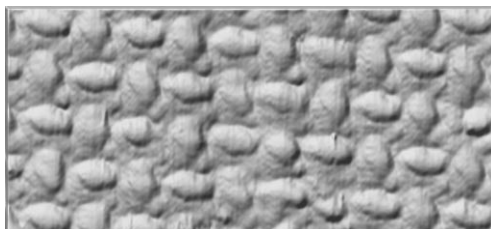


Figure 4.25.: Perylen arrangement in 2D on a Ag(100) surface: STM measurement reveal a molecular herringbone structure. Scan range 15 nm x 7 nm. $V_{bias} = 1.8$ V, $I_t = 60$ pA. The derivative of the piezo-movement is shown.

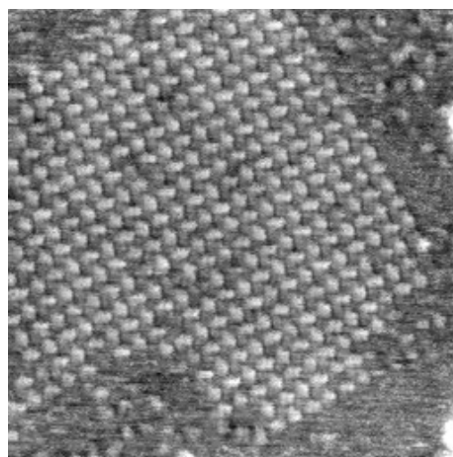


Figure 4.26.: Perylen molecules form a perfect herringbone structure on Ag(100). The island is preferential closed by straight lines. Scan range 33 nm x 33 nm. $V_{bias} = 1.8$ V, $I_t = 20$ pA.

4. Intermixing Mechanism

4.4.3. Mixture C₆₀ – Perylen

This system leads to segregation because the individual components strongly aggregate to pure phases and U_{AB} , the C₆₀-Perylen-mixing energy, is not strong enough to overcome this process: $U_{AB} < \frac{U_{AA}+U_{BB}}{2}$. Figure 4.30 shows a Perylen-island of herringbone pattern,

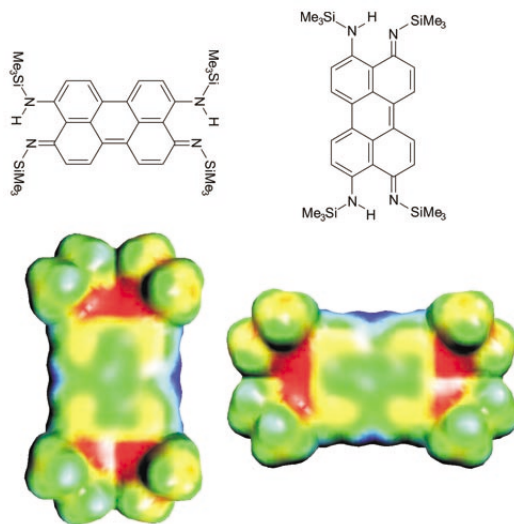


Figure 4.27.: The Perylene molecules arrange in a *herringbone* structure where every molecule is oriented perpendicular to its neighbors. The molecules are lying flat on the substrate for a strong π -orbital-substrate overlap. The electron distribution in the molecules, as is seen in the electrostatic potential surface, favors the orthogonal arrangement.

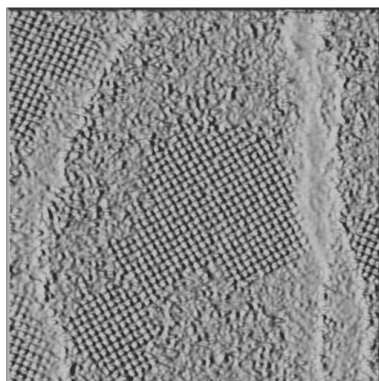


Figure 4.28.: STM measurement of Perylene herringbone domains with different angular orientation on a stepped Ag(100) surface. The molecules self-assemble without additional annealing. Scan range 71 nm x 71 nm. $V_{bias} = 0.7$ V, $I_t = 20$ pA. The derivative of the piezo-movement is shown.

4.4. Typically Segregating System: Perylen – C₆₀ Codeposited on Ag(100)

surrounded by disordered C₆₀ molecules. No intermixing takes place. Potential mixed phases obviously have a higher free energy F_m than the two segregating phases.

Different annealing cycles up to 560 K for 15 minutes were performed to overcome potential mixing barrier. Even with help of this activation energy¹⁶, the molecules do not mix. No changes can be observed in the pattern, except a slight reorganization of the fullerenes into a more regular arrangement.

¹⁶so as applied to pure C₆₀



Figure 4.29.: Photo of a floor panel with herring-bone structure. Image size 1 m x 0.66 m.

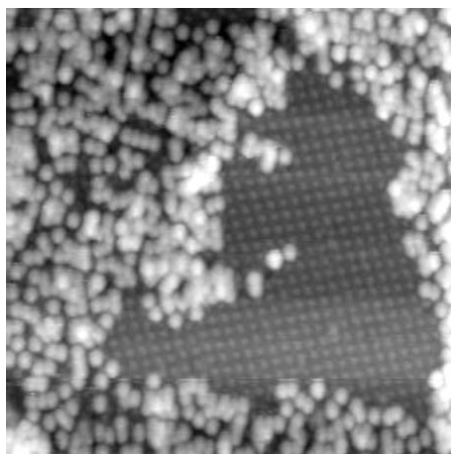


Figure 4.30.: This image shows the segregating system Perylen – C₆₀ on Ag(100). The Perylenes form a perfect herringbone structure, while the fullerenes arrange around the Perylen-island. Imaged after annealing to 560 K for 15 minutes. Longer annealing induces pseudo-periodic structures in the C₆₀ islands but no intermixing. Scan range 52 nm x 52 nm, $V_{bias} = 1.8$ V, $I_t = 24$ pA.

5. Conclusion and Outlook

The production of such self-assembled intermixed molecular monolayers is an important step on the route to the creation of self-assembled functional devices such as molecular data storage or arrays of nano-wires. Thus the here presented technique has the potential for a novel concept for the growth of organic anisotropic thin films and nano-structures at surfaces. The observed intermixed pattern asks for further use in experiments and later maybe even in applications. Some ideas are discussed in this chapter. The potential of this new method, which currently is available for licencing [166], is shown. Finally, some concluding remarks close this chapter.

Bistability: A missing fullerene in a stripe leads to dynamics of the adjacent C_{60} . Figure 5.1 shows reversible changes of the molecular position as probably induced by the scanning tip at room-temperature. The C_{60} close to the vacancy, as shown in the top of this figure, has been shown to hop between two different positions at a frequency (at least) in the order of the scanning frequency (\sim Hz). This experiment clearly demonstrates the reproducibility of the positional switching.

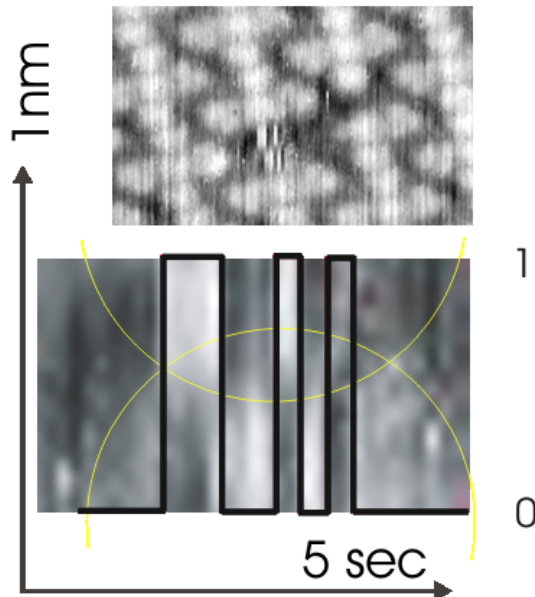


Figure 5.1.: Within a stripe, a single C_{60} molecule reversibly jumps between two metastable positions which could be assigned to bit-states. In this illustration, the fast scan direction is vertical.

Self-repairing: All patterns of the schematic room-temperature phase diagram (figure 3.15) can be found directly after the room-temperature deposition, i.e. without any additional annealing. But for an energetic consideration we have to take into account the kinetic energy which is provided during the deposition.¹ This could in principle supply the activation energy needed for the pattern formation.

Figure 5.2a shows the known *stripe* pattern. In this experiment, a deliberate destruction of the pattern with the STM tip through lowering the tunneling resistance was carried out. The pattern then is distorted (figure 5.2b). Later, the pattern is slowly reshaping towards the original arrangement (figure 5.2c and d). This proves the ample mixing energy at room-temperature. The rebuilding process was monitored over time and is shown in figure 5.3.

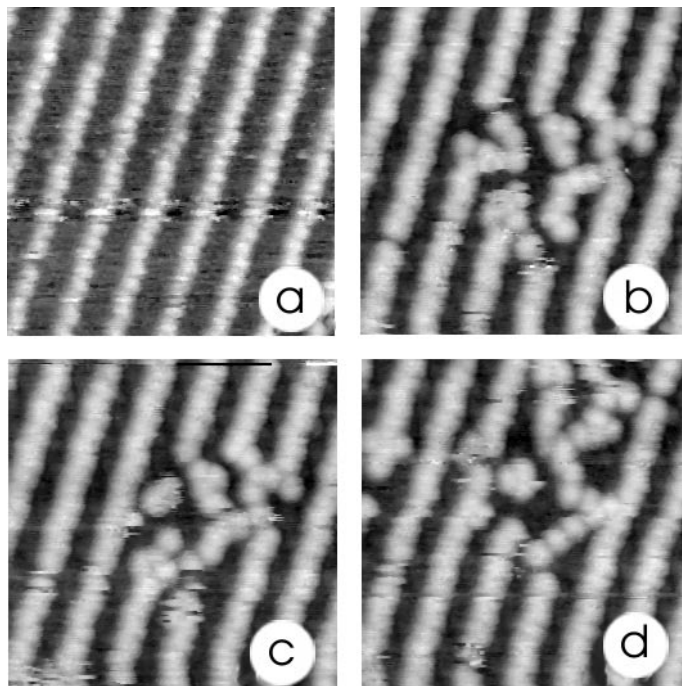


Figure 5.2.: Self-healing of the *stripe* pattern: **a)** Perfect *stripe* domain, recorded at $V_{bias} = 1.6$ V, $I_t = 20$ pA, tunneling resistance $R_t = 80$ G Ω , scan range 22 nm x 22 nm, time 0 s. Notice that the SubPc molecules are hardly visible due to the rather low bias voltage V_{bias} of 0.7 V (section 4.2.3). **b)** Same area after a tip-induced distortion at the center of the image (16 mV bias voltage V_{bias} during ≈ 50 ms for a lower tunneling resistance of $R_t = 800$ M Ω). Four stripes are perturbed. Image recorded with the same tunneling and scan parameters as in a). Time 170 s. **c)** Left row is recovered. Three rows still are broken. Time 227 s. **d)** Only two rows remain broken. Time 332 s.

¹The C₆₀ molecules are deposited at ≈ 570 K which gives them a kinetic energy of $kT = 1.38 \cdot 10^{-23} \text{ JK}^{-1} \cdot 570 \text{ K} = 7.9 \cdot 10^{-21} \text{ J} \approx 50 \text{ meV}$.

5. Conclusion and Outlook

Improvements of production: It was shown that islands of this new material that are ≈ 100 nm in extent can be created. Analysis of many such images taken from several samples indicates that these ordered regions represent about 10% of the surface. Preliminary experiments indicate that it should be possible to grow these islands much larger, perhaps to entirely cover a metal support. Parameters that could produce changes in island size may be (1) the deposition rate, (2) the relative rates of arrival of the components, (3) the substrate temperature during deposition, (4) the post-deposition annealing, (5) using derivatives of the chemical components, and (6) using single crystals as substrates in place of multi-domain films. Modifications of these layers in terms of both electron transport properties and the addition of substituents are possible to engineer. I believe this is only the first in a broad new class of materials based both upon weak intermolecular interactions and image charges associated with adsorption on metal surfaces. What remains to be seen is whether these structures can be extended upward by sequential deposition to produce new three-dimensional materials and whether the individual components can be manipulated reproducibly.

Nanowires: For future application, it would be interesting to have conducting nanowires. It is not clear a priori, if the chains in the *stripe* pattern are conducting, i.e. if there is enough overlap between individual C_{60} molecules. It is however possible to polymerize molecules of a SAM pattern to make them electrical conducting by electron radiation of ca. $1000 \mu C/cm^2$ [167]. The thiols themselves are better decoupled from the substrate because they are attached by σ -bonds. π -adsorption (unfortunately) leads to a better substrate coupling. The polymerization and functionalization is an active research field [168, 169]. For an application, of course, the wires have to be electronically decoupled from their support. The wires therefore have to be grown on an insulator which is not at all clear to work at the moment. Experiments have to be done with scanning probe techniques to check pattern formation on insulators.

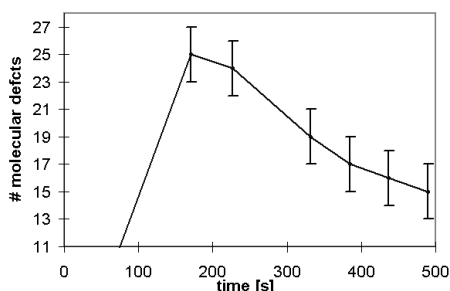


Figure 5.3.: After a tip-crash, the *stripe* pattern restores naturally. 500 sec after the destruction, 40% of the initially replaced molecules are “naturally” reassembled in the original pattern.

Storage device: In a visionary context and on the basis of the described inventions, it seems plausible that there may be technological implementations of single molecule storage on the SIMP materials. The structures have a potential to serve as data storage devices [170]. The large spacing between the molecules enables a variety of different assignments between molecular arrangement and “information bit” patterns: The pseudo linear arrays of C_{60} molecules can be taken as “hard” formatted track marks to identify the positions of each SubPc molecule within one line. After re-positioning of individual SubPc molecules [171–178], the modified pattern can be associated with a bit pattern. A global “reset” could be applied by a controlled annealing cycle as discussed in the previous section. A treatment at elevated temperature could be used to assemble the molecules in their original position. This may be useful to erase written information in a self-assembled data storage layer. Therefore the next experimental step would be the use a variable temperature STM and additionally the capability of manipulate single molecules.

Using these patterns, a limit in the order of Tbyte/Inch² could be approached, which is 2-3 magnitudes higher than that of the currently established “edge of technology” magnetic or optical storage techniques. The exact 2D registry of the SIMP and the recognition of molecules and their position allows for numerous variations in data bit to 2D pattern assignments: Redundant storage, parity bits and the assignment of “words” as multiple bytes are straightforward generalizations of the here proposed basic scheme.

One of the obvious limitations of these SPM based data storage techniques is the speed. The “Millipede”TM [179] approach serves as a parallel interface to circumvent the limitations of the inherently slow read/write cycles in polymer indentations. Our approach has an exceptionally high signal to noise ratio in STM: In Figure 5.4 it is shown, that a data trace (cross section of STM image over the stripe with a C_{60} vacancy in figure 3.10) taken at 1 kHz bandwidth leads to a clear identification of vacancy and occupancy site. This high signal to noise ratio in the order of 20 suggests that significant speed can still be gained in the individual read/write cycles.

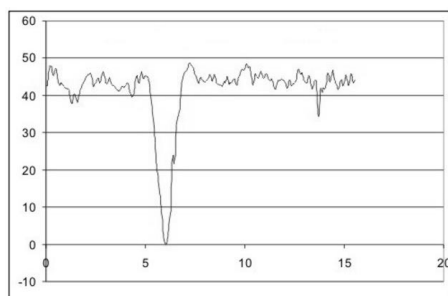


Figure 5.4.: The line-scan over the stripe with two missing C_{60} molecules from figure 3.10 shows the high signal/noise ratio of the potential storage device.

Concluding remarks: We conclude that the observed mode of self-assembly and intermixing emerges from a delicate balance of electrostatic and Van der Waals interactions between

5. *Conclusion and Outlook*

static and fluctuating charge distributions of predominantly polar and polarizable molecules which are bound non covalently onto a polarizable metallic substrate. Each SIMP has its specific structure, composition, symmetry and surface density. The type of pattern can be controlled by the ratio of the two molecular components during the deposition. The exact arrangement of the molecules within the 2D layers described here, offers possibilities beyond the properties which have made SAMs so useful. For the first time, control over the ordering of intermixed arrays of functionalizable molecules created by self-assembly has been demonstrated over hundreds of nanometers. The relatively large spacing between the molecules leaves room for local rearrangements which are currently under study. This motivates the exploration of nanoscale data storage concepts, and the study of electronic [180] and mechanical [140] processes at a single-molecule level, which has often been hampered by the difficulty to identify individual incorporated molecules when using other techniques of self-assembly [181].

A. Porphyrins: A Model Molecule to Study Conformational Flexure and Switching

In this chapter, molecular conformation of a surface adsorbate, Porphyrin, will be discussed, as well as its recognition by Scanning Tunneling Microscope. When a large molecule is adsorbed on a metallic surface, its internal conformation is generally modified leading to a change in its mechanics, electronic transparency and chemical reactivity. It is therefore of fundamental importance to be able to determine the internal configuration of a molecule when adsorbed on a metallic surface. In this respect, STM is a unique experimental method, which contemporarily allows to image the molecule on a surface [90, 182, 183] and to manipulate it [171–176].

The special quality of a molecule is that in its entity, it can be readily modified by synthetic chemists such that its interaction with both the tip and surface are specially designed and controlled. Such “synthetic” molecules can also be used as “building blocks” for artificial supra-molecular structures [68]. By their larger sub-units, molecular orientation can be recognized in STM data which is not possible for single atoms. The free conformation of a molecule in vacuum can be modified when adsorbed on a surface and also the substrate can undergo adsorbate-induced reconstructions [184]. In conjunction with chapter 3, it is interesting to note that the conformation of an adsorbed molecule can be changed by a coadsorbate. Benzene for instance, undergoes a triangular distortion towards Kekule-benzene on Ru(001) when NO [93] or CO [88] is codeposited on Pt(111).

The molecular structure and vacuum conformation of the investigated Porphyrin molecule are described in section A.1. Section A.2 gives an introduction into the subject of molecular conformation. The molecule, adsorbed on Ag(100), with all its features like step-edge decoration, island formation, asymmetric conformation, and switching is discussed in section A.3. Section A.4 finally concludes the observations.

A.1. Structure of a Free Cu-TBPP Molecule

Cu-tetra-[3,5 *di-ter-butyl-phenyl*] porphyrin (Cu-TBPP) belongs to a class of porphyrins with four phenyl-based substituents of symmetrically bonded, interconnecting carbon atoms on pyrrole rings [185], see figure A.3. Figures A.1 and A.2 show a space-filling model of the molecule. Cu-TBPP is an organic molecule where well-defined structural changes can be found: the substituents can be rotated around the σ -single bonds. Two pairs of sterically interacting H electron shells exist for the planar orientation of the substituent at the top right of figure A.2. The overall structure of TPP derivatives can be ascribed to a steric repulsion between the ortho-substituents on the phenyl ring and the outermost substituents on the pyrrole ring. Together with the competing effect of the degree of overlap with the porphyrin

A. Porphyrins: A Model Molecule to Study Conformational Flexure and Switching

ring, this repulsion determines the rotation of the phenyl groups. Thus, the rotation angle around each of the four phenyl-porphyrin σ -single bonds is the predominant factor that determines the shape of Cu-TBPP. X-ray diffraction has shown that tetraphenyl porphyrins TPP derivatives exhibit dihedral angles of 60-90° between the porphyrin ring and the phenyl substituents in bulk crystal samples, depending on the nature of the substitution and their local environment. In vacuum, the *di-t-butylphenyl* substituents are oriented out of plane with the porphyrin in the minimum energy state, see figure A.1.

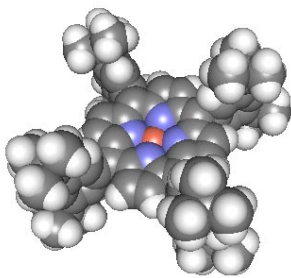


Figure A.1.: Relaxed geometry (vacuum conformation) of a single free Cu-TBPP molecule. Colors specify different elements: C, dark gray; H, white; N, blue; Cu, red (see figure A.3). The molecule has a diameter of about 2 nm and is about 0.9 nm high.

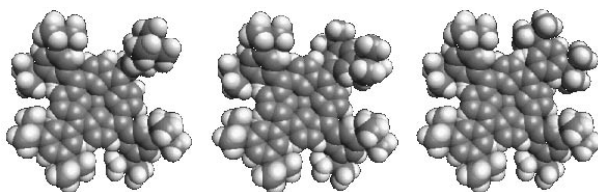


Figure A.2.: Series of space-filling models, showing the rotation of the upper right TBP-group around a σ -single bond.

A.2. Molecular Conformation

Properties of molecular material generally derive from the chemical and physical properties of each molecular sub-unit and from cooperative phenomena like conductivity. Next to the chemical structure of a molecule which is fixed during chemical synthesis, the specific shape of the molecule is defined by bond rotation, bending and flexure. This shape which is generally referred to as a molecule's *conformation* is a predominant factor for “functional” properties of the molecular material in all molecular sciences. Both physical and chemical properties of functional molecules as well as cooperative bulk behavior can be modified

by changing conformation. The particular important role of molecular conformation in life-science systems was recognized when the 3D electron density maps of bio-molecules were resolved in X-ray crystallography [186]. Later, this method was complemented with NMR techniques [187, 188] and molecular modeling (see section 2.6) to understand and visualize complex proteins. Up to now, one central challenge in life sciences remains the understanding of “Structure Function Relationship” towards the prediction of molecular function and properties given the synthesized structure of a molecule.

In this chapter, the goal is to shed some light at the concept of conformation for molecules when adsorbed at surfaces and interfaces. First it is important to note that none of the above-mentioned experimental techniques has given clues about the exact structure of molecules when in contact with a solid or liquid surface. Single parametric techniques like UV, vis. or X-ray Spectroscopy give only scarce insight into the exact structure of molecules. Diffusion measurements and surface X-ray Diffraction have revealed important statistical information about molecular motion and packing. For single molecular objects and small numbers of molecular assemblies, however, all these techniques fail due to their statistical nature. Small amounts of molecular material at surfaces, do not provide enough signal for analysis and furthermore, there is little clue about the exact atomic positions. Only recently, Jung et al. [140] have proven the conformational identification of individual molecules through high quality Scanning Tunneling Microscopy images with submolecular resolution. Donhauser [181] observed conformational switching of single chain-like molecules by STM and reported that the local environment is playing a critical role in the conformational relaxation. This process was further identified as an effect of the electric field rather than of the tunneling current.

In the history of biomolecular conformation, porphyrins have played a core role, as they are the group involved in oxygen binding to the heme and in photosynthesis. This role was identified from the early synthesis of the so called “picket fence” porphyrins where the porphyrin is substituted with asymmetric substituents. The asymmetry of these substituents allowed for the identification of different conformational isomers (atropisomers) which originate from the sterically hindered bond rotation of the phenyl-porphyrin bond. This was first studied by Gottwald and Ulman in 1969 [189] for tetra-arylporphyrins and compared to the simpler case of the bi-phenyl molecule. In this early experiment, column chromatography was used to identify the different isomers after isomerization which occurs at room temperature for the studied system. Hindered ligand rotation and ligand exchange are of prime interest, as they allow for the construction of bi- and multistable mechanics using molecular architecture.

Porphyrin overlays were found to order orientationally by annealing (periodic conformation orientation). The H₂-TBPP on Au(111), showed a conformational change [190] where the ground-state conformation undergoes a bending and leads to a saddle shaped structure: two opposite legs are lower. The “bending axes” of the molecules in the as grown films are random, but after annealing, an ordered superstructure can be found over large areas: neighboring molecules then show perpendicular “bending axes”.

People from the Rieder group at the Freien Universität Berlin showed a reversible modification of a porphyrin molecule on Cu(211) with an STM tip at low temperatures [176, 191].

With an Atomic Force Microscope (AFM) the behavior of the Cu-TBPP under an ex-

A. Porphyrins: A Model Molecule to Study Conformational Flexure and Switching

ternal load was investigated at room-temperature [192, 193]. Frequency-distance curves were made on the Porphyrin and indicated a conformational change of the molecule. The measured force needed to bend down a leg was approximate 0.4 nN.

The here used molecule was found to adapt itself to the substrate geometry when deposited to various substrates [140, 194]: due to its flexibility and internal degrees of freedom, the molecule undergoes substrate-induced conformational changes, as was observed with STM on Cu(100), Cu(111), Cu(211) [194], Au(110), and Ag(110) [140]. Thereby, the substituents undergo a rotation close to 90°.

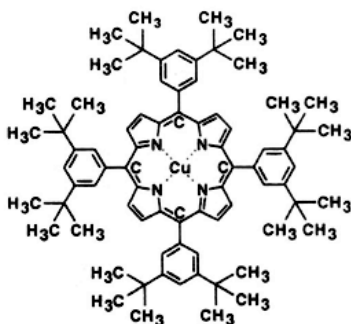


Figure A.3.: Chemical structure of Cu-tetra-[3,5 *di-ter-butyl-phenyl*] porphyrin (Cu-TBPP).

A.3. Cu-TBPP on Ag(100)

The porphyrins were deposited by evaporation at approximate 570 K from a tantalum crucible onto atomically clean Ag(100) substrate which was kept at room-temperature, see section 2.2 for the substrate preparation and and section 2.3 for details of the molecular deposition. In figure A.4 with low molecular coverage (≈ 0.05 ML), one can recognize single molecules as square shaped objects. In an overview STM image, figure A.5, one can see that the molecules are nicely aligned along the substrate step-edges. The molecules decorate the steps because they are attracted by electrostatic forces occurring at this substrate discontinuity. At the steps, the electron density does not change abruptly, but is smeared out and leads to a surface dipole, the upper level being slightly positive, the lower negative [195].

At a higher coverage, condensed islands are created. Because of the high packing density, diffusion of the molecules is further hindered and sub-molecular features are visible in high resolution STM images. Individual Cu-TBPP molecules are roughly identified as four protrusions of square shape, see for example figure A.6. Both their dimensions and theoretical STM electron-scattering quantum chemistry calculations (ESQC) confirm that the lobes correspond to the *di-t-butylphenyl* (DBP) ligands [194]. The porphyrin core does not contribute significantly to the image and appears dark because it is supported approximately 0.7 nm above the surface and consequently is electronically decoupled from the substrate, in agreement with previous investigations [174].¹ Theoretical calculations demonstrate [194]

that the tunneling current mainly flows through the legs, because the associated orbitals are coupled to the metal surface.

¹Owing to the weak overlap between the π -states of the porphyrin core and the phenyl-ligands at this bond angle, the porphyrin-phenyl bond of the TBPP is predominantly a single σ -bond that does not participate in the conjugated electron system.

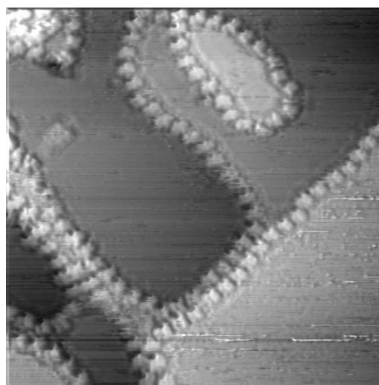


Figure A.4.: At low molecular coverage, the Cu-TBPP molecules decorate the steps of Ag(100). The molecules can be identified as single square-like objects. Scan range 40 nm x 40 nm. $V_{bias} = 1$ V, $I_t = 150$ pA.

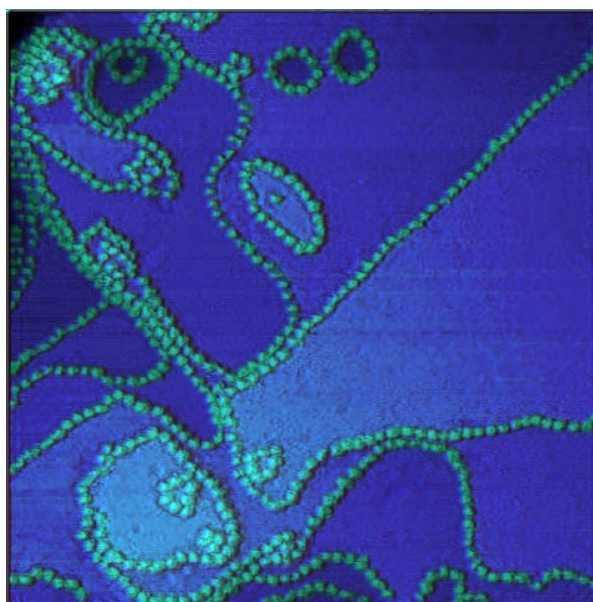


Figure A.5.: Step decoration of Cu-TBPP on Ag(100) at low molecular coverage. Scan range 112 nm x 112 nm. $V_{bias} = 1$ V, $I_t = 150$ pA. A slight median filter and superimposition of the derivative was applied. Artificially colored.

A. Porphyrins: A Model Molecule to Study Conformational Flexure and Switching

When the molecules are adsorbed onto Ag(100) at this higher coverage, they can appear in various forms, see figure A.6: There exists three different brightness' of the four legs and most of the molecules have “mickey-mouse” shape (one bright leg that is neighbored by two dimmed legs and the opposite leg is dark, see figure A.7). The asymmetric STM image

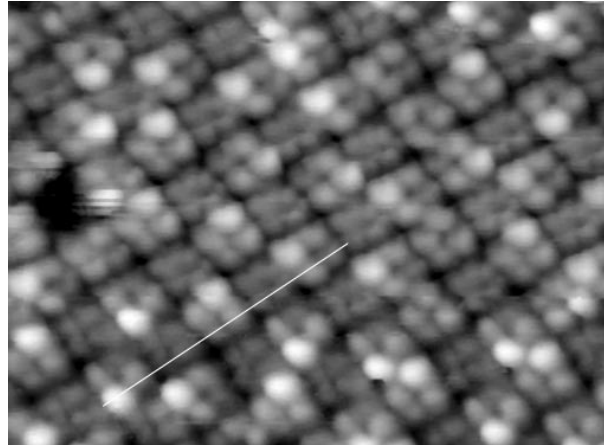


Figure A.6.: At higher coverage, the Cu-TBPP molecules form condensed islands on Ag(100). The individual legs appear with different heights. A height-profile on the marked line can be found in figure A.7. Scan range 11 nm x 8.5 nm. $V_{bias} = 1$ V, $I_t = 40$ pA.

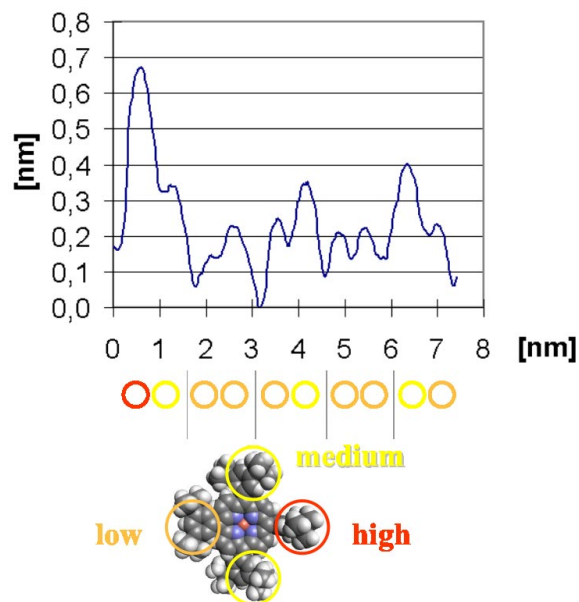


Figure A.7.: Height-profile on the line drawn in figure A.6. Different heights are assigned to different leg-orientations.

of Cu-TBPP, as is also seen on Cu(211) [194], can be explained by a conformally flexed molecule. The determination of single-molecule conformation relies on the shape of the four lobes at each molecule. The relative position of the uppermost t-butyl group corresponding to each lobe of the molecule is determined by the rotation angle for the phenyl-porphyrin bond of each DBP substituent. The turned leg leads to a different electron distribution in the molecule and therefore to a different tunneling resistance. Conformational changes affect the symmetry of the lobes and the transport probability through molecular subgroups. Unflexed Cu-TBPP molecules with four identical legs can be identified as nearest neighbors. There exist three levels of leg height, however only faint contrast variations are observed for one class of legs. Figure A.8, the histogram of illustration A.6, shows the distribution of the recorded heights: The histogram is fitted by a sum of four gaussian curves representing the Ag substrate, the low, medium and high legs, respectively. From the fit, the relative apparent heights of the three cases can be derived, as well as their percentage. The emerging heights behave like $low : medium : high = 1 : 1.34 : 2.08$. Thereby, the measured height of the *high* leg is approximate 0.6 nm. The areas scale like $low : medium : high = 1 : 1.96 : 0.4$, which means that twice as much legs are in medium position than in low position, and only half as much are in the high conformation. This is clear when we consider that the flexed molecules have one low, one high and two medium legs, but some molecules are not deformed and have four low legs.

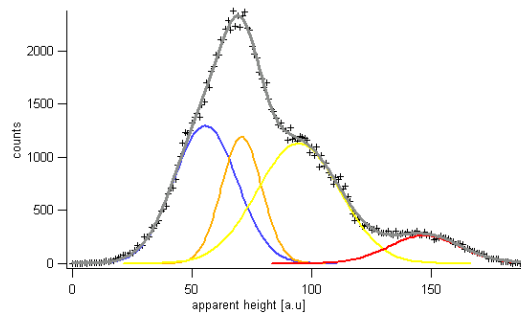


Figure A.8.: Histogram of the STM image in figure A.6: The four fitted gaussian curves represent the Ag substrate, low, medium and high legs, respectively. Most of the legs show the medium conformation and are approximately 35% smaller than the bright legs.

Because topographic STM images represent a convolution of the electronic and topographic structure of the surface (see equation (2.4)), a change of apparent height observed in STM images can thus be due to a change in the physical height of the molecule, a change in the conductivity of the molecule or both. F. Moresco [191] has shown by theoretical calculation (ESQC) that the tunneling current depends strongly on the leg orientation (several orders of magnitude). The core of the porphyrin is decoupled more in the deformed configuration than in unflexed molecules probably because the molecule is tilted and the center porphyrin plane is raised.

A. Porphyrins: A Model Molecule to Study Conformational Flexure and Switching

It is assumed that the legs are turned out of the perpendicular equilibrium state because of the interaction with the Ag(100) substrate (substrate induced conformational change) that leads to a strained molecular film. The distribution of the dim and bright legs is not purely random: The bright legs are distributed in a pseudo periodic super-structure. It looks like the bright legs of different molecules repel each other, maybe due to steric interaction. Since the porphyrin powder is of high purity, it can be ruled out that the observed brightness variation is due to the presence of other molecules or defect porphyrins.

This conformational adaption within the molecules occurs in addition to the general tendency for an adsorbat molecular lattice to rotate with respect to the substrate in order to minimize the inequivalent number of adsorption sites. The different apparent heights in the STM images could in principle also be explained by different adsorption sites or by an electronic effect as in the case of the C_{60} (section 4.4.1). In connection with the discussed observation of the conformational changes with AFM and STM and the observed flexibility on different substrates, however, this conformational interpretation is justified.

The substrate cannot easily be imaged simultaneously with the molecules. But by lowering the tunneling resistance, the Ag lattice gets visible. Figure A.9 shows both, the substrate and the adsorbates, and can help to derive the exact adsorption registry.

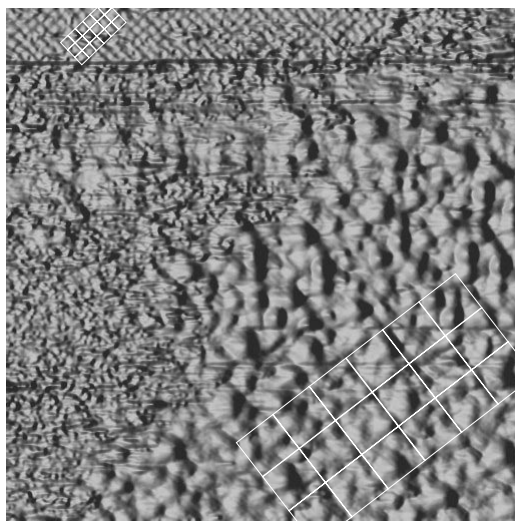


Figure A.9.: 3D illustration of an STM image with a Cu-TBPP island and atomic resolved Ag(100) substrate. The tunneling parameters were changed close to the upper end during the scan from molecule-sensitive to atom-sensitive. $V_{bias} = 1$ V, $I_t = 40$ pA for molecules (lower part); $V_{bias} = 0.1$ V, $I_t = 150$ pA, 10x faster scan-speed (0.015s/line) for atoms (upper part). The substrate lattice (with a lattice constant of 0.289 nm) and the Porphyrin superstructure (with an intermolecular-distance of 1.4 nm) are rotated approximately 6° against each other. Scan range 15 nm x 15 nm.

Spontaneous conformational change We also found that some legs change brightness, i.e., from dark to bright and vice versa during sequential imaging of the same surface area at the same scanning conditions, see figures A.10, A.11, and A.12. This effect is assumed to derive from a conformational change of the molecules. A reason for this spontaneous (or probably slightly tip-induced) intramolecular dynamic could be the overall strain in the monolayer, which is a consequence of the intermolecular and strong molecule–substrate interaction. This is also believed to lead to the asymmetric conformation because the substituents can more closely pack in this conformation. This view is supported by the observation, that neighboring molecules show correlated changes in shape: The “high” substituent avoid to exist in the nearest neighbor positions. It looks like the turned legs repel each other and a conformational change of one molecule thereby can induce a change in a second molecule, see figure A.10 a-c). The pseudo-periodic superstructure then is better conserved. The “blinking” molecules seem to be concentrated to certain regions, maybe caused by underlying substrate defects.

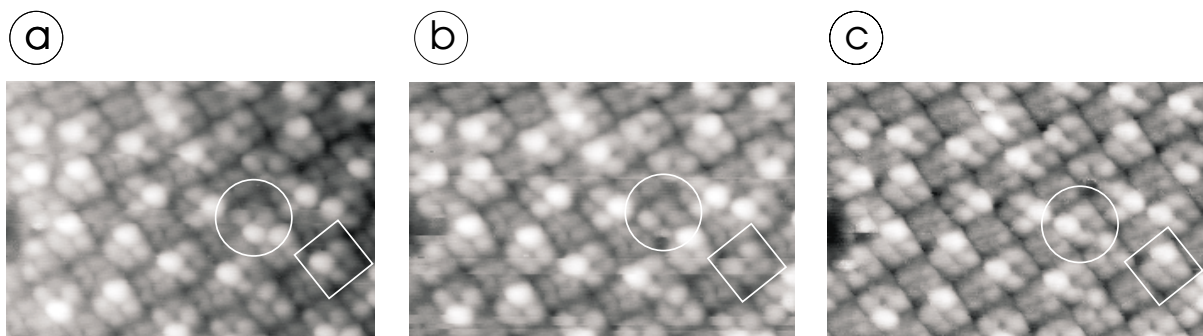


Figure A.10.: Three successive STM images **a**), **b**) and **c**) of the same Cu-TBPP island on Ag(100), recorded with identical scan and tunneling parameters. The time between the images is 103 s. The two marked molecules change the appearance during the scans: the molecule labeled by a circle changes from *south* to *west* conformation, whereas the molecule labeled by a square changes from *west* to *north* conformation. All other molecules are unaffected. Scan range 9 nm x 6.5 nm. $V_{bias} = 1$ V, $I_t = 40$ pA.

In some images, see figure A.13, there exist regions without any bright molecules. In the next scan, however, the bright features can be back at the original positions. This could be due to a tip change that turns the tip insensible for the identification of different legs and that this is an imaging effect. Thus, not every tip is sensitive enough to identify single molecules conformation.

A.4. Conclusion

The changes in the conformation and its detection render this molecule a model to study single molecular behavior. With porphyrins a single molecular storage device could be im-

A. Porphyrins: A Model Molecule to Study Conformational Flexure and Switching

plemented [197]: Apparent heights could represent the ON and OFF states of a switch. The molecules could probably be switched by an SPM tip. Or the molecules could be attached between two crossed electrodes of a nanowire array. A voltage pulse could possibly switch the molecule between two discrete states. Such devices already are under investigation, but at the moment still need thousands of molecules between the electrodes for reproducible switching [198, 199].

The idea of molecular switches is quite clear [200–202], but we have to take into account that the properties of such a switch will change dramatically when connected to wiring interfaces [203]. The molecular geometry will adapt to the environment which in turn affects the electronic structure of the first. A further drawback of the proposed storage idea is the coupling between the individual porphyrins.

In a more general sense, the observation of conformational effects for single molecules is an astounding achievement in experimental molecular science which may give us even deeper insight into important processes which occur at surfaces, like catalysis, molecular electronics and opto-electronics and tribology.

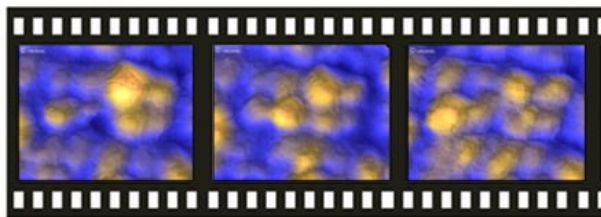


Figure A.11.: Cu-TBPP on Ag(100). The scans were completed 103 s after each other. The conformation of the two imaged molecules has repeatedly changed between the scans. This image is rendered by the *POV-Ray*TM Raytrace program packet [196]. $V_{bias} = 1$ V, $I_t = 40$ pA.

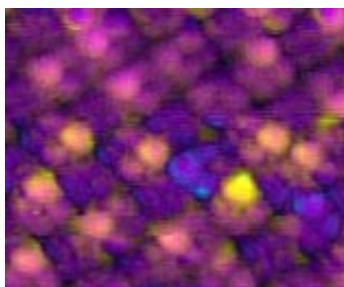


Figure A.12.: This color image is a composition of two successive STM image (from figure A.10), each with its own color (bright blue and yellow). The differences between the two images appear in the original color, whereas the unchanged areas result in purple. Two special molecules stand out due to an alteration of their conformation.

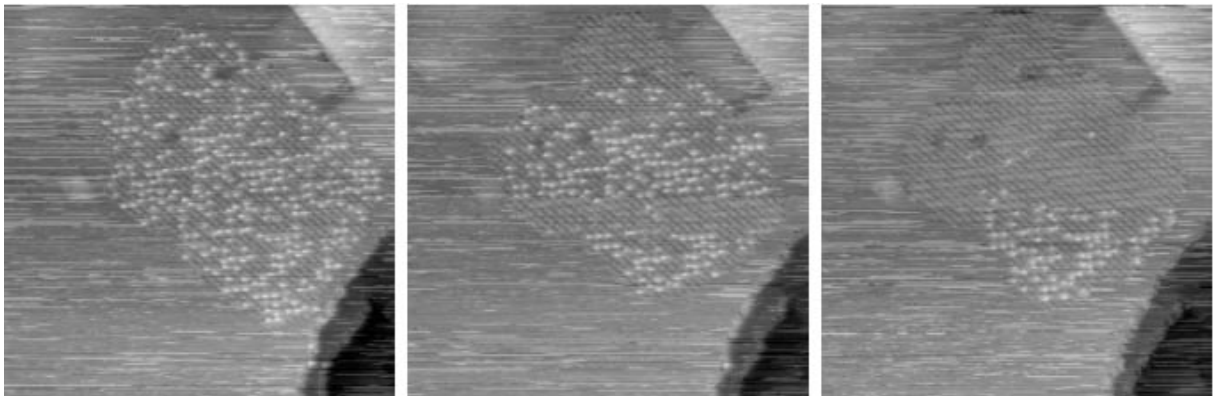


Figure A.13.: Three successive STM images of the same condensed Cu-TBPP island on Ag(100). The time between the images is 50 s. Only in some time slices during the scan, the tip had changed to become sensitive enough to distinguish between the intramolecular features of molecules with various conformation. Scan range 90 nm x 90 nm. $V_{bias} = 2.2$ V, $I_t = 20$ pA.

Bibliography

- [1] J. Jortner and M.A. Ratner, *Molecular Electronics*, Blackwell, Oxford (1997).
- [2] S. Roth and C. Joachim, *Atomic and Molecular Wires*, Kluwer, Dordrecht (1997).
- [3] C.D. Chidsey and R.W. Murray, *Electroactive Polymers And Macromolecular Electronics*, Science **231**, 25–31 (1986).
- [4] C. Joachim, *Electronics using hybrid-molecular and mono-molecular devices*, Nature **408**, 541–548 (2000).
- [5] Mark A. Ratner, *Introducing molecular electronics*, materialstoday **3**, 20–27 (2002).
- [6] F.L. Carter, *Molecular Electronic Devices*, Marcel Dekker Inc., New York (1982).
- [7] A. Aviram and M.A. Ratner, *Molecular Rectifiers*, Chem. Phys. Lett. **29**, 277–283 (1974).
- [8] B. Mann and H. Kuhn, *Tunneling Through Fatty Acid Salt Monolayers*, J. Appl. Phys. **42**, 4398 (1971).
- [9] S. Roth, S. Blumentritt, M. Burghard, E. Cammi, D. Carroll, S. Curran, G. Dusberg, K. Liu, J. Muster, G. Philipp, and T. Rabenau, *Molecular rectifiers and transistors based on π -conjugated materials*, Synthetic Metals **94**, 105–110 (1998).
- [10] J.H. Burroughes, D.D.C. Bradley, A.R. Brown, R.N. Marks, K. Mackay, R.H. Friendand, P.L. Burns, and A.B. Holmes, *Light-Emitting-Diodes Based On Conjugated Polymers*, Nature **347**, 539–541 (1990).
- [11] S.R. Forrest, *Ultrathin organic films grown by organic molecular beam deposition and related techniques*, Chem. Rev. **97**, 1793–1896 (1997).
- [12] W. Brütting, S. Berleb, and A.G.Mückl, *Device physics of organic light-emitting diodes based on molecular materials*, Org. Electron. **2**, 1–36 (2001).
- [13] H.E. Katz, *Organic molecular solids as thin film transistor semiconductors*, J. Mat. Chem. **7**, 369–376 (1997).
- [14] G. Horowitz, *Organic field-effect transistors*, Adv. Mat. **10**, 365–377 (1998).
- [15] A. Bachtold, P. Hadley, T. Nakanishi, and C. Dekker, *Logic circuits with carbon nanotube transistors*, Science **294**, 1317–1320 (2001).
- [16] J.-M. Lehn, *Supramolecular Chemistry: Concepts and Perspectives*, VCH, Basel (1995), ISBN 3-527-28330-7.
- [17] J.-M. Lehn, *Supramolecular Chemistry*, Science **260**, 1762–1763 (1993).
- [18] Makoto Fujita, *Molecular Self-Assembly*, Springer, D-Berlin (2000), ISBN 3-540-66948-5.
- [19] R. Maoz and J. Sagiv, *Penetration-Controlled Reactions In Organized Monolayer Assemblies: Aqueous Permanganate Interaction With Monolayer And Multilayer Films Of Long-Chain Surfactants*, Langmuir **3**, 1034–1044 (1987).
- [20] R.G. Nuzzo and D.L. Allara, *Adsorption Of Bifunctional Organic Disulfides On Gold Surfaces*, J. Am. Chem. Soc. **105**, 4481–4483 (1983).

- [21] G. Binnig, H. Rohrer, Ch. Gerber, and E. Weibel, *Surface Studies by Scanning Tunneling Microscopy*, Phys. Rev. Lett. **49**, 57–61 (1982).
- [22] G. Binnig and H. Rohrer, *Scanning Tunneling Microscopy*, Helvetica Physica Acta **55**, 726–735 (1982).
- [23] C.J. Chen, *Introduction to Scanning Tunneling Microscopy*, Oxford University Press, Oxford (1993).
- [24] R. Wiesendanger, *Scanning Probe Microscopy and Spectroscopy: methods and applications*, Cambridge University Press (1994), ISBN 0-521-41810-0.
- [25] E. Breuning, M. Ruben, J.-M. Lehn, F. Renz, Y. Garcia, V. Ksenofontov, P. Gütlich, E. Wegelius, and K. Rissanen, *Spin Crossover in a Supramolecular Fe₄II [2x2] Grid Triggered by Temperature, Pressure, and Light*, Ang. Chem. Int. Ed. **39**, 2504–2507 (2000).
- [26] URL: http://www.hothardware.com/hh_files/CCAM/p4northwood24g.shtml.
- [27] M. Henzler and W. Göpel, *Oberflächenphysik des Festkörpers*, B.G. Teubner Studienbücher, Stuttgart (1994), ISBN 3–519–13047–5.
- [28] Frank Meisinger, *Rastersondenmikroskopie an magnetischen Systemen*, Ph.D. thesis, Universität Basel (1999).
- [29] Dominik Schaller, *Structural and Magnetic Properties of Thin Metallic Films and Multilayers*, Ph.D. thesis, Universität Basel (1998).
- [30] T.M. Schaub, *Untersuchung nichtperiodischer Oberflächen im Ultrahochvakuum mittels Rastertunnelmikroskopie*, Ph.D. thesis, Universität Basel (1994).
- [31] D.E. Bürgler, C.M. Schmidt, J.A. Wolf, T.M. Schaub, and H.-J. Güntherodt, *Ag films on Fe/GaAs(001): from clean surfaces to atomic Ga structures*, Surf. Sci. **316**, 295–305 (1996).
- [32] C.M. Schmidt, *Magnetic Interlayer Exchange Coupling in Fe/Cr/Fe(001) Trilayers is Correlated to Nanometer Scale Lateral Interface Structure*, Ph.D. thesis, Universität Basel (1998).
- [33] S. Berner, *Molecular Diffusion and Self-Organization on Metal Surfaces: Sub-Phthalocyanine on Ag(111)*, Ph.D. thesis, Universität Basel (2002).
- [34] Berichte und Mitteilungen, Fritz-Haber-Institut der Max-Planck-Gesellschaft, Berlin, I/1999.
- [35] D.W. Phasley, Philosophical-Magazine-A (Physics of Condensed Matter, Defects and Mechanical Properties) **4**, 316 (1959).
- [36] H.-J. Güntherodt and R. Wiesendanger (Eds.), *Scanning Tunneling Microscopy I, Springer Series in Surface Sciences*, 20, Springer-Verlag, Berlin (1992).
- [37] H.-J. Güntherodt and R. Wiesendanger (Eds.), *Scanning Tunneling Microscopy II, Springer Series in Surface Sciences*, 28, Springer-Verlag, Berlin (1992).
- [38] H.-J. Güntherodt and R. Wiesendanger (Eds.), *Scanning Tunneling Microscopy III, Springer Series in Surface Sciences*, 29, Springer-Verlag, Berlin (1993).
- [39] G. Binnig and H. Rohrer, *Scanning Tunneling Microscopy*, Surf. Sci. **126**, 236–244 (1983).
- [40] J.B. Pendry, A.B. Prêtre, and B.C.H. Krutzen, *Theory of the scanning tunneling microscope*, J. Phys.: Condens. Matter **3**, 4313–4321 (1991).
- [41] J. Bardeen, *Tunnelling From A Many-Particle Point of View*, Phys. Rev. Lett. **6**, 57 (1961).

Bibliography

- [42] J. Tersoff and D.R. Hamann, *Theory and Application for the Scanning Tunneling Microscope*, Phys. Rev. Lett. **50**, 1998–2001 (1983).
- [43] J. Tersoff and D.R. Hamann, *Theory of the scanning tunneling microscope*, Phys. Rev. B **31**, 805–813 (1985).
- [44] S. Zöphel, J. Repp, G. Meyer, and K.H. Rieder, *Determination of binding sites in ordered phases of CO/Cu(211) employing molecular level manipulation*, Chem. Phys. Lett. **310**, 145–149 (1999).
- [45] J.K. Gimzewski, T.A. Jung, M.T. Cuberes, and R.R. Schlittler, *Scanning tunneling microscopy of individual molecules: beyond imaging*, Surf. Sci. **386**, 101–114 (1997).
- [46] M. Böhrringer, W.-D. Schneider, and R. Berndt, *Corrugation reversal in scanning tunneling microscope images of organic molecules*, Phys. Rev. B **57**, 4081–4087 (1998).
- [47] P. Sautet, *Images of adsorbates with the scanning tunneling microscope: theoretical approaches to the contrast mechanism*, Chem. Rev. **97**, 1097–1116 (1997).
- [48] Stefan Vock, *Modifikation eines Raster-Tunnel-Mikroskops*, Diplomarbeit, Universität Basel (2000).
- [49] S. Hüfner, *Photoelectron Spectroscopy, Springer Series in Solid-State Sciences*, 82, Springer-Verlag, Berlin Heidelberg (1995), ISBN 3–540–19108–9.
- [50] H. Hertz, Ann. Physik **31**, 983 (1887).
- [51] A. Einstein, *Über einen die Erzeugung und Verwandlung von Licht betreffenden heuristischen Gesichtspunkt*, Ann. Physik **17**, 132 (1905).
- [52] C. Berglund and W.E. Spicer, *Photoemission Studies Of Copper + Silver - Theory*, Phys. Rev. A **136**, 1030 (1964).
- [53] M.P. Seah and W.A. Dench, *Quantitative electron spectroscopy of surfaces: a standard data base for electron inelastic mean free paths in solids*, Surf. Interface Ann. **1**, 2–11 (1979).
- [54] Dusanka Naumovic, Ph.D. thesis, Universität Fribourg.
- [55] URL: <http://www.netsci.org/Science/Compchem/feature01.html>.
- [56] R.M. Dreizler and E.K.U. Gross, *Density Functional Theory: An Approach to the Quantum Many-Body Problem*, Springer-Verlag, Berlin (1990), ISBN 3–540–51993–9.
- [57] J.H. Warren, L. Radom, P. Schleyer, and J.A. Pople, *Ab Initio Molecular Orbital Theory*, John Wiley and Sons, New York (1986).
- [58] J. Cioslowski, *Reviews in Computational Chemistry: Ab Initio Calculations on Large Molecules: Methodology and Applications*, VCH Publishers, New York (1993).
- [59] J.J.P. Stewart, *Reviews in Computational Chemistry: Semiempirical Molecular Orbital Methods*, VCH Publishers, New York (1990).
- [60] Stanley Ivan, *Ab-initio density functional calculations on SubPc using the B3LYP exchange-correlation functional at the 6-31Gd level* (2002), personal communication.

- [61] M.J. Frisch, G.W. Trucks, H.B. Schlegel, G.E. Scuseria, M.A. Robb, J.R. Cheeseman, V.G. Zakrzewski, J.A. Montgomery, R.E. Stratmann, J.C. Burant, S. Dapprich, J.M. Millam, A.D. Daniels, K.N. Kudin, M.C. Strain, O. Farkas, J. Tomasi, V. Barone, M. Cossi, R. Cammi, B. Mennucci, C. Pomelli, C. Adamo, S. Clifford, J. Ochterski, G.A. Petersson, P.Y. Ayala, Q. Cui, K. Morokuma, D.K. Malick, A.D. Rabuck, K. Raghavachari, J.B. Foresman, J. Cioslowski, J.V. Ortiz, A.G. Baboul, B.B. Stefanov, G. Liu, A. Liashenko, P. Piskorz, I. Komaromi, R. Gomperts, R.L. Martin, D.J. Fox, T. Keith, M.A. Al-Laham, C.Y. Peng, A. Nanayakkara, C. Gonzalez, M. Challacombe, P.M.W. Gill, B. Johnson, W. Chen, M.W. Wong, J.L. Andres, C. Gonzalez, M. Head-Gordon, E.S. Replogle, and J.A. Pople, *Gaussian 98 Revision A7*, Gaussian Inc., Pittsburgh PA (1998).
- [62] H. Yanagi, D. Schlettwein, H. Nakayama, and T. Nishino, *Site-specific physisorption and chemical reaction of subphthalocyanine molecules on silicon(111)-7x7*, Phys. Rev. B **61**, 1959–1964 (2000).
- [63] V.R. Ferro, L.A. Poveda, R.H. Gonzalez-Jonte, J.M. Garcia de la Vega, T. Torres, and B. del Rey, *Molecular electronic structure of subphthalocyanine macrocycles*, J. Porphyrins Phthalocyanines **4**, 610–619 (2000).
- [64] V.R. Ferro, J.M. Garcia de la Vega, R.H. Gonzalez-Jonte, and L.A. Poveda, *A theoretical study of subphthalocyanine and its nitro- and tertbutyl-derivatives*, J. Mol. Structure **537**, 223–234 (2001).
- [65] G.M. Whitesides, J.P. Mathias, and C.T. Seto, *Molecular self-assembly and nanochemistry: A chemical strategy for the synthesis of nanostructures*, Science **254**, 1312–1319 (1991).
- [66] Nano-7 ECOSS-21, 21th European Conference on Surface Science, 23.-28.6.2002, Malmö (Sweden).
- [67] W.A. Lopes and H.M. Jaeger, *Hierarchical self-assembly of metal nanostructures on diblock copolymer scaffolds*, Nature **414**, 735–738 (2001).
- [68] T. Yokoyama, S. Yokoyama, T. Kamikado, and S. Mashiko, *Selective assembly on surface of supramolecular aggregates with controlled size and shape*, Nature **413**, 619–621 (2001).
- [69] M. Böhrringer, K. Morgenstern, W.-D. Schneider, R. Berndt, F. Mauri, A. De Vita, and R. Car, *Two-dimensional self-assembly of supramolecular clusters and chains*, Phys. Rev. Lett. **83**, 324–327 (1999).
- [70] S. de Feyter, A. Gesquire, M.M. Abdel-Mottaleb, P.C.M. Grim, and F.C. de Schryver, *Scanning Tunneling Microscopy: A Unique Tool in the Study of Chirality, Dynamics, and Reactivity in Physisorbed Organic Monolayers*, Acc. Chem. Res. **33**, 520–531 (2000).
- [71] J.V. Barth, J. Weckesser, C. Cai, Peter Günter, Lukas Bürgi, Olivier Jeandupeux, and Klaus Kern, *Building supramolecular nanostructures at surfaces by hydrogen bonding*, Ang. Chem. Int. Ed. **39**, 1230–1234 (2000).
- [72] J.V. Barth, J. Weckesser, C. Cai, Peter Günter, Lukas Bürgi, Olivier Jeandupeux, and Klaus Kern, *Aufbau supramolekularer Nanostrukturen an Oberflächen über Wasserstoffbrückenbindungen*, Ang. Chem. **112**, 1285–1288 (2000).
- [73] J.E. Lennard-Jones, *Processes of Adsorption and Diffusion on Solid Surfaces*, Trans. Faraday Soc. **28**, 333 (1932).
- [74] R.F.W. Bader, W.H. Henneker, and P.E. Cade, *Molecular Charge Distribution and Chemical Binding*, J. Chem. Phys. **46**, 3341–3363 (1967).
- [75] S. Berner, M. Brunner, L. Ramoino, H. Suzuki, H.-J. Güntherodt, and T.A. Jung, *Time evolution analysis of a 2D solid-gas equilibrium: a model system for molecular adsorption and diffusion*, Chem. Phys. Lett. **348**, 175–181 (2001).
- [76] M. Schunack, T.R. Linderoth, F. Rosei, E. Laegsgaard, I. Stensgaard, and F. Besenbacher, *Long jumps in the surface diffusion of large molecules*, Phys. Rev. Lett. **88**, 156102/1–4 (2002).

Bibliography

- [77] J.L. Atwood, J.E.D. Davies, D.D. Macnicol, and F. Vogtle, *Comprehensive Supramolecular Chemistry*, Pergamon Press, New York (1996).
- [78] G.R. Desiraju, *Supramolecular synthons in crystal engineering-a new organic synthesis*, Ang. Chem. Int. Ed. **34**, 23112327 (1995).
- [79] G. Coates, A. Dunn, A. Henling, D. Dougherty, and R.H. Grubbs, Ang. Chem. Int. Ed. **36**, 248 (1997).
- [80] J.H. Williams, *The Molecular Electric Quadrupole-Moment And Solid-State Architecture*, Acc. Chem. Res. **26**, 593–598 (1993).
- [81] K.W. Hipps, L. Scudiero, D.E. Barlow, and M.P. Cooke Jr., *A Self-Organized 2-Dimensional Bifunctional Structure Formed by Supramolecular Design*, J. Am. Chem. Soc. **124**, 2126–2127 (2002).
- [82] T. Kawai, H. Tanaka, and T. Nakagawa, *Low dimensional self-organization of DNA-base molecules on Cu(111) surfaces*, Surf. Sci. **386**, 124–136 (1997).
- [83] G.G. Roberts, *Langmuir-Blodgett Films*, Plenum Press, New York (1990).
- [84] A. Ulman, *Ultrathin organic films, from Langmuir-Blodgett to Self-Assembly*, Academic Press Inc., San Diego (1991), ISBN 0–12–708230–1.
- [85] D.Y. Takamoto, E. Aydil, J.A. Zasadzinski, A.T. Ivanova, D.K. Schwartz, T.L. Yang, and P.S. Cremer, *Stable Ordering in Langmuir-Blodgett Films*, Science **293**, 1292–1295 (2001).
- [86] A. Ulman, *Formation and structure of self-assembled monolayers*, Chem. Rev. **96**, 1533–1554 (1996).
- [87] L.S. Pinheiro and M.L.A. Temperini, *Coadsorption of 2-mercaptopyrimidine and 1,10'-phenanthroline on Au(111) as seen by STM*, Surf. Sci. **441**, 53–64 (1999).
- [88] D.F. Ogletree, M.A. Van Hove, and G.A. Somorjai, *Benzene and Carbon Monoxide adsorbed on Pt(111): A LEED intensity analysis*, Surf. Sci. **183**, 1–20 (1987).
- [89] P.A. Heimann, P. Jakob, T. Pache, H.-P. Steinrück, and D. Menzel, *Benzene coadsorbed with CO and NO on Ru(001): A UPS study with synchrotron radiation*, Surf. Sci. **210**, 282–300 (1988).
- [90] H. Ohtani, R.J. Wilson, S. Chiang, and C.M. Mate, *Scanning Tunneling Microscopy Observations of Benzene Molecules on the Rh(111)-(3x3) (C₆H₆ + 2CO) Surface*, Phys. Rev. Lett. **60**, 2398–2401 (1988).
- [91] P. Zebisch, W. Huber, and H.P. Steinrück, *On the formation of mixed ordered structures in the coadsorption system benzene + NO on Ni(111)*, Surf. Sci. **258**, 1–15 (1991).
- [92] H.A. Yoon, M. Salmeron, and G.A. Somorjai, *Scanning tunneling microscopy (STM) study of benzene and its coadsorption with carbon monoxide on Rh(111)*, Surf. Sci. **373**, 300–306 (1996).
- [93] M. Stichler, R. Weimar, and D. Menzel, *The influence of electronegative coadsorbates on the geometry of benzene on Ru(001)*, Surf. Sci. **384**, 179–191 (1997).
- [94] M.A. Van Hove and G.A. Somorjai, *Selected molecular surface structures determined by modern low-energy electron diffraction*, J. Mat. Chem. **131**, 243–257 (1998).
- [95] C.M. Mate and G. A. Somorjai, *Carbon monoxide induced ordering of benzene on Pt(111) and Rh(111) crystal surfaces*, Surf. Sci. **160**, 542–560 (1985).
- [96] T. Sasaki, T. Aruga, H. Kuroda, and Y. Iwasawa, *Interaction between CO and NH₃ coadsorbed on Ru(001): its effects on the ordering in mixed adlayers and the ammonia dissociation*, Surf. Sci. **240**, 223–244 (1990).

- [97] G.S. Blackman, C.T. Kao, B.E. Bent, C.M. Mate, M.A. van Hove, and G.A. Somorjai, *LEED and RHEELS studies of the coadsorbed CO + Ethylidyne and NO + Ethylidyne systems on the Rh(111) crystal surface*, Surf. Sci. **207**, 66–88 (1988).
- [98] B.L. Kropman, D.H.A. Blank, and H. Rogalla, *Binary Mixtures of Self-Assembled Monolayers on SrTiO₃: Experimental Evidence for Phase Segregation*, Langmuir **16**, 1469–1472 (2000).
- [99] T. Takami, E. Delamarche, and B. Michel, *Recognition of individual tail groups in self-assembled monolayers*, Langmuir **11**, 3876–3881 (1995).
- [100] E. Meyer, R. Overney, R. Lüthi, D. Brodbeck, L. Howald, J. Frommer, H.-J. Güntherodt, O. Wolter, M. Fujihira, H. Takano, and Y. Gotoh, *Friction force microscopy of mixed Langmuir-Blodgett films*, Thin Solid Films **220**, 132–137 (1992).
- [101] A. Meller and A. Ossko, *Phthalocyaninartige Bor-Komplexe*, Monatshefte f. Chemie **103**, 150–155 (1972).
- [102] C.G. Claessens, D. Gonzalez-Rodriguez, and T. Torres, *Subphthalocyanines: Singular Aromatic Compounds—Synthesis, Reactivity, and Physical Properties*, Chem. Rev. **102**, 835–853 (2002).
- [103] H. Kietai, *Crystal And Molecular-Structure Of A New Phthalocyanine-Like Boron Complex*, Monatshefte f. Chemie **105**, 405–418 (1974).
- [104] B. del Rey, U. Keller, T. Torres, G. Rojo, F. Agullo-Lopez, S. Nonell, C. Marti, S. Brasselet, Y. Ledoux, and J. Zyss, *Synthesis and nonlinear optical, photophysical, and electrochemical properties of subphthalocyanines*, J. Am. Chem. Soc. **120**, 12808–12817 (1998).
- [105] J. Rauschnabel and M. Hanack, *New Derivatives And Homologs Of Subphthalocyanine*, Tetrahedron Lett. **36**, 1629–1632 (1995).
- [106] Brit. UK Pat. Appl. GB 2,290,489, 1996. P. Hunt (Imperial Chemical Industries PLC, UK).
- [107] H.W. Kroto, J.R. Heath, S.C. O'Brian, R.F. Curl, and R.E. Smalley, *C₆₀: Buckminsterfullerene*, Nature **318**, 162–163 (1985).
- [108] W. Kratschmer, L.D. Lamb, K. Fostiropoulos, and D. Huffman, *Solid C₆₀: a new form of carbon*, Nature **347**, 354–358 (1990).
- [109] J.K. Gimzewski, S. Modesti, and R. Schlittler, *Cooperative self-assembly of Au atoms and C₆₀ on Au(110) surfaces*, Phys. Rev. Lett. **72**, 1036–1039 (1994).
- [110] S. Modesti, S. Cerasari, and P. Rudolf, *Determination of charge states of C₆₀ adsorbed on metal surfaces*, Phys. Rev. Lett. **71**, 2469–2472 (1993).
- [111] M. Kosaka, K. Tanigaki, T.W. Ebbesen, Y. Nakahara, and K. Tateishi, *Electronic states studies of alkali-metal-doped C₆₀ superconductors by nuclear magnetic resonance*, Appl. Phys. Lett. **63**, 2561–2563 (1993).
- [112] E.I. Altman and R.J. Colton, *Determination of the orientation of C₆₀ adsorbed on Au(111) and Ag(111)*, Phys. Rev. B **48**, 18244–18249 (1993).
- [113] B. Kessler, *Phthalocyanine-C₆₀ composites as improved photoreceptor materials?*, Appl. Phys. A **67**, 125–133 (1998).
- [114] E.I. Altman and R.J. Colton, *Nucleation, growth, and structure of fullerene films on Au(111)*, Surf. Sci. **279**, 49–67 (1992).
- [115] A. Fartash, *Orientational epitaxy of high-quality C₆₀ films on Ag(111)*, Phys. Rev. B **52**, 7883–7886 (1995).

Bibliography

- [116] T. Sakurai, X.-D. Wang, Q.K. Xue, Y. Hasegawa, T. Hashizume, and H. Shinohara, *Scanning tunneling microscopy study of fullerenes*, Progress in Surface Science **51**, 263–408 (1996).
- [117] E. Giudice, E. Magnano, S. Rusponi, C. Boragno, and U. Valbusa, *Morphology of C₆₀ thin films on Ag(100)*, Surf. Sci. **405**, L561–L565 (1998).
- [118] M.K.J. Johansson, A.J. Maxwell, S.M. Gray, P.A. Bruhwiler, and L.S.O. Johansson, *Adsorption of C₆₀ on Al(111) studied with scanning tunnelling microscopy*, Surf. Sci. **397**, 314–321 (1998).
- [119] A. Kühnle, T.R. Linderoth, B. Hammer, and Flemming Besenbacher, *Chiral recognition in dimerization of adsorbed cysteine observed by scanning tunnelling microscopy*, Nature **415**, 891–893 (2002).
- [120] V. Humblot, S. Haq, C. Muryn, W.A. Hofer, and R. Raval, *From Local Adsorption Stresses to Chiral Surfaces: (R,R)-Tartaric Acid on Ni(110)*, J. Am. Chem. Soc. **124**, 503–510 (2002).
- [121] M. Ortega Lorenzo, C. J. Baddeley, C. Muryn, and R. Raval, *Extended surface chirality from supramolecular assemblies of adsorbed chiral molecules*, Nature **404**, 376–379 (2000).
- [122] Conference Proceedings, Rasmita Raval, Thursday, June 27 2002, TH-B-015, Nano-7 ECOSS-21, 21th European Conference on Surface Science, 23.-28.6.2002, Malmö (Sweden).
- [123] Linear or hexagonal phases in single-component ad-layers of Xe on Pt(111) can be selected by coverage, temperature. For observations by He scattering see K. Kern, and G. Comsa, *Helium-scattering studies of the dynamics and phase transitions of surfaces*, Adv. in Chem. Phys. **76**, 211–280 (1989).
- [124] S. Berner, M. de Wild, L. Ramoino, H. Suzuki, H. Yanagi, D. Schlettwein, S. Ivan, A. Baratoff, H.-J. Güntherodt, and T.A. Jung, *to be published*.
- [125] M. de Wild, S. Berner, H. Suzuki, H. Yanagi, D. Schlettwein, S. Ivan, A. Baratoff, H.-J. Güntherodt, and T.A. Jung, *A Novel Route To Molecular Self-Assembly: Self-Intermixed Monolayer Phases*, ChemPhysChem **10**, accepted (2002).
- [126] Ph. Lambin, A.A. Lucas, and J.-P. Vigneron, *Polarization waves and Van der Waals cohesion of C₆₀ fullerite*, Phys. Rev. B **46**, 1794–1803 (1992).
- [127] L.H. Tjeng, R. Hesper, A.C.L. Heessels, A. Heeres, H.T. Jonkman, and G.A. Sawatzky, *Development of the electronic structure in K-doped C₆₀ monolayer on a Ag(111) surface*, Solid State Communications **103**, 31–35 (1997).
- [128] Y. Kuk, D.K. Kim, Y.D. Suh, K.H. Park, H.P. Noh, S.J. Oh, and S.K. Kim, *Stressed C₆₀ Layers on Au(001)*, Phys. Rev. Lett. **70**, 1948–1951 (1993).
- [129] M. Pedio, K. Hevesi, N. Zema, M. Capozzi, P. Perfetti, R. Gouttebaron, J.J. Pireaux, R. Caudano, and P. Rudolf, *C₆₀/metal surfaces: adsorption and decomposition*, Surf. Sci. **437**, 249–260 (1999).
- [130] J.P. Lu, X.P. Li, and R.M. Martin, *Ground state and phase transitions in solid C₆₀*, Phys. Rev. Lett. **68**, 1551–1554 (1992).
- [131] J.G. Hou, Y. Jinlong, W. Haiqian, L. Qunxiang, Z. Changan, Y. Lanfeng, W. Bing, D.M. Chen, and Z. Qingshi, *Topology of two-dimensional C₆₀ domains*, Nature **409**, 304–305 (2001).
- [132] URL: http://riesling.chem.umn.edu/~hu/line_resp.html.
- [133] E. Wimmer, C.L. Fu, and A.J. Freeman, *Catalytic Promoting and Poisoning: All-Electron Local-Density-Functional Theory of CO on Ni(001) Surfaces Coadsorbed with K or S*, Phys. Rev. Lett. **55**, 2618–2621 (1985).
- [134] E. Ruckenstein and T. Halachev, *Interactions between coadsorbed species on the Rh(111) surface as a function of the separation distance between them*, Surf. Sci. **122**, 422–432 (1982).

- [135] T.L. Einstein, *Theory of indirect interaction between chemisorbed atoms*, CRC-Critical-Reviews-in-Solid-State-and-Materials-Sciences **7**, 261–288 (1978).
- [136] K.H. Lau and W. Kohn, *Indirect long-range oscillatory interaction between adsorbed atoms*, Surf. Sci. **75**, 69–85 (1978).
- [137] J. Li, W-D. Schneider, and R. Berndt, *Local density of states from spectroscopic scanning-tunneling-microscope images: Ag(111)*, Phys. Rev. B **56**, 7656–7659 (1997).
- [138] D. Kolthoff and H. Pfnür, *Geometrical evidence for long-range coupling in strongly anisotropic adsorbate systems: Sr and Li on Mo(211)*, Surf. Sci. **459**, 256–276 (2000).
- [139] Jacob N. Israelachvili, *Intermolecular And Surface Forces*, Academic Press, London (1991), ISBN 0-12-375181-0.
- [140] T.A. Jung, R.R. Schlittler, and J.K. Gimzewski, *Conformational identification of individual adsorbed molecules with the STM*, Nature **386**, 696–698 (1997).
- [141] R. Hesper, L.H. Tjeng, and G.A. Sawatzky, *Strongly reduced band gap in a correlated insulator in close proximity to a metal*, Europhys. Lett. **40**, 177–182 (1997).
- [142] M.R.C. Hunt, P. Rudolf, and S. Modesti, *Localization of substrate-induced modification in the electronic structure of C₆₀ at fullerene-metal interfaces*, Phys. Rev. B **55**, 7882–7888 (1997).
- [143] G.K. Wertheim and D.N.E. Buchanan, *Interfacial reaction of C₆₀ with silver*, Phys. Rev. B **50**, 11070–11073 (1994).
- [144] C.T. Tzeng, W.S. Lo, J.Y. Yuh, R.Y. Chu, and K.D. Tsuei, *Photoemission, near edge x-ray-adsorption spectroscopy, and low-energy electron diffraction study of C₆₀ on Au(111) surfaces*, Phys. Rev. B **61**, 2263–2272 (2000).
- [145] J. H. Weaver, J.L. Martins, T. Komeda, Y. Chen, T. R. Ohno, G. H. Kroll, N. Troullier, R. E. Haufler, and R. E. Smalley, *Electronic structure of solid C₆₀: Experiment and theory*, Phys. Rev. Lett. **66**, 1741–1744 (1991).
- [146] A.J. Maxwell, P.A. Brühwiler, D. Arvanitis, J. Hasselström, M.K.J. Johansson, and N. Martensson, *Electronic and geometric structure of C₆₀ on Al(111) and Al(110)*, Phys. Rev. B **57**, 7312–7326 (1998).
- [147] E. Magnano, S. Vandr e, C. Cepek, A. Goldini, A.D. Laine, G.M. Curr o, A. Santinello, and M. Sancrotti, *Substrate-adlayer interaction at the C₆₀/Ag(110) interface studied by high-resolution synchrotron radiation*, Surf. Sci. **377** (1997).
- [148] P.W. Wagner, W.M. Riggs, L.E. Davis, J.F. Moulder, and G.E. Muilenberg, *Handbook of X-ray Photoelectron Spectroscopy*, Perkin-Elmer Corporation, Eden Prairie, Minnesota (1979).
- [149] P.J. Benning, D.M. Poirier, N. Troullier, J.L. Martins, J.H. Weaver, R.E. Haufler, L.P.F. Chibante, and R.E. Smalley, *Electronic states of solid C₆₀: symmetries and photoionization cross sections*, Phys. Rev. B **44**, 1962–1965 (1991).
- [150] R.C. Haddon, L.E. Brus, and K. Raghvachari, *Electronic structure and bonding in icosahedral C₆₀*, Chem. Phys. Lett. **125**, 459–464 (1985).
- [151] S.J. Chase, W.S. Basca, M.G. Mitch, L.J. Pilione, and J.S. Lannin, *Surface enhanced Raman scattering and photoemission of C₆₀ on noble-metal surfaces*, Phys. Rev. B **46**, 7873–7877 (1992).
- [152] F.S. Tautz, M. Eremtchenko, J.A. Schaefer, M. Sokolowski, V. Shklover, K. Gloeckler, and E. Umbach, *A comparison of the chemisorption behaviour of PTCDA on different Ag surfaces*, Surf. Sci. **502**, 176–184 (2002).

Bibliography

- [153] Prof. Dr.-Ing. G. Brunner, *Skriptum zur Vorlesung Thermodynamik III*, Technische Universität, Arbeitsbereich Verfahrenstechnik, Hamburg-Harburg (2001).
- [154] Prof. Dr.-Ing. K. Schaber, *Skriptum Chemische Thermodynamik*, Institut für Technische Thermodynamik und Kältetechnik der Universität Karlsruhe, Wintersemester, Karlsruhe (2001).
- [155] Le Chatelier, *Recherches experimentales et theoretiques sur les equilibres chimiques*, Paris (1888).
- [156] Klaus Stierstadt, *Physik der Materie*, VCH, D-6940 Weinheim (1989), ISBN 3-527-26921-5.
- [157] Richard Becker, *Theorie der Wärme*, Springer, Berlin (1978), ISBN 3-540-08988-8.
- [158] John A. Venables, *Introduction to Surface and Thin Film Processes*, Cambridge University Press, The Edinburgh Building, Cambridge CB2 2RU, UK (2000), ISBN 0-521-62460-6.
- [159] D.A. Neumann, J.R.D. Copley, R.L. Cappelletti, W.A. Kamitakahara, R.M. Lindstrom, K.M. Creegan, D.M. Cox, W.J. Romanow, N. Coustel, J.P.Jr. McCauley, N.C. Maliszewskyj, J.E. Fischer, and A.B. Smith, *Coherent quasielastic neutron scattering study of the rotational dynamics of C₆₀ in the orientationally disordered phase*, Phys. Rev. Lett. **67**, 3808–3811 (1991).
- [160] C. Cepek, M. Sancrotti, T. Greber, and J. Osterwalder, *Electronic structure of K doped C₆₀ monolayers on Ag(001)*, Surf. Sci. **454** (2000).
- [161] J.A. Venables, G. Spiller, and M. Hanbücken, *Nucleation and growth of thin films*, Rep. Prog. Phys. **47**, 399–459 (1984).
- [162] E. Umbach, K. Glöckler, and M. Sokolowski, *Surface architecture with large organic molecules: interface order and epitaxy*, Surf. Sci. **402**, 20–31 (1998).
- [163] P. Fenter, P. Eisenberger, P. Burrows, S.R. Forrest, and K.S. Liang, *Epitaxy at the organic-inorganic interface*, Physica B **221**, 145–151 (1996).
- [164] Molecules and molecular data provided by: Christian Galka, Arbeitsgruppe Prof. Lutz Gade, Institut für Anorganische, Chemie der Universität Würzburg, Am Hubland, D-97074 Würzburg, Deutschland. Personal communication.
- [165] J. Taborski, *NEXAFS investigations on ordered adsorbate layers of large aromatic molecules*, J. Electr. Rel. Phen. **75**, 129–147 (1995).
- [166] M. Brunner, S. Berner, H. Suzuki, and T.A. Jung, *Production method for atomic and molecular patterns on surfaces and nanostructured devices*, EU Patent Application (2001).
- [167] W. Geyer, V. Stadler, A. Küller, B. Völkel, W. Eck, A. Gölzhäuser, M. Grunze, T. Weimann, and K. Edinger, *Chemische Nanostrukturierung von Oberflächen*, DPG conference 2002 Regensburg, Poster CPP 15.4 .
- [168] M. Nunez-Regueiro, L. Marques, J.-L. Hodeau, O. Bethoux, and M. Perroux, *Polymerized Fullerite Structures*, Phys. Rev. Lett. **74**, 278–281 (1995).
- [169] P.M. Ajayan, V. Ravikumar, and J.-C. Charlier, *Surface Reconstructions and Dimensional Changes in Single-Walled Carbon Nanotubes*, Phys. Rev. Lett. **81**, 1437–1440 (1998).
- [170] R. Bennewitz, J.N. Crain, A. Kirakosian, J.-L. Lin, J.L. McChesney, D.Y. Petrovykh, and F.J. Himpsel, *Atomic scale memory at a silicon surface*, Nanotechnology **13**, 499 (2002).
- [171] J.S. Foster, J.E. Frommer, and P.C. Arnett, *Molecular manipulation using a tunneling microscope*, Nature **331**, 324–326 (1988).
- [172] P.H. Beton, A. Dunn, and P. Moriarty, *Manipulation Of C-60 Molecules On A Si Surface*, Appl. Phys. Lett. **67**, 1075–1077 (1995).

- [173] M.T. Cuberes, R.R. Schlittler, and J.K. Gimzewski, *Room temperature supramolecular repositioning at molecular interfaces using a scanning tunneling microscope*, Surf. Sci. **371**, 231–234 (1997).
- [174] T.A. Jung, R.R. Schlittler, J.K. Gimzewski, H. Tang, and C. Joachim, *Controlled room-temperature positioning of individual molecules: Molecular flexure and motion*, Science **271**, 181–184 (1996).
- [175] M. Böhrringer, R. Berndt, and W.-D. Schneider, *Scanning tunneling microscope-induced molecular motion and its effect on the image formation*, Surf. Sci. **408**, 72–85 (1998).
- [176] F. Moresco, G. Meyer, K.-H. Rieder, H. Tang, A. Goudron, and C. Joachim, *Recording Intramolecular Mechanics during the Manipulation of a Large Molecule*, Phys. Rev. Lett. **87**, 88302–1–88302–4 (2001).
- [177] D.M. Eigler and E.K. Schweizer, *Positioning single atoms with a scanning tunneling microscope*, Nature **344**, 524–526 (1990).
- [178] J.A. Stroscio and D.M. Eigler, *Atomic and molecular manipulation with the scanning tunneling microscope*, Science **254**, 319–326 (1991).
- [179] P. Vettiger, M. Despont, U. Drechsler, U. Dürig, W. Häberle, M.I. Lutwyche, H.E. Rothuizen, R. Stutz, R. Widmer, and G.K. Binnig, *The “Millipede”—more than one thousand tips for future AFM data storage*, IBM Journal of Research and Development **44**, 323–340 (2000).
- [180] J.K. Gimzewski and C. Joachim, *Nanoscale Science of Single Molecules Using Local Probes*, Science **283**, 1683–1688 (1999).
- [181] Z.J. Donhauser, B.A. Mantooth, K.F. Kelly, L.A. Bumm, J.D. Monnell, J.J. Stapleton, D.W. Price, A.M. Rawlett, D.L. Allara, J.M. Tour, and P.S. Weiss, *Conductance Switching in Single Molecules Through Conformational Changes*, Science **292**, 2303–2307 (2001).
- [182] J.K. Gimzewski, E. Stoll, and R.R. Schlittler, *Scanning tunneling microscopy of individual molecules of Copper Phthalocyanine adsorbed on polycrystalline silver surfaces*, Surf. Sci. **181**, 267–277 (1987).
- [183] P.H. Lippel, R.J. Wilson, M.D. Miller, C. Wöll, and S. Chiang, *High-resolution imaging of Copper-Phthalocyanine by scanning tunneling microscopy*, Phys. Rev. Lett. **62**, 171–174 (1989).
- [184] F. Rosei, M. Schunack, P. Jiang, A. Gourdon, E. Laegsgaard, I. Stensgaard, C. Joachim, and F. Besenbacher, *Organic molecules acting as templates on metal surfaces*, Science **296**, 328–331 (2002).
- [185] K.M. Smith, *Porphyrins and Metalloporphyrins*, Elsevier, New York (1975).
- [186] M.F. Perutz, H.C. Watson, H. Muirhead, R. Diamond R, and W. Bolton, *structure of haemoglobin - X-ray examination of reduced horse haemoglobin*, Nature **203**, 687 (1964).
- [187] K. Wüthrich, *The way to NMR structures of proteins*, Nature Structural Biology **8**, 923–925 (2001).
- [188] P. Basu, N.V. Shokhirev, J.H. Enemark, and F.A. Walker, *NMR-Studies Of Hindered Ligand Rotation, Magnetic-Anisotropy, Curie Behavior, Proton Spin Relaxation, And Ligand-Exchange In Some Novel Oxomolybdenum(V) Iron(III) Porphyrinate Complexes*, J. Am. Chem. Soc. **117**, 9042–9055 (1995).
- [189] E.F. Ullman L.K. Gottwald, *Biphenyl-Type Atropisomerism As A Probe For Conformational Rigidity Of Alpha, Beta, Gamma, Delta-Tetraarylporphines*, Tetrahedron Letters **36**, 3071–3074 (1969).
- [190] Takashi Yokoyama, Shiyoshi Yokoyama, Toshiya Kamikado, and Shinro Mashiko, *Nonplanar adsorption and orientational ordering of porphyrin molecules on Au(111)*, J. Chem. Phys. **115**, 3814–3818 (2001).
- [191] F. Moresco, G. Meyer, K.-H. Rieder, H. Tang, A. Goudron, and C. Joachim, *Conformational Changes of Single Molecules Induced by STM*, Phys. Rev. Lett. **86**, 672–675 (2001).

Bibliography

- [192] Ch. Loppacher, M. Bammerlin, M. Guggisberg, E. Meyer, H.-J. Güntherodt, R. Schlittler, and J.K. Gimzewski, *Forces with submolecular resolution between the probing tip and Cu-TBPP molecules on Cu(100) observed with a combined AFM/STM*, Appl. Phys. A **72**, 105–108 (2001).
- [193] Christian Loppacher, *Nichtkontakt-Rasterkraftmikroskopie mit digitalem Phasenregelkreis*, Ph.D. thesis, Universität Basel, IfP, CH-4056 Basel (2000).
- [194] F. Moresco, G. Meyer, K.-H. Rieder, J. Ping, H. Tang, and C. Joachim, *TBPP molecules on copper surfaces: a low temperature scanning tunneling microscope investigation*, Surf. Sci. **499**, 94–102 (2002).
- [195] T. Sakurai and Y. Watanabe (Eds.), *Advances in Scanning Probe Microscopy*, Springer, Tokyo (1999), ISBN 3-540-66718-0.
- [196] POV-RayTM for Windows, Version 3.5.icl.win32, copyrighted freeware, Copyright 1991-2002 by The Persistence of Vision Development Team. URL: <http://www.povray.org/>.
- [197] *Molecular Layered medium used in integrated circuits and computer storage devices*. U.S. Patent, Feb. 29 2000 6,031,756. J.K. Gimzewski, T.A. Jung and R.R. Schlittler.
- [198] C.P. Collier, G. Mattersteig, E.W. Wong, L. Yi, K. Berberly, J. Sampaio, F.M. Raymo, J.F. Stoddart, and J.R. Heath, *A [2]catenane-based solid state electronically reconfigurable switch*, Science **289**, 1172–1175 (2000).
- [199] Yi Luo, C. Patrick Collier, Jan O. Jeppesen, Kent A. Nielsen, Erica De Ionno, Greg Ho, Julie Perkins, Hsian-Rong Tseng, Tohru Yamamoto, J. Fraser Stoddart, and James R. Heath, *Two-dimensional molecular electronics circuits*, ChemPhysChem **3**, 467 (2002).
- [200] C. Joachim and J.K. Gimzewski, *An electromechanical amplifier using a single molecule*, Chem. Phys. Lett. **265**, 353–357 (1996).
- [201] C. Joachim, J.K. Gimzewski, and H. Tang, *Physical principles of the single-C₆₀ transistor effect*, Phys. Rev. B **58**, 16407–16417 (1998).
- [202] D.T. Gryko, Chr. Clausen, K.M. Roth, N. Dontha, D.F. Bocian, W.G. Kuhr, and J.S. Lindsay, *Synthesis of Porphyrin-Linker-Thiol Molecules with Diverse Linkers for Studies of Molecular-Based Information Storage*, J. Org. Chem. **65**, 7345–7355 (2000).
- [203] X.D. Cui, A. Primak, X. Zarate, J. Tomfohr, O.F. Sankey, A.L. Moore, T.A. Moore, D. Gust, G. Harris, and S.M. Lindsay, *Reproducible Measurement of Single-Molecule Conductivity*, Science **294**, 571–574 (2001).

List of Figures

1.1.	The number of transistors integrated into Integrated Circuits is growing exponentially since the seventies following the prediction of Gordon Moore in 1968. For its continuity, however, new technologies might be needed. Data from [26].	2
2.1.	The Nanolab: top view of the UHV system comprising the STM-, ESCA-, MBE-, LEED-, Evap- and OMBE-chamber. (Technical drawing by A. Heuri)	5
2.2.	3D model of the Nanolab exposing the manifold features of the system. (Technical drawing by A. Heuri)	6
2.3.	Sphere model of a face-centered cubic single crystal with surfaces oriented (100), (110), and (111), each with specific symmetry and corrugation. From [34]. 7	
2.4.	Schematic energy diagram for the tunneling process from the tip to the unoccupied states of the sample. The two conductors are separated by the distance d , and the positive bias voltage V_{bias} is applied to the sample. The DOS of the tip and the sample are indicated as ρ_t , ρ_s , respectively. The size of the arrows in the tunneling gap represents the tunneling probability, described by the tunneling matrix element.	9
2.5.	Principle operation of the STM. (Schematic: distances and sizes are not to scale.) The tunneling current I_T which flows between the tip and the atomically flat and conducting sample when a constant bias voltage V_{bias} is applied, decays exponentially with the tip-sample separation. The tip motion in the scans with constant current mode, controlled by a feedback loop and piezoelectric elements, is indicated over a surface step.	10
2.6.	Principle of Photoelectron Spectroscopy. The irradiated matter emits electrons with kinetic energy E_K if the photon energy $h\nu > E_B + \phi$ and is thereby mapping the occupied energy levels of the solid.	11
3.1.	Structure of Chloro[subphthalocyaninato]boron(III) (SubPc). Colors specify different elements: C, dark gray; Cl, green; H, white; N, blue; B, pink, hidden by the Cl. The height is approximately 0.5 nm, the diameter ca. 1.3 nm. . . .	16
3.2.	SubPc adsorbed on Ag(111). A single molecule is marked by a circle. The three sub-units of a molecule represent the phenyl-rings [62]. Scan range 21 nm x 9 nm. $V_{bias} = 2$ V, $I_t = 200$ pA.	17
3.3.	A monolayer of SubPc on Ag(111): The molecules are arranged in a hexagonal honey-comb pattern [75]. Scan range 56 nm x 56 nm. $V_{bias} = 1.3$ V, $I_t = 200$ pA.	17

List of Figures

3.4.	Structure of C ₆₀ . The diameter of the carbon cage is approximately 7 Å.	17
3.5.	Self-intermixed monolayer on Ag(111) and its molecular components. Artificially colored Scanning Tunneling Microscopy image of the basic unit of the molecular <i>stripe</i> pattern with superimposed schematic contours (SubPc green, C ₆₀ yellow). Individual components can be identified by size and shape. Scan range 4.3 nm x 3.2 nm. $V_{bias} = 1.3$ V, $I_t = 20$ pA.	19
3.6.	Self-intermixed monolayer on Ag(111): Artificially colored STM image of a monolayer of co-adsorbed SubPc and C ₆₀ on Ag(111) (imaged area, 17 nm x 25 nm, $V_{bias} = 1.3$ V, $I_t = 20$ pA). The self-intermixed <i>stripe</i> phase is shown on the right with alternating C ₆₀ chains (yellow) and SubPc rows (green). The bare substrate areas appear dark. The distance between adjacent parallel C ₆₀ rows is 3.3 nm. Up to 38 parallel stripes with a length of 100 nm have been observed. The monoclinic unit cell of $p2$ symmetry contains three C ₆₀ and two SubPc molecules. One C ₆₀ molecule, colored in red near the top edge of the C ₆₀ island, jumped to an adjacent site between two horizontal scans. A pure C ₆₀ island coexists on the left hand side.	20
3.7.	Proposed model for the registry of the <i>stripe</i> phase on Ag(111). The positions and the orientations of the C ₆₀ and SubPc molecules are depicted on the atomic silver lattice.	22
3.8.	a) Rotational and b) translational domain shifts of the <i>stripe</i> phase in accordance with the hexagonal (111) substrate (60° in a), resp. 1.7 nm in b) which means a shift by 6 Ag sites). Scan range a) 56 nm x 48 nm, b) 23 nm x 21 nm.	22
3.9.	Mesoscopic chirality segregation into λ and ρ domains of the <i>stripe</i> pattern: Enantiomorph supramolecular structures are formed by a chiral packing of achiral molecules. The scan ranges are approximately 10 nm x 10 nm. In both scans $V_{bias} \approx 1.3$ V, $I_t \approx 20$ pA.	23
3.10.	Self-Intermixed Monolayer Phases (SIMPs): coexisting <i>star</i> and <i>stripe</i> patterns. This STM image shows two different SIMPs of SubPc and C ₆₀ on Ag(111) (imaged area, 34 nm x 34 nm, $V_{bias} = 1.9$ V, $I_t = 20$ pA). On the right hand side, the 3:2- <i>stripe</i> SIMP (I) and on the left hand side, the hexagonal 1:1- <i>star</i> SIMP (II) is observed. Point defects are marked by arrows (top right: a vacancy defect is interrupting a C ₆₀ row; left: a center hole is filled with a molecule). Apparently random tip excursions of single molecular height (III) are visible between the two ordered regions and are identified as mobile molecules in a 2D gas phase [75].	24
3.11.	STM image of a hexagonal cell in the <i>star</i> SIMP, with superimposed schematic shapes. A C ₆₀ triplet is surrounded by three SubPc molecules. Through a vacancy in the center, the level of the Ag substrate is imaged. Scan range 11.5 nm x 11.5 nm, $V_{bias} = 1.9$ V, $I_t = 20$ pA.	25
3.12.	With a good STM tip, the intramolecular structure of the SubPc molecules can be resolved and their orientation within the pattern is unravelled. Scan range 17 nm x 12 nm, $V_{bias} = 1.9$ V, $I_t = 20$ pA.	25

3.13. Proposed model for the registry of the <i>star</i> phase on Ag(111). The center hole is large enough to offer space for an additional molecule (see left arrow in figure 3.10).	26
3.14. Molecular gas-phase: between the two well-ordered SIMPs, random tip excursions can be seen due to mobile molecules (top part). Scan range 27 nm x 15 nm, $V_{bias} = 1.9$ V, $I_t = 20$ pA (section from fig. 3.10). The line-scan (“height-profile”, lower part) makes clear that the same objects can be found in the condensed phases and in the gas phase. The motion of the molecules in the gas-phase during the scanning-process, however, inhibits any correlation of the successive scan-lines.	27
3.15. Schematic room-temperature “phase-diagram” of SubPc and C ₆₀ with corresponding STM images of self- intermixed monolayers (imaged area, 13 nm x 13 nm, 1.0 V < V_{bias} < 1.9 V, 20 pA < I_t < 100 pA, C ₆₀ blue, SubPc green). Left column: pure SIMPs displayed against the ratio SubPc:C ₆₀ : 1:0, honey-comb phase of pure SubPc; 1:1, self-intermixed monolayer <i>star</i> phase; 2:3, self-intermixed monolayer <i>stripe</i> phase; 0:1, hexagonal phase of pure C ₆₀ . Right column: Coexisting phases in equilibrium with molecular 2D gas for ratios SubPc:C ₆₀ which are between the above-mentioned values.	29
3.16. “Snapshot” of the transition from pure SubPc honey-comb pattern to an intermixed phase. The C ₆₀ molecules inter-diffuse and form “channels”, where two C ₆₀ molecules replace one SubPc. Scan range 19 nm x 17 nm. $V_{bias} = 2$ V, $I_t = 15$ pA. This STM image is slightly filtered with a median filter.	30
4.1. LUMO of C ₆₀ [132].	32
4.2. Relaxed geometry and effective atomic charges (Mulliken population analysis) from a density functional computation on a single free SubPc molecule [125]. For the identification of atomic species, the color-code of figure 3.1 is used. The distribution of delocalized electronic states and partial charges determines the intermolecular and molecule-substrate interactions which presumably leads to the observed ordering as discussed in the text.	33
4.3. Electrostatic potential of the free SubPc molecule mapped onto the electron density surface [60]. Excess of electrons at the Cl in the center are colored <i>red</i> (negative electrostatic potential), more positively charged portion at the peripheral phenyl-rings <i>blue</i> (positive potential). This electron distribution is responsible for the axial dipole moment [60] and for the molecular interactions.	33
4.4. Summary of the forces in SIMPs: molecule-substrate and molecule-molecule interactions for both components separately and the mixed phase are shown. Attractive contributions are in <i>blue</i> , repulsive contributions in <i>red</i>	35
4.5. Apparent height of C ₆₀ molecules in different phases, imaged at 1.9 V bias voltage V_{bias} . The variations are assumed to arise from different local environments modified by the SubPc molecules.	37

List of Figures

4.6. STM image of a *stripe* island recorded at the different bias voltage V_{bias} , indicated on the left side. The tunneling current I_t was kept constant at 20 pA. At low V_{bias} , only the C_{60} molecules remain visible. Due to the specific electronic structure of the molecules, the appearance of the pattern strongly depend on V_{bias} . Scan range 34 nm x 51 nm. 38

4.7. The ratio of the apparent heights of C_{60} and SubPc is shown as a function of the applied bias voltage V_{bias} . The tunneling current I_t was kept constant at 20 pA. At elevated V_{bias} , the apparent heights of both molecules becomes the same, whereas at lower bias voltage, the C_{60} dominate because their LUMO is partly occupied owing to a charge transfer from the substrate. The SubPc molecules are hardly visible at low V_{bias} , which is consistent with observations on pure SubPc films [33]. 39

4.8. Comparison of the coverage measurement by the microbalance and by XPS. Both methods correlate well. 40

4.9. The C1s peak of the C_{60} film shifts as a function of the coverage. The chemical shift, compared to bulk fullerenes, where the C1s peak shows up at 285.3 eV, points toward an ionic character of the adlayer–substrate interaction [113, 147]. 41

4.10. XPS spectra of the C1s peak of pure C_{60} , pure SubPc and a two-component film on Ag(111) measured with Mg- K_{α} excitation. A chemical shift can be observed for the C–C and C–N carbon compound peaks of the SubPc film. The two different chemical environments of the carbon atoms in SubPc also lead to the asymmetry in the main peak of the mixed film. In all phases, however, the C–C peak-position is unchanged. 42

4.11. He-I ($h\nu = 21.2$ eV) valence band spectra of various thickness' of C_{60} layer on Ag(111). The characteristic HOMO and HOMO-1 peaks simultaneously shift towards smaller kinetic energies. The individual spectra are scaled by an arbitrary factor to stress the shifts. 44

4.12. Rigid band shift of the C_{60} HOMOs with increasing film thickness indicate a charge transfer and screening. 44

4.13. UPS spectra close to E_F of different films. In contrast to the SubPc layer, the C_{60} and the two-component films show filled states at the Fermi edge. 45

4.14. Valence band spectra close to E_F of pure C_{60} , pure SubPc and a two-component film on Ag(111) with approximately the same amount of the components, together with a calculated linear-combination of the pure films. All features of the SIMP spectra simply can be explained by the pure films, thus no strong interactions between the two components are believed to take place. 45

4.15. Isobar T, c -diagrams for the phase behavior of 3D binary systems with limited miscibility in the liquid phase. In the dashed areas, a homogeneous phase of both components exists. a) For instance the Phenol-Water-system: a Water-rich and a Phenol-rich phase can coexist up to an upper critical solubility-temperature T_c . Above the phase boundary line, a homogeneous mixture is found at any composition, at a certain higher temperature, a liquid-gas-transition takes place; b) System with lower critical solubility-temperature, e.g. Triethylamin-Water; c) System with lower and upper critical solubility-temperature, e.g. Nicotine-Water; The assignment of the SIMP system needs further investigations, most notably variable temperature STM experiments. Graphics from [153].	48
4.16. Relation between entropy and energy for $U_{AA}=0.5$ eV [127], $U_{BB}=0.19$ eV [75], $U_{AB}=0.42$ eV. At the relative concentration $c=0$, only A -molecules exist, $c=1$ stands for the pure B phase. The competition between energy and entropy determines the emerging phases.	50
4.17. In a mixed system, the free energy can have two minima, leading to a demixing at distinct concentrations of the components.	51
4.18. Rough Ag(111) surface with C_{60} islands of hexagonal shape. The derivative of the piezo-movement is displayed to simultaneously show the details within the terrace and the huge step bunches. The C_{60} molecules are individually resolved when scanned on a reduced area (not shown here). The fullerenes tend to aggregate and maximize their number of neighbors. This results in a hexagon with the preferred border/inside ratio. Scan range 170 nm x 170 nm. $V_{bias} = 2$ V, $I_t = 15$ pA.	51
4.19. <i>Stripe</i> domain containing a pure C_{60} island. The interior angles of the island always are 120° . This conglomeration of the exceeding fullerenes shows the minimization of the phase boundary lines and the phase boundary energy. Scan Range 50 nm x 30 nm. $V_{bias} = 1.3$ V, $I_t = 20$ pA.	52
4.20. C_{60} on Ag(100): After room-temperature deposition, the molecules are randomly distributed over several terraces. Only when the 1 st layer is full, a 2 nd layer can grow. Scan range 95 nm x 95 nm. $V_{bias} = 2.5$ V, $I_t = 30$ pA.	54
4.21. C_{60} on Ag(100) after annealing to 570 K for 10 minutes. Densely-packed islands are formed. Due to different chemical bonding to the substrate, bright and dark C_{60} molecules appear. The bright molecules form pseudo-periodic structures. Scan range 65 nm x 65 nm. $V_{bias} = 1.8$ V, $I_t = 30$ pA.	55
4.22. C_{60} on Ag(100) after annealing to 570 K for 10 minutes. The bright molecules are distributed in zigzag or square structures along a preferential orientation. Scan range 17 nm x 17 nm. $V_{bias} = 1.8$ V, $I_t = 30$ pA.	55
4.23. Space-filling model of the N, N', N'', N''' -Tetra(trimethylsilyl)-4,9-diamino-perylenchinon-3,10-diimin molecule. Colors specify different elements: white: H, black C, blue N, green Si. For the chemical structure see figure 4.27.	56
4.24. 3D Crystal packing of N, N', N'', N''' -Tetra(trimethylsilyl)-4,9-diamino-perylenchinon-3,10-diimin [164].	56

List of Figures

4.25. Perylen arrangement in 2D on a Ag(100) surface: STM measurement reveal a molecular herringbone structure. Scan range 15 nm x 7 nm. $V_{bias} = 1.8$ V, $I_t = 60$ pA. The derivative of the piezo-movement is shown. 57

4.26. Perylen molecules form a perfect herringbone structure on Ag(100). The island is preferential closed by straight lines. Scan range 33 nm x 33 nm. $V_{bias} = 1.8$ V, $I_t = 20$ pA. 57

4.27. The Perylen molecules arrange in a *herringbone* structure where every molecule is oriented perpendicular to its neighbors. The molecules are lying flat on the substrate for a strong π -orbital-substrate overlap. The electron distribution in the molecules, as is seen in the electrostatic potential surface, favors the orthogonal arrangement. 58

4.28. STM measurement of Perylen herringbone domains with different angular orientation on a stepped Ag(100) surface. The molecules self-assemble without additional annealing. Scan range 71 nm x 71 nm. $V_{bias} = 0.7$ V, $I_t = 20$ pA. The derivative of the piezo-movement is shown. 58

4.29. Photo of a floor panel with herring-bone structure. Image size 1 m x 0.66 m. 59

4.30. This image shows the segregating system Perylen – C₆₀ on Ag(100). The Perylenes form a perfect herringbone structure, while the fullerenes arrange around the Perylen-island. Imaged after annealing to 560 K for 15 minutes. Longer annealing induces pseudo-periodic structures in the C₆₀ islands but no intermixing. Scan range 52 nm x 52 nm, $V_{bias} = 1.8$ V, $I_t = 24$ pA. 59

5.1. Within a stripe, a single C₆₀ molecule reversibly jumps between two metastable positions which could be assigned to bit-states. In this illustration, the fast scan direction is vertical. 60

5.2. Self-healing of the *stripe* pattern: **a)** Perfect *stripe* domain, recorded at $V_{bias} = 1.6$ V, $I_t = 20$ pA, tunneling resistance $R_t = 80$ G Ω , scan range 22 nm x 22 nm, time 0 s. Notice that the SubPc molecules are hardly visible due to the rather low bias voltage V_{bias} of 0.7 V (section 4.2.3). **b)** Same area after a tip-induced distortion at the center of the image (16 mV bias voltage V_{bias} during ≈ 50 ms for a lower tunneling resistance of $R_t = 800$ M Ω). Four stripes are perturbed. Image recorded with the same tunneling and scan parameters as in a). Time 170 s. **c)** Left row is recovered. Three rows still are broken. Time 227 s. **d)** Only two rows remain broken. Time 332 s. 61

5.3. After a tip-crash, the *stripe* pattern restores naturally. 500 sec after the destruction, 40% of the initially replaced molecules are “naturally” reassembled in the original pattern. 62

5.4. The line-scan over the stripe with two missing C₆₀ molecules from figure 3.10 shows the high signal/noise ratio of the potential storage device. 63

A.1. Relaxed geometry (vacuum conformation) of a single free Cu-TBPP molecule. Colors specify different elements: C, dark gray; H, white; N, blue; Cu, red (see figure A.3). The molecule has a diameter of about 2 nm and is about 0.9 nm high.	66
A.2. Series of space-filling models, showing the rotation of the upper right TBP-group around a σ -single bond.	66
A.3. Chemical structure of Cu-tetra-[3,5 <i>di-ter-butyl-phenyl</i>] porphyrin (Cu-TBPP).	68
A.4. At low molecular coverage, the Cu-TBPP molecules decorate the steps of Ag(100). The molecules can be identified as single square-like objects. Scan range 40 nm x 40 nm. $V_{bias} = 1$ V, $I_t = 150$ pA.	69
A.5. Step decoration of Cu-TBPP on Ag(100) at low molecular coverage. Scan range 112 nm x 112 nm. $V_{bias} = 1$ V, $I_t = 150$ pA. A slight median filter and superimposition of the derivative was applied. Artificially colorized.	69
A.6. At higher coverage, the Cu-TBPP molecules form condensed islands on Ag(100). The individual legs appear with different heights. A height-profile on the marked line can be found in figure A.7. Scan range 11 nm x 8.5 nm. $V_{bias} = 1$ V, $I_t = 40$ pA.	70
A.7. Height-profile on the line drawn in figure A.6. Different heights are assigned to different leg-orientations.	70
A.8. Histogram of the STM image in figure A.6: The four fitted gaussian curves represent the Ag substrate, low, medium and high legs, respectively. Most of the legs show the medium conformation and are approximately 35% smaller than the bright legs.	71
A.9. 3D illustration of an STM image with a Cu-TBPP island and atomic resolved Ag(100) substrate. The tunneling parameters were changed close to the upper end during the scan from molecule-sensitive to atom-sensitive. $V_{bias} = 1$ V, $I_t = 40$ pA for molecules (lower part); $V_{bias} = 0.1$ V, $I_t = 150$ pA, 10x faster scan-speed (0.015 s/line) for atoms (upper part). The substrate lattice (with a lattice constant of 0.289 nm) and the Porphyrin superstructure (with an intermolecular-distance of 1.4 nm) are rotated approximately 6° against each other. Scan range 15 nm x 15 nm.	72
A.10. Three successive STM images a), b) and c) of the same Cu-TBPP island on Ag(100), recorded with identical scan and tunneling parameters. The time between the images is 103 s. The two marked molecules change the appearance during the scans: the molecule labeled by a circle changes from <i>south</i> to <i>west</i> conformation, whereas the molecule labeled by a square changes from <i>west</i> to <i>north</i> conformation. All other molecules are unaffected. Scan range 9 nm x 6.5 nm. $V_{bias} = 1$ V, $I_t = 40$ pA.	73
A.11. Cu-TBPP on Ag(100). The scans were completed 103 s after each other. The conformation of the two imaged molecules has repeatedly changed between the scans. This image is rendered by the <i>POV-Ray</i> TM Raytrace program packet [196]. $V_{bias} = 1$ V, $I_t = 40$ pA.	74

List of Figures

A.12. This color image is a composition of two successive STM images (from figure A.10), each with its own color (bright blue and yellow). The differences between the two images appear in the original color, whereas the unchanged areas result in purple. Two special molecules stand out due to an alteration of their conformation. 74

A.13. Three successive STM images of the same condensed Cu-TBPP island on Ag(100). The time between the images is 50 s. Only in some time slices during the scan, the tip had changed to become sensitive enough to distinguish between the intramolecular features of molecules with various conformation. Scan range 90 nm x 90 nm. $V_{bias} = 2.2$ V, $I_t = 20$ pA. 75

Acknowledgements

The work in this thesis could not have been performed without the support of many people who I would like to thank at this point.

First of all, I thank professor H.-J. Güntherodt for making the organic molecule scanning tunneling microscopy project possible by his continuous support.

A special thank belongs to Dr. T.A. Jung as my supervisor for all his effort in understanding the STM-method, during the measurements, the analysis and the publication of data.

I thank professor H.-J. Güntherodt, professor E. Meyer and Dr. T.A. Jung for agreeing to be referee for my thesis.

In addition, I would like to thank all other past and present co-workers of the Nanolab who shared the best and the worst moments with me and whose contributions can be found in all parts of this thesis: Simon Berner, Luca Ramoino, Hitoshi Suzuki, Silvia Schintke, Alex Heuri, Diego Haldemann, Frank Meisinger, Stefan Vock, Thomas Gasche, Hisao Yanagi.

For continuous theoretical support and many hours of highly scientific discussion I thank Alexis Baratoff, Christoph Bruder and Stanley Ivan.

I thank the past and present members of the Güntherodt and Meyer group and the electronic lab for making the last three years a pleasant time. Mr. H.-R. Hidber and Remo Hofer always had an idea solving computer problems and taught me to use the POV-RAY and SXM programs. Specially, I would like to thank Mrs. J. Vetter, Mrs. G. Weaver, Mrs. A. Vischer, Mrs. A. Kalt and Mrs. B. Kammerman for the administrative and uncomplicated support. I thank the mechanical workshops for materializing my ideas. The support from S. Jakob and H. Breitenstein and the work from P. Cattin, P. Wunderli, W. Roth and coworkers is indispensable for our Lab. For the support in organizing the “Anfängerpraktikum für Physik” I thank Prof. Gian-Reto Plattner and Prof. Berndt Krusche.

I thank T. Kamikado, S. Yokoyama and S. Mashiko (Kansai Advanced Research Center, Japan) for providing the porphyrin molecules, H. Kliesch and D. Wöhrle (University of Bremen, Germany) for synthesizing and providing the SubPc molecules and L. Gade (Universite Strassbourg, France) and Chr. Galka (University of Würzburg, Germany) for synthesizing and providing the Perylen molecules.

Financial support by the Swiss National Science Foundation, the TopNano 21-Project, the NCCR Nanoscale Science and the University of Basel is gratefully acknowledged.

I thank my parents for their support and love during the last few decades.

Finally, I thank my wife Judith, who had to endure the long working hours that were needed during this thesis. The time spent with her has always refreshed and inspired me.

Conferences and Publications

Conference presentations related to this work

- Workshop Scanning Probe Microscopies and Organic Materials IX, 9.-11.10.2000, Hannover (Germany):
Structure and Conformation of Single Molecules from UHV-STM
M. Brunner, S. Berner, H. Suzuki, T.A. Jung and H.-J. Güntherodt
- Sci and Ski seminar, 19.-23.3.2001, Andermatt (Switzerland):
Multiphase adsorption of molecules in a two dimensional bottle: Two dimensional molecular motion and dynamic equilibrium.
M. Brunner, S. Berner, L. Ramoino, H. Suzuki, H. Yanagi, D. Schlettwein, T.A. Jung and H.-J. Güntherodt
- STM-7, Molecular Nanosystems: From Single Molecules to Supramolecular Assemblies, 15.-20.7.2001, Vancouver (Canada):
Conformational Flexure and Switching of a Single Porphyrin
M. Brunner, S. Berner, H. Suzuki, Chr. Loppacher, T. Kamikado, T.A. Jung, E. Meyer, R. Bennewitz and H.-J. Güntherodt
- Frühjahrstagung der Deutschen Physikalischen Gesellschaft, 11.-15.3.2002, Regensburg (Germany):
Complex 2D Phase Behavior observed for Binary Mixtures of Porphyrin Derivatives
M. de Wild, S. Berner, H. Suzuki, T.A. Jung, and H.-J. Güntherodt
- Molecular Nanosystems: From Single Molecules to Supramolecular Assemblies, 14.-19.4.2002, Ascona (Switzerland):
Self-Intermixed Monolayer Phases
M. de Wild, S. Berner, H. Suzuki, T.A. Jung, and H.-J. Güntherodt
- Scanning Probe Microscopy, Sensors and Nanostructures IV, 26.-29.5.2002, Las Vegas (USA):
Formation of Nanostructures by a Novel Self-Assembling Technique in a Bi-Molecular System
M. de Wild, S. Berner, H. Suzuki, A. Baratoff, S. Ivan, H.-J. Güntherodt, and T.A. Jung
- Visit of the Center for Integrated Science and Engineering at the Columbia University, 3.-5.6.2002, New York (USA):
Self-Assembly of Organic Molecules at Metal-surfaces observed with a UHV-STM
M. de Wild, S. Berner, A. Baratoff, S. Ivan, H.-J. Güntherodt, and T.A. Jung
- Nano-7 ECOSS-21, 21th European Conference on Surface Science, 23.-28.6.2002, Malmö (Sweden):
Novel Self-Assembling Technique In A Bi-Molecular System
M. de Wild, S. Berner, H. Suzuki, A. Baratoff, S. Ivan, H.-J. Güntherodt, and T.A. Jung
- NCCR-meeting, 3.-6.9.2002, Pontresina (Switzerland):
Molecular Self-Assembly and Flexibility
M. de Wild, S. Berner, H. Suzuki, A. Baratoff, S. Ivan, H.-J. Güntherodt, and T.A. Jung

Publications

1. *Characterisation of molecular overlayers on metal surface in dynamic equilibrium by scanning tunnelling microscope*
H. Suzuki, S. Berner, M. Brunner, H. Yanagi, D. Schlettwein, T.A. Jung, H.-J. Güntherodt
Thin Solid Films **393**, 325-328 (2001)
2. *Time evolution of a 2D solid-gas equilibrium: a model system for molecular adsorption and diffusion*
S. Berner, M. Brunner, L. Ramoino, H. Suzuki, H.-J. Güntherodt, T.A. Jung
Chemical Physics Letters **348**, 175-181 (2001)
3. *Production method for atomic and molecular patterns on surfaces and nanostructured devices*
M. Brunner, S. Berner, H. Suzuki, T.A. Jung
EU Patent Application (2001)
4. *A Novel Route To Molecular Self-Assembly: Self-Intermixed Monolayer Phases*
M. de Wild, S. Berner, H. Suzuki, H. Yanagi, D. Schlettwein, S. Ivan, A. Baratoff, H.-J. Güntherodt, T.A. Jung
ChemPhysChem **10**, 881-885 (2002)
5. *Molecular Assembly and Self-Assembly: Molecular Nanoscience for Future Technologies*
M. de Wild, S. Berner, H. Suzuki, L. Ramoino, A. Baratoff, T.A. Jung
Chimia **10**, 500-505 (2002)

Curriculum Vitae

17. Juni 1972	Geboren in Basel, Sohn von Markus und Theres Brunner-Ilg
1979-1984	Primarschule in Binnigen
1984-1988	Progymnasium in Binnigen
1988-1991	Gymnasium Oberwil mit Maturität Typus C
1992-1997	Physikstudium an der Universität Basel
Juli-Dezember 1995	Semesterarbeit " <i>Photoconductivity and Electrical Fluctuations in Hydrogenated Amorphous Silicon</i> " in der Halbleitergruppe des Departements Kondensierter Materie an der Universität Utrecht (Niederland) unter Prof. J.I. Dijkhuis
April 1996	Geologie Nebenfach-Examen, spezialisiert in Mineralogie und Geophysik
Februar 1997	Diplomexamen in Experimentalphysik
September 1997	Diplomarbeit " <i>Supraleitende Mesoskopische Drähte</i> " in der Forschungsgruppe Mesoskopische Physik an der Universität Basel unter Prof. Chr. Schönenberger
Oktober 1997-Juni 1999	Sensorentwicklung bei Durchflussmesstechnik Coriolis, F&E Abteilung Endress+Hauser, Flowtec AG in Reinach (BL)
Juli 1997-August 1997	Arbeit in der Hollandia SAC Hütte in 3240 mü.M.
September 1999	Beginn der Doktorarbeit unter der Leitung von Dr. T.A. Jung in der Gruppe von Prof. H.-J. Güntherodt am Institut für Physik der Universität Basel
September 1999	Beginn der Assistententätigkeit als verantwortlicher Leiter des "Anfänger Praktikum für Physik" unter Prof. G.-R. Plattner, später Prof. B. Krusche

Folgenden Dozentinnen und Dozenten verdanke ich meine Ausbildung:

C. Bandle (BS), A. Baratoff (BS), R. Bennowitz (BS), C.E. De Capitani (BS), de Wijn (NL), J.I. Dijkhuis (NL), E. Meyer (BS), J.P. Goedbloed (NL), S. Gräser (BS), H.-J. Güntherodt (BS), H.A. Hänni (BS), L. Hauber (BS), G. 't Hooft (NL), I. Sick (BS), J. Jourdan (BS), T.A. Jung (BS), H. Mühri (BS), P. Oelhafen (BS), H. Rudin (BS), B. Scarpellini (BS), S.M. Schmid (BS), Chr. Schönenberger (BS), F.C. Schüller (NL), A. Spaenhauer (BS), W.B. Stern (BS), L. Tauscher (BS), H. Thomas (BS), D. Trautmann (BS), C. Ullrich (BS), A. Wetzler (BS), I. Zschokke-Graenacher (BS).

BS: Universität Basel, Schweiz

NL: Rijks Universiteit Utrecht, Nederland